Spectroscopy of High Energy Ion-Neutral Collisions

Yawei Lin

Thesis submitted to the

Faculty of Graduate and Postdoctoral Studies

In partial fulfillment of the requirements for

the degree of Doctor of Philosophy

In the Ottawa-Carleton Chemistry Institute

Department of Chemistry, University of Ottawa

Ottawa, Ontario, Canada

2011

Candidate	Supervisor
Yawei Lin	Dr. Paul M. Mayer

Abstract

This research work focused on studying the emission spectroscopy produced from the high energy ion-molecule collision processes in mass spectrometry. The collision experiments are described and divided into 4 chapters (Chapter 3, 4, 5, 6).

$N_2O^{+\bullet}$ is an ion of atmospheric importance. In chapter 3 the investigation of the collision between high translational energy (4-8 keV range) $N_2O^{+\bullet}$ ions and Helium target gas in mass spectrometry using collision induced emission (CIE) spectroscopy is described. A commercial analytical mass spectrometer coupled with a spectrograph and charge-coupled device (CCD) detector was used to obtain the collision-induced emission (CIE) spectra (190 – 1020 nm). The observed emissions were from the $A\ ^2\Sigma^+ \rightarrow X\ ^2\Pi^+$ system of $N_2O^{+\bullet}$, excited fragments of the parent molecule and the target gas. The relative emission intensities of the $N_2O^{+\bullet}$ ions and their fragments were independent of the ion translational energy within the 4-8 keV range, confirming the curve-crossing mechanism for translational-to-internal energy transfer in this system. Band emission intensities of 1_0^1 and 3_1^1 relative to the 1_0^0 band within the $N_2O^{+\bullet}$ ($A \rightarrow X$) system have been measured and compared with reference data. The results indicated that the collisionally excited ion has a decidedly non-Franck-Condon vibrational state distribution.

In chapter 4, the collision-induced emission (CIE) spectra from 4-8 keV collisions between projectile $He^{+\bullet}$ ions and CO_2 target gas ($He^{+\bullet}/CO_2$) were obtained. The observed emissions were from the A $^2\Pi_u^+$ and B $^2\Sigma^+_u$ states of $CO_2^{+\bullet}$, excited states of He, and with excited fragments. The relative vibrational population of the A $^2\Pi_u^+$ state were estimated and compared with our previous $CO_2^{+\bullet}$/He studies. The results indicate that charge transfer ionization of CO_2 in $He^{+\bullet}/CO_2$ collisions is similar to that of photon excitation, while in the case of $CO_2^{+\bullet}$/He, the population is more evenly distributed due to intramolecular vibrational redistribution (IVR) after the collision. Adiabatic potential energy surfaces calculated at the CISD/6-311+g(2df) level of theory for $CO_2^{+\bullet}$/He collisions, show the curve crossing of the $CO_2^{+\bullet}$ A $^2\Pi_u^+$ and $CO_2^{+\bullet}$ B $^2\Sigma^+_u$ states, in agreement with our observation.

In high energy (keV) CID experiments, oxygen has the unique ability to enhance specific ion fragmentation pathways that lie within a relatively narrow band of activation energy. It has been previously proposed that this oxygen enhanced dissociation phenomenon was due to the participation of the O_2 B $^3\Sigma_u^+ \rightarrow$ X $^3\Sigma_g^-$ (Shumann-Runge) system in the collision complex. During the collision, oxygen was first being excited to its B $^3\Sigma_u^+$ state then subsequently returns this energy back to the projectile ion. This energy drives the non-statistical dissociation of the projectile ion provided there is an energetically accessible pathway in resonance with the absorbed radiation. In Chapter 5, to probe the validity of this hypothesis, CIE experiments were carried out to observe the photon emissions from keV collisions of a selection of projectile ions with O_2 target gas. By studying the resulting CIE spectra, a second potential mechanism came to light, one that involves the nearly isoenergetic $O_2^{+\cdot}$ A $^2\Pi_u \rightarrow$ X $^2\Pi_g$ state transition.

In chapter 6, neutral hydroxymethylene and formaldehyde were generated by charge exchange neutralization of their respective ionic counterparts and then were reionized and detected as recovery signals in neutralization-reionization mass spectrometry in the modified VG-ZAB mass spectrometer. The reionized species were characterized by their subsequent collision-induced dissociation (CID) mass spectra. The transient diradical hydroxymethylene was observed to isomerize to formaldehyde with an experimental life time exceeding 13.9 μs. The vertical neutralization energy of the $HCOH^+$ ion has also been identified using charge transfer reactions between the fast ions and stationary target gases of differing ionization energy. The measured values match the result of *ab initio* calculations at the QCISD/6-311+G(d,p) and CCSD(T)/6-311++G(3df,2p) levels of theory. Neutral hydroxymethylene can also be produced by proton transfer from CH_2OH^+ to a strong base such as pyridine, confirmed by appropriate isotopic labelling. There is a kinetic isotope effect for H^+ vs D^+ transfer from the C atom of the hydroxymethyl cation of ~ 3, consistent with a primary KIE of a nearly thermoneutral reaction.

Acknowledgements

I am deeply grateful to my supervisor, Dr. Paul Mayer, for providing me for his guidance, encouragement, and for the confidence he has always shown in me. My PhD study would not have been possible without his supports. I express my sincere gratitude to him for helping me through the 4-year oversea studying, introducing me to mass spectrometry and providing me an enthusiastic and productive environment which enabled me to bring my study to a successful completion.

Special thanks go out to Dr. John Holmes for his helpful comments and discussions of my work, Dr. Sander Mommers for making all the filaments and for always being there when the ZAB was not working. I have worked with a number of colleagues who have been incredibly supportive and encouraging. I would like to take this opportunity to thank all of them for making the lab an enjoyable place to work: Sharon Curtis, Clement Kazakoff, Eric Martineau, Justin Renaud, Brandi West (in alphabetic order) and all other past colleagues.

Last but not least, I would like to thank my husband Liu Xin and all my family members for being supportive and understanding throughout the course of my studies. I would also like to thank the University of Ottawa and my supervisor Paul Mayer for financially supporting.

Table of Contents

Abstract		ii
Acknowledgements		v
Table of Contents		vi
List of Figures		xi
List of Tables		xv
Abbreviations		xvi

Chapter 1: Introduction

1.0	Goal of this thesis	1
1.1	Ion-molecule collisions in space	2
1.2	Ion-molecule collisions in mass spectrometry	3
1.2.1	Frame of reference	5
1.2.2	Interaction potential	8
1.2.3	Impact parameter, *b*	9
1.2.4	Classification of collision processes	9
1.2.5	Mechanisms of collisional excitation	10
a)	Electronic excitation	11
b)	Ro-vibrational excitation without electronic excitation	15
c)	Formation of a long-lived collision complex	16
d)	Predissociation of the projectile ion induced by the target	16
1.2.6	Methods for studying high energy ion-molecule collisions	17

a) Translational energy spectroscopy 17

b) Angle-Resolved Mass Spectrometry 23

c) Collision-induced emission spectroscopy 25

1.2.8 Summary of the works in this thesis 27

Chapter 2: Methods of Study

2.1 The Modified VG-ZAB Mass Spectrometer 29

2.11 Ion source 30

2.12 Magnetic analyzer 32

2.13 Electrostatic analyzer 33

2.14 Ion detector 35

2.2 Experiments performed in the VG-ZAB Mass Spectrometer 36

2.2.1 Collision-Induced Dissociation experiment 37

2.2.2 Neutralization-reionization mass spectrometry experiment 37

2.2.3 Collision-induced emission experiment 38

REFERENCES 41

Chapter 3: Fluorescence from the A $^2\Sigma^+$state suggests a non--Franck-Condon $N_2O^{+\bullet}$ vibrational state population after keV collisional activation with helium.

3.1 Introduction 46

3.2 Experimental procedures 49

3.3 Results and disscusion 51

3.3.1 Emission spectrum from $N_2O^{+\bullet}$/He collisions 51

3.3.2 Relative emission intensity as a function of ion translational energy 52

3.3.3 Relative band strength in the A $^2\Sigma^+$ state $N_2O^{+\bullet}$ 53

3.4 Conclusion 56

REFERENCES 57

Chapter 4: A comparison of the charge transfer and collisional activation processes in ionized CO_2/He collisions

4.1 Introduction 68

4.2.1 Experimental procedures 70

4.2.2 Potential energy curves calculation of collision complex $CO_2^{+\bullet}$-He 72

4.3 Results and discussion 73

4.3.1 Emission spectrum from $He^{+\bullet}/CO_2$ collisions 73

4.3.2 Vibrational distribution in the A state $CO_2^{+\bullet}$ ion 75

4.4 Conclusion 77

REFERENCES 78

Chapter 5: Do the O_2 Shumann -Runge bands participate in keV collision-induced dissociation experiments?

5.1 Introduction 91

5.2 Experimental procedures 94

5.3 Results and discussion 95

5.3.1 CIE spectra of $CH_3NO_2^{+\bullet}/O_2$ and $CH_3NO_2^{+\bullet}$/He collisions 96

5.3.2 CIE spectra of $N_2^{+\bullet}/O_2$ and $N_2^{+\bullet}$/He collisions 97

5.3.3 CIE spectra of CH_3^+/O_2 collisions 98

5.4 Conclusion 99

REFERENCES 100

Chapter 6: Can neutral hydroxymethylene play a significant role in interstellar space? A neutralization-reionization and reactivity mass spectrometry study

6.1 Introduction 111

6.2 Experimental procedures 114

6.2.1 Chemicals 114

6.2.2 Neutralization-reionization mass spectrometry 114

6.2.3 FT-ICR mass spectrometry 115

6.3 Theoretical procedure 116

6.3.1 Geometry optimization and frequency calculation 116

6.3.2 Gaussian-3 calculation 117

6.4 Results and discussion 118

6.4.1 CID experiments for $HCOH^{+\cdot}$ (1a) and $H_2CO^{+\cdot}$ (2a) 118

6.4.2 Neutralization-reionization (NR) for *trans*-^{1}HCOH (1b) and H_2CO (2b) 119

6.4.3 NR-CID experiments to identify *trans*-^{1}HCOH (1b) 120

6.4.4 Vertical neutralization energy (NEv) experiment 120

6.4.5 Proton transfer reactions 121

6.5 Conclusions 124

REFERENCES 125

Chapter 7: Conclusions 139

Claims to original research 141

List of publication 143

List of Figures

Figure 1.1	(a) Initial and (b) final trajectories of a fast ion- neutral target collision between M^+ and X, viewed in the laboratory frame of reference.	6
Figure 1.2	Trajectory of the same collision in Figure 1.1, viewed in the center-of-mass frame of reference.	6
Figure 1.3	The Newton velocity diagram for the same collision as described in Figure 1.2.	6
Figure 1.4	A t plot of an interaction potential *V(r)* for an Atomic ion-atomic targe system (M^+-X) as a function of ion-target separation, *r*.	8
Figure 1.5	Definition of the impact parameter *b*.	9
Figure 1.6	Diagram illustrating a electronic transition (with vibrational feature).	11
Figure 1.7	Simplified diagram illustrating curve crossing during ion-target collisions.	13
Figure 1.8	TES spectrum of $C^{+\cdot}$ colliding with N_2, at 3 keV collision energy. (refer to Ref. 44 in Page 43)	18
Figure 1.9	TES spectra of 3-keV H^+ and $H_2^{+\cdot}$ projectile ions scattered off N_2. (refer to Ref. 45 in Page 43)	19
Figure 1.10	Energy change spectra for 4-keV C^{2+}/Ar collisions obtained with a C^{2+} beam containing (a) a mixture of ground and metastable content, (b) only ground state and (c) only ^3P metastable ions. (refer to Ref. 46 in Page 43)	21
Figure 1.11	High-resolution TES scan of the N^+ fragments from the CID of 10-keV $N_2^{+\cdot}$/He collisions spectrometers. (refer to Ref. 49 in Page 44)	22
Figure 2.1	Schematic diagram of the modified VG-ZAB mass spectrometer used in this research work.	29
Figure 2.2	A typical electron ionization (EI) ion source used	31

in mass spectrometers.

Figure 2.3 A magnetic analyzer used in mass spectrometers to select ions with specific m/z ratio. 32

Figure 2.4 A electrostatic analyzer used in mass spectrometers to select ions with specific translational energy . 34

Figure 2.5 Schematic diagram of the ion detector used in the mass spectrometer. 35

Figure 2.6 A simplified layout (not to scale) of the modified VG-ZAB with BEE geometry showing collision cells and deflector electrodes. FFR, CC and ESA represent field-free region, collision cell and electrostatic analyzer for short 36

Figure 2.7 The inside of the third field-free region. spectrometer. 39

Figure 3.1 A simplified diagram illustrating curve-crossings during ion-target collisions. 63

Figure 3.2 Collision-induced emission spectra of $N_2O^{+\bullet}$/He collisions at 8 keV. 63

Figure 3.3 Collision-induced emission spectra of $N_2O^{+\bullet}$/He collisions at 8, 6 and 4 keV. 64

Figure 3.4 Ab initio potential curves for a collinear $N_2O^{+\bullet}$ geometry calculated by Komiha et al. (refer to Ref. 32 in Page 58). Reprinted with permission) 65

Figure 3.5 The plot of the lifetime-corrected relative emission intensities of $N_2O^{+\bullet}$, N^+, N, and O at various ion translational energies vs. those at 8 keV. 66

Figure 3.6 Collision-induced emission spectrum of 8 keV $N_2O^{+\bullet}$/He collisions obtained with an entrance slit width of 1.0 mm 67

Figure 4.1 Collision trajectory of $CO_2^{+\bullet}$/He collisions and adiabatic potential energy curves of the $CO_2^{+\bullet}$-He collision complex calculated at the CISD/6-311+g(2df) level of theory. 86

Figure 4.2 Collision-induced emission spectra of 87

$He^{+\bullet}/CO_2$ collisions at 8 keV.

Figure 4.3 Adiabatic potential energy curves of the $CO_2^{+\bullet}$/He collision complex at various β values calculated at the CISD/6-311+g(2df) level of theory. 88

Figure 4.4 Collision-induced emission spectrum of 8 keV $He^{+\bullet}/CO_2$ collisions obtained with an entrance slit width of 1.0 mm 89

Figure 4.5 Peaks in the $CO_2^{+\bullet}$ $A\ ^2\Pi_u^+ \rightarrow X\ ^2\Pi_g$ emission obtained from $He^{+\bullet}/CO_2$ collisions fitted by Franck-Condon factors. Individual vibrational transitions from (i,0,0) of the $A\ ^2\Pi_u^+$ state to (j,0,0) of the $X\ ^2\Pi_g$ state are represented as i-j. 90

Figure 5.1 Partial He and O_2 CID mass spectra of (a) source $^+CH_2OH$ (b) source $^+CH_2NH_2$ (c) $CH_3NO_2^{+\cdot}$ 104

Figure 5.2 Potential energy diagram of O_2 and $O_2^{+\cdot}$ by Krupenie (refer to Ref.16 in Page 101) 105

Figure 5.3 a) CIE spectra of $CH_3NO_2^{+\cdot}/O_2$ versus $CH_3NO_2^{+\cdot}$/He, slit width 3mm;accumulation time 1hr.b) CIE spectra of $CH_3NO_2^{+\cdot}/O_2$; 40% beam reduction; slit width 3mm; accumulation time 2hrs 106

Figure 5.4 CIE spectrum of $N_2^{+\cdot}/O_2$ versus $N_2^{+\cdot}$/He, 40% beam reduction; slit width 3 mm,accumulation time 2hrs. 107

Figure 5.5 a) CIE spectrum of $N_2^{+\cdot}/O_2$, slit width 1mm, b) CIE spectrum of $N_2^{+\cdot}/O_2$,slit width 0.5mm. Superimposed on the spectrum are the $A\ ^2\Pi_u \rightarrow X\ ^2\Pi_g$ $O_2^{+\cdot}$ emission bands 108

Figure 5.6 a) CIE spectrum of $N_2^{+\cdot}/O_2$ versus CH_3^+/O_2, slit width 1 mm. b) CH_3^+/O_2, 40% beam reduction; slit width 0.5 mm. Superimposed on the spectrum are he $A\ ^2\Pi_u \rightarrow X\ ^2\Pi_g$ $O_2^{+\cdot}$ emission band 109

Figure 5.7 CIE spectrum of CH_3^+/O_2, slit width 0.5 mm. Superimposed on the spectrum are the Shumann-Runge ($B\ ^3\Sigma_u^+$ — $X\ ^3\Sigma_g^-$) O_2 emission bands reported in the literature 110

Figure 6.1 A simplified layout (not to scale) of the modified VG-ZAB with BEE geometry showing collision cells and deflector electrodes. 134

Figure 6.2 Schematic relative G3 energies for CCSD(T)/6-311++G(3df,2p) and QCISD/6-311+g(d,p) level of theory. 134

Figure 6.3 Collision induced dissociation mass spectra of $[C,H_2,O]^+$ produced from respectively (a) formaldehyde, (b) methanol 135

Figure 6.4 Neutralization-reionization mass spectra of $[C,H_2,O]^+$ produced from respectively (a) formaldehyde, (b) methanol. 136

Figure 6.5 Neutralization-reionization-collision induced dissociation mass spectra of $[C,H_2,O]^+$ produced from respectively (a) formaldehyde, (b) methanol. 137

Figure 6.6 Neutralization-reionization-collision induced dissociation mass spectra of [C,H2,O]$^+$ produced from methanol with neutralization gas as respectively (a) 1-butene, (b) 2-butene, (c) dimethylamine. 138

List of Tables

Table 3.1	Observed emissions in Figure 3.2 and their corresponding radiative lifetimes	60
Table 3.2	Band emission intensities of 1_0^1 and 3_1^1 relative to 1_0^0 band of $N_2O^{+\bullet}$ ($A \rightarrow X$) system	61
Table 4.1	Observed emissions in the collison of $He^{+\bullet}$ with neutral CO_2.	82
Table 4.2	The relative peak intensity ratios for the molecular emission of $CO_2^{+\bullet}$	83
Table 4.3	The relative vibrational populations for states (0,0,0) to (7,0,0) in the $CO_2^{+\bullet}$ A $^2\Pi_u^+$ state.	84
Table 6.1	Properties of neutralization gases and data from the corresponding NR-CID mass spectra	129
Table 6.2	Peak intensity ratio of m/z 13 to m/z 14 from CID and NR-CID mass spectra[a] of $[C,H_2,O]^+$ ions	130
Table 6.3	Optimized Bond Lengths (Å) and Bond Angles (°) for **1a**, **2a**, **1b** and **2b**	131
Table 6.4	Relative abundances (%) of the BH^+ and BD^+ product ions formed in the reaction of a base B with D-labeled hydroxymethyl cation and protonated methanol.	132

Abbreviations

CCD	Charge-Coupled Device
CID	Collision-Induced Dissociation
CIE	Collision-Induced Emission
CISD	Configuration Interaction with Single and Double Excitations
Da	Dalton (= Atomic Mass Unit)
DFT	Density Functional Theory
ECD	Electron Capture Dissociation
ECR	Electron Capture Resonance
ETD	Electron Transfer Dissociation
EI	Electron Ionization
ESA	Electrostatic Analyzer
FFR	Field-Free Region
G3	Gaussian-3 Theory
IE	Ionization Energy
IS	Interstellar
IVR	Intramolecular Vibrational Energy Redistribution
m/z	Mass-to-Charge Ratio
MP2	Second-Order Møller-Plesset Perturbation Theory
MP4	Fourth-Order Møller-Plesset Perturbation Theory
MS	Mass Spectrometry
MS/MS	Tandem Mass Spectrometry

NR	Neutralization-Reionization
NRMS	Neutralization-Reionization Mass Spectrometry
PES	Potential Energy Surface **OR** Photoelectron Spectroscopy
QCISD	Quadratic Configuration Interaction with Single and Double Excitations
RRKM	Rice-Ramsperger-Kassel-Marcus Theory
SID	Surface Induced Dissociation
TES	Translational Energy Spectroscopy
TS	Transition State

Chapter 1 Introduction

1.0 Goal of this thesis

` Collisional activation method is widely used in mass spectrometry, however the energy transfer mechanisms behind those ion-target collisions is still not fully understood. In this study of work, the goal is to obtain emission spectroscopy from the collision processes between high energy (in keV range) ions and neutral target gases in mass spectrometry. With the rich collision induced spectroscopic information from the fragments and precursor ions, the energy distribution and activation mechanism of the high energy ion-molecule collisions can be investigated.

1.1 Ion-molecule collisions in the space

Our knowledge of outer space has been greatly expanded over the past decades by the spectroscopic measurements of interstellar (IS) compounds obtained by a wide variety of space born and ground based instruments. This spectroscopic information ranges through emission and/or absorption lines of electronic, rotational, and vibrational transitions and over 100 molecular species have been identified in the interstellar medium. It has been accepted that ion-molecule collisions play a key role in the formation of interstellar molecules [1]. Such reactions were first discussed in detail in 1970 by Klemperer et al. [2]. Also, ion-molecule collisions are one of the causes of an atmospheric phenomenon - aurora [3]. Auroras on earth result from optical emissions from high-latitude “polar regions” due to the collisions between the solar wind and atmospheric atoms and molecules. Aurora emissions from other planets such as Jupiter, Saturn, Venus and Mars etc have also been observed, providing remote-sensing information about the collisional processes at aurora latitudes and the planetary magnetospheric regions where they originate [4,5].

To study these ion interactions experimentally, mass spectrometry (MS), of course, became the method of choice because its ability to direct ions and the near-vacuum condition that the instrument operate under [6,7].

1.2 Ion-molecule collisions in mass spectrometry

Mass spectrometry (MS) has become one of the most versatile analytical techniques with numerous chemical and biological applications. MS instruments consist of three modules, ion source (which can convert sample molecules into gas-phase ions); mass analyzer (which sorts the ions by their mass to charge (m/z) ratios), detector (which provides data for calculating the ion abundance).

Early mass spectrometers were capable of only one stage of mass analysis, so that structure elucidation of the ions was limited. With the advent of tandem mass spectrometry (MS/MS), ion activation methods are applied to facilitate the fragmentation of ions to obtain more detailed structural information. Several ion activation techniques have been developed, such as collision induced dissociation (CID) [8], surface induced dissociation (SID) [9], electron capture dissociation (ECD) [10] and electron transfer dissociation (ETD) [11] etc, among which CID remains the most widely used ion activation method used in present day instruments.

Collision induced dissociation (CID) is the first activation method used for MS/MS studies. Its history can be traced to work published in 1913, when J. J. Thomson [12] observed a residual signal from $H_2^{+\cdot}$, though it was not until 1919 that Aston explained the signal as a result of collisional activation [13]. In 1968 the laboratories of McLafferty and Jennings described how the leakage of gas into a field-free region (FFR) gave rise to additional fragmentation of the ion beams traversed them and reported their CID mass spectra [14]. At that time, the leakage was taken as a source of “interference” to the

observation of metastable peaks. In 1973, a key paper by Mclafferty [15] showed the potential of how this "interference" can be put to use to effect an exponential increase in the amount of MS information obtained from MS/MS methods. Much of the ensuing work was devoted to developing CID as a tool for distinguishing isomeric ion structures (for further information, refer to the book by Holmes et al [16]). Until the advent of the triple quadrupole instrument for analytical MS/MS as described by Yost and Enke in the late 1970s [17], all CID experiments were carried out on magnetic sector mass spectrometers (collision energies in the keV range). Particularly noteworthy contributions to our understanding of CID at low collision energies (1-100eV) were made by Beauchamp [18] and McLuckey [19] et al. in 1990s.

In mass spectrometry, CID is often considered a two-step process: collisional activation and dissociation after activation, shown in equation 1.1 and 1.2, respectively:

$$M^+ + X \rightarrow (M^+)^* + X \qquad (1.1)$$

$$(M^+)^* \rightarrow \text{dissociation product ions and neutrals} \qquad (1.2)$$

In step 1, the ions are usually accelerated by some electrical potential and then allowed to collide with neutral target gas (often helium, nitrogen or argon). During the collision, some of the kinetic energy of the projectile ion is converted into its internal energy. In the second step, the excited ion can undergo bond breaking, producing dissociation product ions and neutrals.

When the precursor ion (i.e. M^+) is polyatomic, step 2 of the CID process is a unimolecular dissociation which can usually be explained by Rice, Ramsperger Kassel and Marcus (RRKM) theory [20,21] (though exceptions still exist which will be discussed in chapter 5). Assumptions of RRKM theory are that all oscillator motions within an ion are independent and all microscopic states have equal statistical probabilities. Therefore, the internal energy can be assumed to be distributed among all internal degrees of freedom and the production of the mass spectrum is the result of the competition between the energetically accessible dissociation pathways no matter how the internal energy got into the ion in the first step.

Step 2 (eq. 1.1) deals with how collision energy is converted into internal energy, which is the major concern of this study. A brief review of this process is given in the next section.

1.2.1 Frame of reference

To simplify the description of the ion-molecule collision process, it is better to work in the center-of-mass (com) frame of reference rather than laboratory framework [8,21]. In the latter, the target gas is considered to be stationary and the collision energy is simply taken as the kinetic energy of the ion. Figure 1.1 shows the trajectory in the laboratory frame of reference.

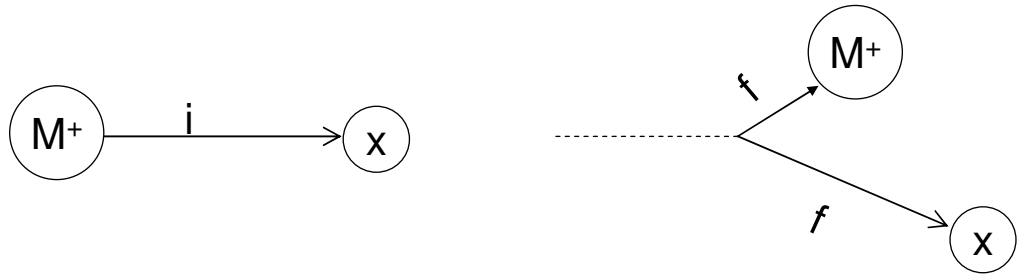

(a) (b)

Figure 1.1 (a) Initial (i) and (b) final (f) trajectories of a fast ion- neutral target collision between M^+ and X, viewed in the laboratory frame of reference.

However, not all of this laboratory kinetic energy is available for conversion into internal energy because of the conservation of momentum. A conversion to the com framework makes the situation easier to describe since the centre of mass momentum is always zero, shown in Figure 1.2.

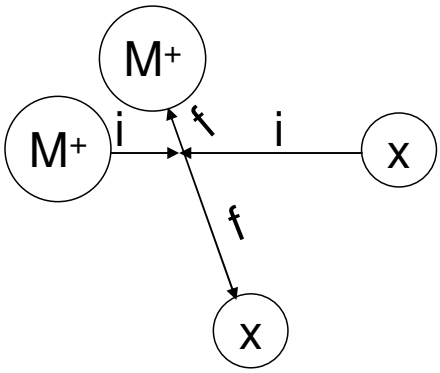

Figure 1.2 Trajectory of the same collision in Figure 1 viewed in the center-of-mass frame of reference

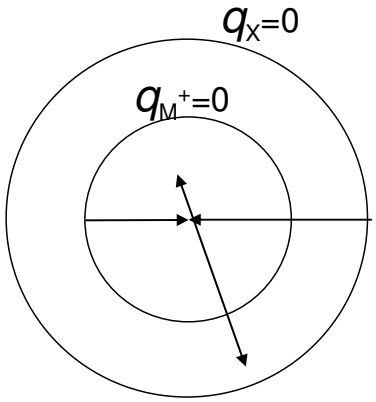

Figure 1.3 The Newton velocity diagram for the collision in Figure 2.

In the center of mass (com) frame work, the collision centre is chosen as the point in space at which the mechanical moments of the two collision partners are equal and opposite.

It is equivalent to "sitting" on the centre of mass of the collision system and watching the collision partners approach each other from opposite directions and recede from each other after collision. Thus, the available collision energy is the kinetic energy in the framework of centre-of-mass (KE_{com}) rather than that in the laboratory frame (KE_{lab}) [23]. The KE_{lab} and KE_{com} are related by equation 1.3

$$KE_{com} = KE_{lab}\left(\frac{m_X}{m_X + m_{M^+}}\right) \qquad (1.3)$$

where m_X and m_{M^+} is the mass of the neutral target molecule and the projectile ion M^+, respectively.

As indicated from the above expression, both the laboratory kinetic energy and the masses of the collisional partners can influence the collision energy interconversion. The collision processes occurring in mass spectrometry can be classified as high or low energy collisions based primarily on the kinetic energy in the laboratory frame of reference: high energy collisions with KE_{com} in keV range ($KE_{com} >$ 100 eV) are common in sector and TOF/TOF instruments. Low energy collisions, seen in quadrupole and ion trap mass spectrometers, have a collision energy range of to 1~ 300 eV (KE_{com}<100 eV). Intermediate collisions often refer to those that are in between and do not occur in commonly used tandem mass spectrometers.

1.2.2 Interaction potential

The simplest theory describing the collision is the so-called hard-sphere collision theory [23]. In the case of a collision between an atomic projectile ion and atomic target, the interaction potential is similar to that of a diatomic molecule, shown in Figure 1.4.

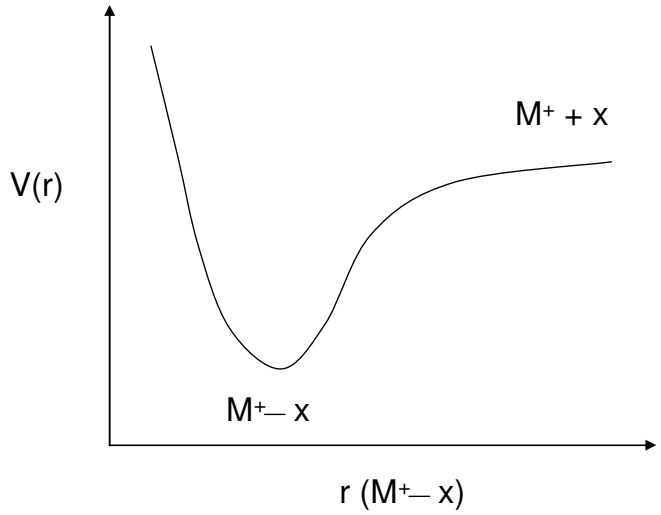

Figure 1.4 A plot of the interaction potential *V(r)*, for an atomic ion-atomic target system (M^+-X) as a function of ion-target separation, *r*.

There are two distinct parts of the interaction potential: an attractive potential at large interatomic distances and a repulsive potential at small distances. For a polyatomic projectile and target this picture will extend to three or multi-dimensions. The mathematical form of the attractive potential will depend on the diffuseness of the charge on the projectile ion and on the nature of the interaction; for example, r^{-2} for ion-dipole, r^{-3} for ion-quadupole and r^{-4} for ion-induced dipole, where r is the distance between the projectile and the target. For targets such as helium, the attractive part of the potential can often be ignored due to its small radius. However, for polyatomic and polarizable targets, it must be considered. A strong attractive potential can increase the relative velocities of the two species so that the

collisional energy may beyond the simple KE_{lab} measurements. The repulsive part of the interaction potential can be the source of collisional scattering and change as a function of $e^{(-r)}$, where r is the distance between the projectile and target.

1.2.3 Impact parameter, *b*

Another term defines the ion-target collision is the impact parameter, *b*. Shirts et al. used *b* to describe pictorially the collision process, shown in Fig 1.5. It is given by $r\sin\theta$, representing the distance of closest approach of two collision partners. Large values of *b* represent "soft" collisions while "hard" collisions have small values and $b = 0$ is for head on collisions.

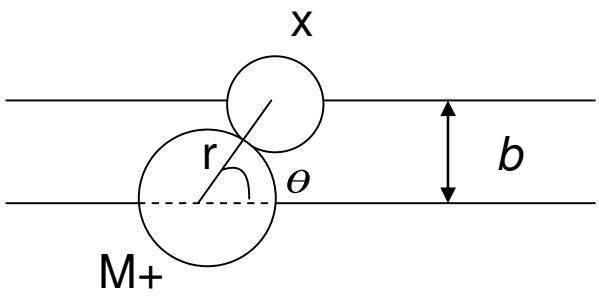

Figure 1.5 Definition of the impact parameter *b*

1.2.4 Classification of collision processes

Based on the *net* exchange between internal energy and kinetic energy of the collision system, q (designated as the collision endothermicity), the collision process can be divided into elastic collisions ($q = 0$), inelastic collisions ($q > 0$) and superelastic collisions ($q < 0$). A classical picture of an elastic collision is the billiard ball collision. In elastic collisions, the recoil velocities and angles of the collision partners must obey conservation of energy and momentum. The elastic scattering can be represented by the Newton velocity diagram [8,23], shown in Figure 1.3. In the diagram, elastic collision vectors fall on the two circles and those fall inside and outside the circles indicate inelastic and superelastic collisions, respectively.

For the atomic ion-atomic target collisions that do not result in electronic change, they can be considered elastic, while for collisions involving at least one di- or polyatomic species, they are seldom elastic, since the chemical bonds are never infinitly rigid.

1.2.5 Mechanisms of collisional excitation

A number of mechanisms have been proposed for the ion-molecule collisions in mass spectrometers. Durup [25] summarized that there are several possible processes that would take place after ion-molecule collisions, such as a) electronic excitation without scattering, b) vibrational and rotational excitation of the ion, c) formation of a long-lived collision complex and d) predissociation of the projectile ion induced by the target. In this section, these mechanisms will be introduced, with special emphasis placed on the electronic excitation following collision, which is relevant to my study.

a) Electronic excitation

The possible mechanisms for electronic excitation are vertical excitation and a curve-crossing mechanism. Vertical excitation is often used to explain photon excitation. According to the Franck-Condon principle [26], because the nuclei are much more massive than the electrons, an electronic transition takes place faster than the nuclei can respond, so that the initial state and the excited state have similar geometries during the transition, shown in Fig 1.6.

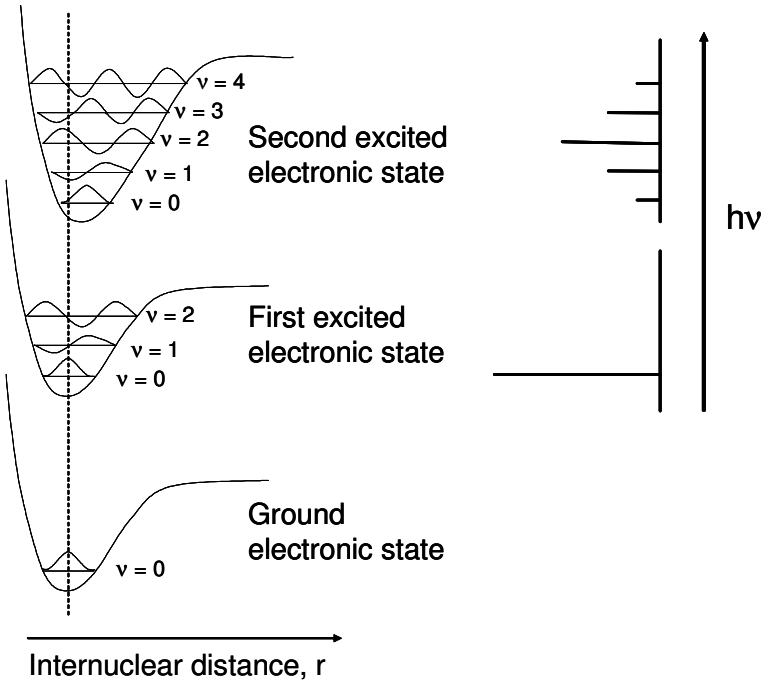

Figure 1.6 Energy diagram illustrating the electronic transition (with vibrational feature).

The quantum mechanical formulation of this principle is that the relative probability of transition, known as the Franck-Condon factor (*FC*) is proportional to the square of the overlap integral between the vibrational wavefunctions of the two states that are involved in the transition, shown in equation 1.4.

$$FC = \left\langle \int \psi_{\nu}^{'} \psi_{\nu}^{''} dR \right\rangle^{2} \qquad (1.4)$$

where $\psi_{\nu}^{'}$ and $\psi_{\nu}^{''}$ represent the wave function of an upper and a lower state, respectively.

The vertical excitation is expected to be important at short time scales (10^{-14} s or less). In most MS/MS experiments interaction times tend to be longer than that, especially for those polyatomic ions with masses larger than a few hundred amu. For very light precursor ions (e.g. < 50 amu) in the keV range, the vertical transition mechanism may still be important [8].

The other mechanism for electronic excitation is the curve-crossing mechanism, which is also the most widely applicable one for electronic transitions in the collisional activation of polyatomic ions [8,27,28]. The qualitative and quantitative description of curve crossing adiabatic energy transfer to produce electronic excitation has been described by Massey, Burhop, Gilbody [29] and Nikitin [30]. Figure 1.7 shows a simplified diagram describing the curve crossing mechanism, in which only two adiabatic potential energy curves are shown, one for the ground state and one for the excited state. During the collision process, when the projectile ion M^+ approaches the target X, the energy of the collision complex increases along the adiabatic curve of the ground state (in the case of using He as the target gas), until the ground state potential surface crosses with that of an excited state

through point C and the collision complex will continue along the excited state potential energy curve, bringing about a radiationless transition between the ground and electronic excited state of the collision complex.

The strength of the non-adiabatic coupling of the two curves can be represented as the Massey parameter, ξ, described by the Massey equation [31,32]

$$\xi = a\Delta E / h\upsilon \qquad (1.5)$$

where ΔE is the smallest energy gap between two adiabatic states, a is the width of the nonadiabatic interaction region and υ is the classical nuclear velocity. When $\xi >> 1$, the probability that a non-adiabatic transition takes place will be small.

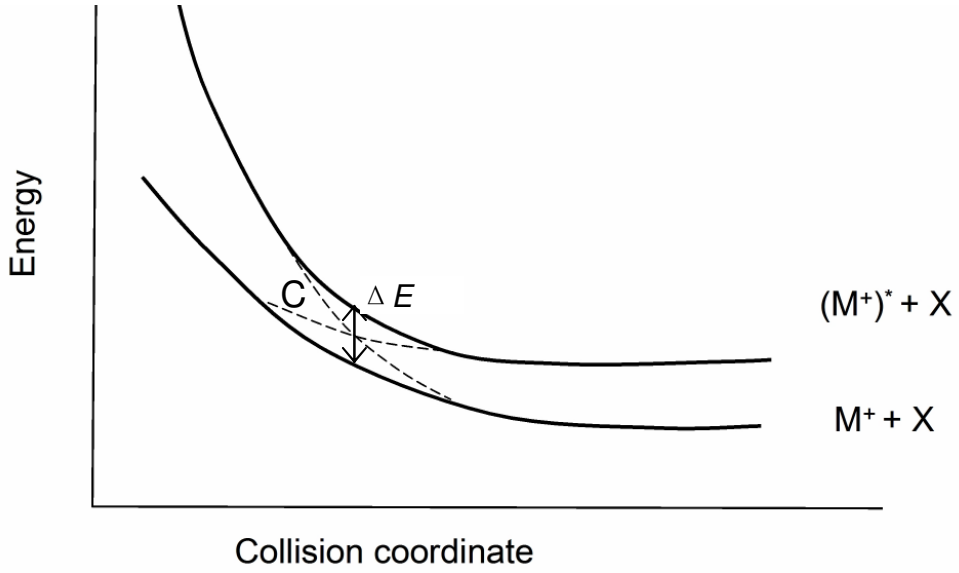

Figure 1.7 Simplified diagram illustrating curve-crossing of the potential energy surface of the collision complex during ion-target collisions.

If the collision complex remains in an excited electronic state, then upon separation of the collision complex, it will produce either the excited ion M^{+*} or the target molecule X^{*}. When using helium as the target, the resulting product will be the excited projectile ion M^{+*} because the high-lying excited states of helium, so that the ions are electronically excited by the collisional activation.

Landau, Zener and Stueckelberg [33-35] described the probability, *P*, of crossing-over of two diabatic potential curves as

$$P = e^{-2\delta} \tag{1.6}$$

where $\delta = \dfrac{(2\pi)^{3/2} H_{12}^2(R)}{((dV_1/dr) - (dV_2/dr))h\nu}$ (1.7)

V is the potential, ν is the relative velocity of the two colliding species and $H_{12}(R)$ is the off diagonal component of the Hamiltonian describing the transition between diabatic states 1 and 2 at distance R. If the transition is optically allowed, $H_{12}(R)$ follows a $\mu^{-2}r^{-3}$ dependence, where μ is the dipole moment of the optical transition.

When there is only a crossing point between two states as described in Figure 1.6, the total probability for the system to end up in the excited state is 2*P*(1-*P*), because it is sampled twice during a collision, once on the way in and once on the way out. From this expression, we can expect the probability to be at the maximum at a set of conditions.

The kinetic energy regime that produces a maximum curve-crossing probability tends to be in the high energy (1-100 keV) range for polyatomic ions. Compared with diatomic ion,

polyatomic ions are more likely to be electronically excited through curve-crossing because for polyatomic ions there are more accessible excited electronic states, which increase the number of crossing points so the probability of the system crossing back to the ground stats on the way out of the collision is small. As polyatomic species get larger, the electronic excitation is likely to be converted into ro-vibrational excitation of ground state by IVR (intramolecular vibrational redistribution).

b) Ro-vibrational excitation without electronic excitation

The curve-crossing mechanism described above can also be applied to the collision activation, which leads to ro-vibrational excitation without first electronically excitation of the projectile ion. The probability of vibrational excitation is small if $\frac{r\nu}{v} >> 1$, where r is the radius of the collidiong ion, ν is the vibrational frequency for the mode being explored and v is the relative velocity of the colliding pair [29,30].

Another possible mechanism that will lead to vibrational and rotational excitation without accompanying electronic excitation is called impulsive collision. It is based on momentum transfer collision between the target and part of the ion. Upon collision, the repulsive part of the potential is sampled and part of the energy can be distributed into vibrational motions [36,37]. We can consider its extreme case in which an ion consisting of two non-interacting parts, a “participant” group P and a “spectator” group S, has negligible force constant between them. Upon collision with the target, momentum transfer occurs to

only group P, leading to the scattering of P but not S. In this case, there is a net internal momentum change in PS^+ and therefore, a part of the incident kinetic energy is transformed into vibrational excitation energy of PS^+.

c) Formation of a long-lived collision complex

The ion-molecule collision can also produce a "long-lived" collision complex if the attractive potential between the ion M^+ and target X is large and if the relative velocity of the two species is small enough. This type of collision is referred to as a "sticky collision", which is quite different from the repulsive collisions in that all the relative translational energy of the colliding pair is converted into internal energy of the complex. The internal energy of the complex is thus KE_{com}. When the long-lived complex dissociate into M^+ and X, part of the complex's internal energy is converted back into the translational energy of the products [25, 38, 39].

d) Predissociation of the projectile ion induced by the target

Predissociation of the projectile ion can occur in a collision while the collision does not formally involve the conversion of translational to internal energy, there is a transfer from a ground electronic state of the ion to a dissociative state brought on by a perturbation to the electronic surfaces by the target. Durup et al. discussed this type of process [25].

1.2.6 Methods for studying high energy ion-molecule collisions

Most of the early collision studies were carried out with high collisional energy (projectile ion with a translational energy in the keV range), such as magnetic sector mass spectrometers which were in wide spread use in early stages of mass spectrometry. Recently, with the advent of TOF/TOF instrument, the high energy collision has become a fragmentation method in renaissance [40-43]. In this thesis, we focused on the high energy collisions in mass spectrometry and several methods for studying high energy ion-molecule collisions are discussed in this section.

.

a) Translational energy spectroscopy

As the collision system is isolated, the translational energy of the projectile ion is the only source of the necessary energy to drive the reactions upon collision. Therefore a direct connection is established between the translational energy loss (or gain) and the internal energy states of the system. A method called translational energy spectroscopy (TES) is thus developed to study the ion-molecule collisions by measuring the change of translational energy in the projectile (Type I TES)bor fragment ions after collisions (Type II TES).

The type I TES experiments commonly studies the collisions between an atomic ion and a neutral molecule because with this combination there is no dissociation of projectile

ion, which allows the studies on the excitation of neutral molecules. An experiment of type I TES, for example, was carried out by Brenton et al. [44], in which collisions of 3 keV $C^{+\cdot}$ on N_2 gas has been studied. The instrument consists of an ion source, a magnet for mass selection, a pair of symmetrical electrostatic analyzers (ESA) for translational energy analysis and a third smaller ESA to eliminate artifact signals.

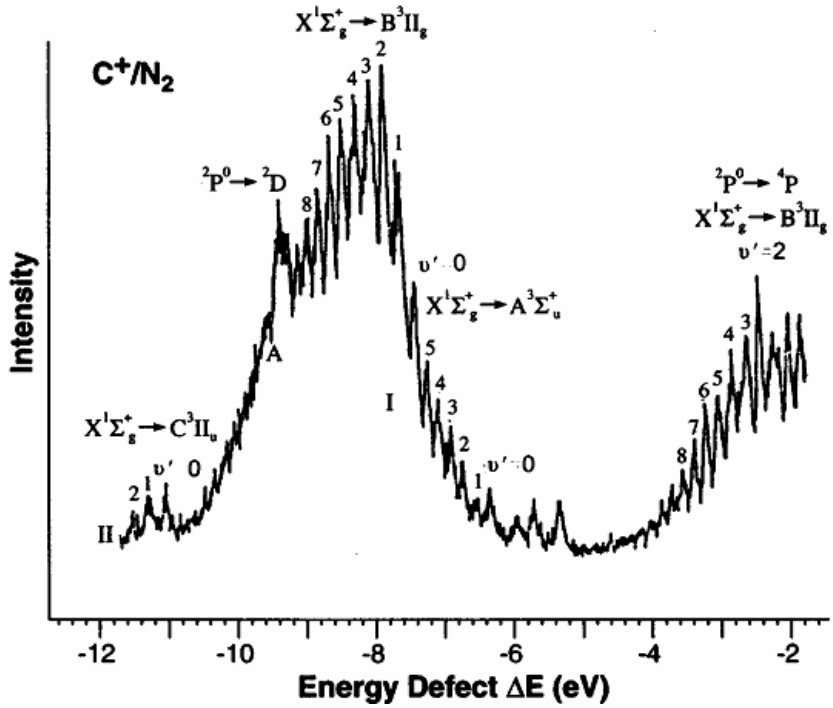

Figure 1.8 TES spectrum of C^+ colliding with N_2, at 3 keV collision energy (refer to Ref. 44 in Page 43).

The obtained TES spectrum is shown in Figure 1.8 where the translational energy loses of $C^{+\cdot}$ were plotted against the ion beam intensities after collision. From the spectrum, several excited electronic transitions of N_2 produced from collision have been revealed, such as $A^3\sum_u^+$, $B^3\Pi_g$ and $C^3\Pi_u$, states, together with their associated vibrational progressions. The

transitions between $^2P^0$ state of $C^{+\cdot}$ to its lower states are also observed, indicating the simultaneous atomic and molecular excitations are the major processes during the collision.

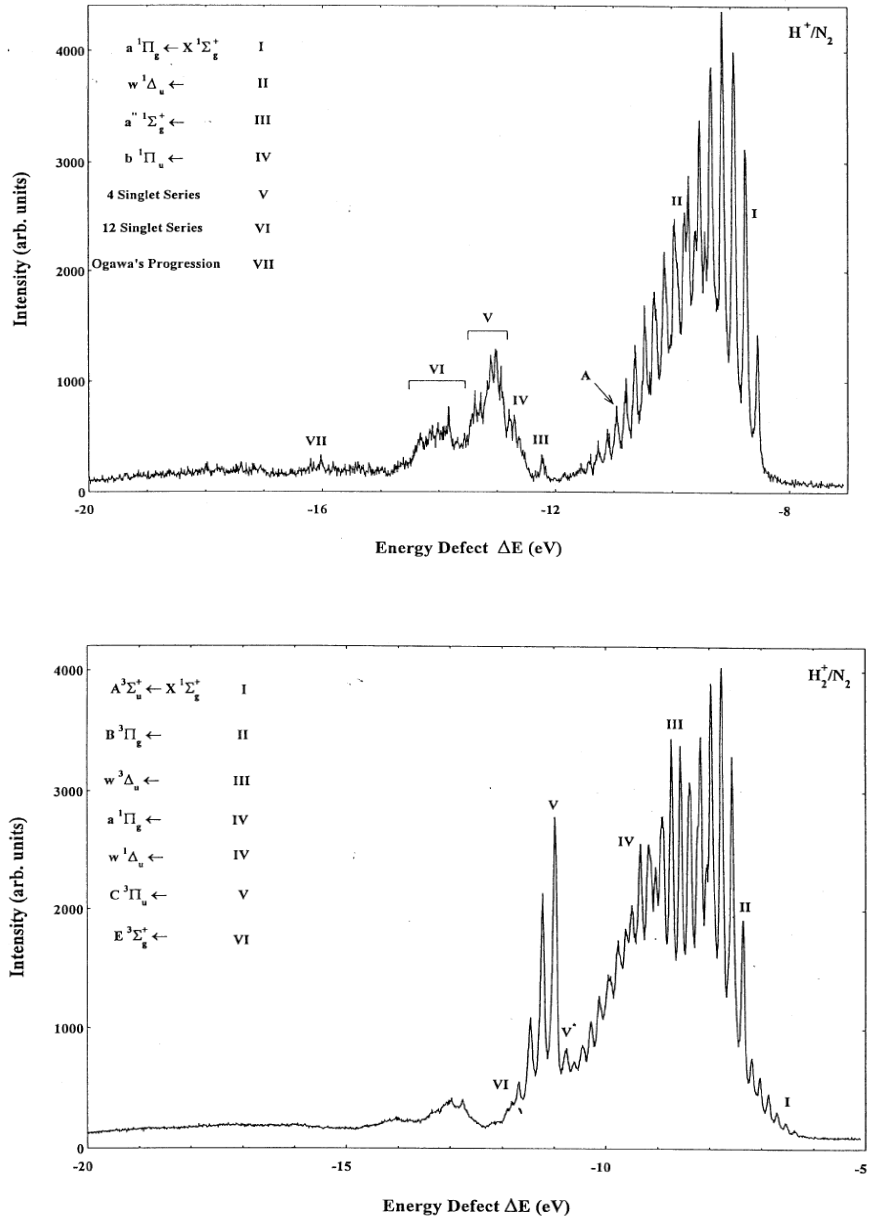

Figure 1.9 TES spectra of 3-keV H^+ and $H_2^{+\cdot}$ projectile ions scattered off N_2 (refer to Ref. 45 in Page 43).

With the same instrument, collisions between H^+ and $H_2^{+\cdot}$ projectile ions and target gas N_2 have been probed [45]. The TES spectra obtained from the two collisions are shown in Figure 1.9 as a comparison.

For H^+/N_2 collisions, only transitions to singlet excited states were observed while both singlet and triplet excited states were observed for $H_2^{+\cdot}/N_2$ collisions. Therefore, spin conservation was obeyed for H^+/N_2 collisions. However, the prominent transitions for H^+/N_2 are $X\ ^1\Sigma_g^+ \rightarrow a\ ^1\Pi_g$ and $X\ ^1\Sigma_g^+ \rightarrow w\ ^1\Delta_u$, both of which break the dipole electronic selection rules that are applied to optical spectroscopy. Excitation from the $X\ ^1\Sigma_g^+$ to a $^1\Pi_g$ state should be symmetry forbidden since g-g and u-u transitions are disallowed. Similarly, for excitation to $w\ ^1\Delta_u$, the orbital angular momentum changes by 2, which also breaks the selection rule $\Delta\Lambda=0, \pm1$. Similar results were obtained from several other collision systems. As a result, it was concluded that not all selection rules that are normally applied to optical spectroscopy are obeyed in collisional excitation.

The translational energy can also be used to select the internal energy of the ions. Recently, there is some interest in studies of state selective electron capture in atomic ion-molecule collisions using translational energy spectroscopy. Gilbody [46, 47] group used double translational energy spectroscopy (DTES) [48] to resolve the ground state and the metastable state of the ion beam. An ion beam of C^{2+}, for example, is known to contain $(2s^2)^1S$ ground state and $(2p)^3P$ metastable C^{2+} ions. In the DTES approach, an intense beam of C^{3+-} ions was first obtained from an Electron Capature Resonance (ECR) ion source, mass selected by a magnet and then collided with He target gas producing $(1s^22s^2)^1S$ ground and

some excited states of C^{2+} through electron capture reaction. The C^{2+} ions were then resolved in TES spectra by their translational energy change. As a result, ^1S ground or ^3P metastable ions can be selected by an electric field and then passed on to another electrostatic analyzer to study their electron capture process by a second stage of TES. Figure 1.10 illustrates a comparison between energy change spectra for one-electron capture in 4 keV C^{2+}/Ar collisions obtained with a C^{2+} beam containing (a) a mixture of ground and metastable content, (b) only ground state and (c) only ^3P metastable ions. Collision product channels resulting from the respective ^1S ground and ^3P metastable states can clearly be distinguished this way.

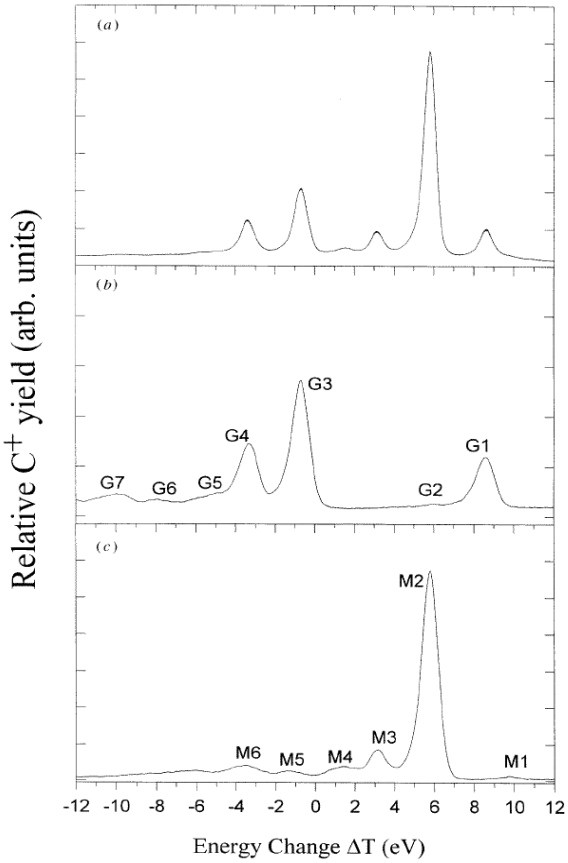

Figure 1.10 TES spectra for 4-keV C^{2+}/Ar collisions obtained with a C^{2+} beam containing (a) a mixture of ground and metastable content, (b) only ground state and (c) only ^3P metastable ions (reproduced with permission) (refer to Ref. 46 in Page 43)

An example of type II TES studies can be demonstrated by the studies of $N_2^{+\cdot}$/He

collisions by Fournier et al. [49]. The obtained TES spectrum, Figure 1.11, shows the laboratory momentum distribution of forward- and backward-scattered N^+ plotted against *W* (the kinetic energy of the dissociation products in the centre of mass framework). Peak h corresponds to $N^{+\cdot}$, which is broad and nearly symmetric. The broadening of the peak is because of the excess energy of the excited $N_2^{+\cdot}$ relative to its dissociation limit, which is represented as e_d. The shoulder peaks labeled from a to f correspond to $N^{+\cdot}$ fragments with different e_d and these peaks agree with e_d of the excited electronic state C $^2\Sigma_u^+$ of $N_2^{+\cdot}$ (vibrational levels ν'=4-9) with respect to the first dissociation limit obtained from spectroscopic data. This indicates that the $N^{+\cdot}$ fragments come from the predissociation of ν' = 4-9 of the $C^2\Sigma_u^+$ state.

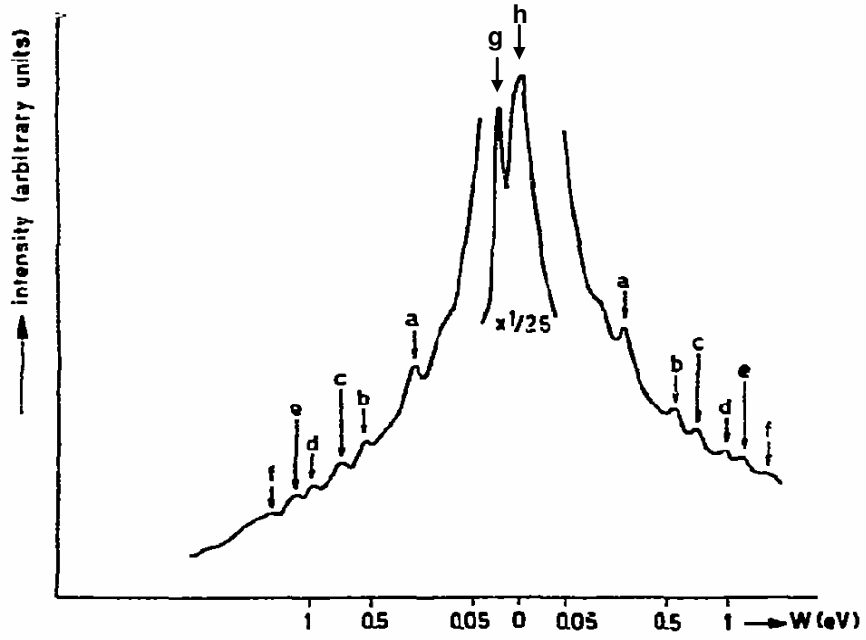

Figure 1.11 High-resolution TES spectrum of the $N^{+\cdot}$ fragments from the CID of 10 keV $N_2^{+\cdot}$/He collisions(refer to Ref. 49 in Page 44).

b) Angle-Resolved Mass Spectrometry

Angle-resolved mass spectrometry is a variation method of translational energy spectroscopy in that translational energy changes are measured at different scattering angles. It is based on the assumption that hard collisions deposit more energy than soft collisions so that the collision impact parameter is related to the internal energy deposited by the collision.

This hypothesis has been tested by the Cooks group [50]. They installed an angle-resolving slit to their double focusing mass spectrometer to obtain energy-loss spectra and CID mass spectra at different scattering angles (typically between 0 and 2 degrees). For $Ar^{+\cdot}$/Ar collisions, four peaks (belonging to one electronic state) were observed in the TES spectrum: one elastic and three inelastic scattering peaks. When small scattering angles are sampled, the elastic scattering peak is much more intense than the inelastic peaks. As the scattering angle increases, the absolute intensity decreases for all peaks but the relative intensity of the inelastic peaks increases. CID mass spectra different scattering angles for ethyl isobutyl ether were also obtained and they followed the same trend. Angle-resolved CID spectra for several molecular ions have been studied by the same group, from which they gave a qualitative proof that selecting scattering angle does select internal energy of the projectile ion.

The target effects have been studied by comparing the results for methanol molecular ions on He, N_2 and Freon using angle-resolved mass spectrometry [50]. The scattering angle giving rise to equal intensities of the two fragment ions were determined for each target. These laboratory scattering angles were 0.44, 0.49 and 0.59 respectively. Helium, with the smallest scattering angle, is the most effective target for the collisional activation. But considering their large difference in mass, their laboratory scattering angles are considerably similar.

The Cooks group has studied the variation of scattering angles due to different translational energies of the projectile ions [52]. An attempt was made to investigate whether the reduced scattering angle, defined as $\tau = E\theta$, can be used to relate scattering angles at different ion translational energies. Energy loss spectra of the same $E\theta$ are similar for $Ar^{+\cdot}$/Ar collision. As $E\theta$ increases, so does the abundance of high-energy loss peaks. Similar behaviour was observed for the CID of nitromethane molecular ions.

Attempts also have been made to correlate the scattering with kinetic energy release (KER) [53, 54]. It is generally agreed that both impact parameters and KER contribute to scattering of the precursor ions. However, separating KER and collision scattering is infeasible. As a result, it would be difficult for angle-resolved mass spectrometry to yield direct information on the internal excitation of projectile ions.

c) Collision-induced emission spectroscopy

Compared with Laser-induced fluorescence spectroscopy, in which emission spectroscopy of polyatomic ions was obtained by laser pulses, a method called collision-induced emission spectroscopy (CIE) can also obtain the emission spectroscopy by high energy ion-molecule collisions. By studying the collision-induced emission spectra, information on the electronic states that are accessible by collisions can be obtained bringing insights to the collision process.

CIE spectroscopy is often carried out in a mass spectrometer for the study of ion-neutral collisions where projectile ions collide with a neutral target gas in a collision cell. The photon emissions are subsequently detected by a photomultiplier tube or a charge-coupled device detector.

Early experiments were carried out to acquire laboratory data on ion-molecule collisions that occur in the Earth's atmosphere, most of which are charge transfer processes between fast ions and small molecules such as N_2, O_2 and CO_2. In addition to the measurement of cross sections for these charge transfer processes, emphasis is also placed on the determination of vibrational state distributions in the excited electronic states. To understand the nature of the collision processes, the observed vibrational state distributions are often compared to those estimated from theory using Franck-Condon factors. Moore and Doering [55] studied the collisions between various projectile ions and target N_2. The vibrational distribution of the $N_2^{+\cdot}$ B state resulting from charge transfer reaction was

estimated by observing the relative band intensities of the $\Delta v = -1$ sequence of the B→X emission. It was found out that the observed vibrational distributions depend heavily on the laboratory velocity of the reactant ion but very little on its chemical nature. When the velocity is below 10^8 cm/s (i.e. ~ 5 keV for H^+ precursor ion), the vibrational distributions no longer agree with the vertical transition model. This disagreement was explained due to distortion of the target molecule electron cloud by the impinging ion at low velocities [55, 56]. However, the similar behavior was also observed in $N_2^{+\cdot}$/target collisions, in which the charge resides on the precursor ion [57]. Therefore, the ion-induced distortion explanation cannot be applied. Instead, Kelly et al. [58, 59] explained it with a more general qualitative curve-crossing model. It is assumed that the deviations from vertical transitions during collisions are caused by short-range, repulsive interaction between the projectile and the target and these short-range interactions result in direct translational-vibrational excitation in both the initial and final electronic states of the diatomic molecule. The fact that short-range forces are involved means that the reaction occurs at small impact parameters. As such, the diatomic molecule cannot be regarded as being isolated. In other words, distortion occurs by chemical forces that are operative in any short-range encounter between the two collision particles.

Ehbrecht et al. also studied the charge transfer process involving multiply-charged ions by CIE spectroscopy [60]. In the experiment, CO^{2+} ions with translational energies ranging from 60-2000 eV were produced to collide with various neutral targets, such as Ar, N_2, H_2, D_2 and CO. The charge transfer process results in $CO^{+\cdot}$ ($B\ ^2\Sigma^+$), and the B → X emission was detected. At 2 keV, the vibrational distributions in $CO^{+\cdot}$ were found to be

similar to those predicted by the Franck-Condon principle while at lower energy, an increase in the population of higher vibrational states was observed, especially from collisions with Ar. In the case of CO^{2+}/N_2 and CO^{2+}/CO collisions where emissions from the ionized targets were also observed, a comparison was made with the analogous product emission from charge transfer with singly-charged projectiles (i.e. $Ar^{+\cdot}/N_2$ and $Ar^{+\cdot}/CO$ collisions). Pronounced deviations from the Franck-Condon prediction in the latter case was explained as the difference in the crossing radius between the entrance and the exit channel potentials. Whenever the crossing radius is large, the vibrational distribution in the product deviates only little from the Franck-Condon prediction and vice versa.

A major advantage with collision-induced emission spectroscopy over translational energy spectroscopy is that it offers a more direct way to identify the energy levels of the collision species. The emission spectra obtained have higher resolution and sensitivity.

In this thesis, the majority of my work is focused on the study of high energy ion-molecule collisions using CIE spectroscopy. A summary of my work is given below.

1.2.8 Summary of the works in this thesis

The projects introduced in this work starts with the CIE studies from an ion of atmospheric importance, $N_2O^{+\cdot}$. The collision mechanism of $N_2O^{+\cdot}/He$ has been discussed (in Chapter 3). The $He^{+\cdot}/CO_2$ study is discussed in Chapter 4, in comparison with a previous

study of $CO_2^{+\cdot}$/He by Poon et al. [61], showing different collision processes. To explain the target effects of O_2, CIE studies were carried out on the collisions between various projectile ions and O_2 (Chapter 5). Lastly, in Chapter 6, a highly reactive compound *trans*-hydroxymethylene was produced by the collision experiments and its energetics have been studied.

Chapter 2 Methods of study

2.1 The modified VG-ZAB Mass Spectrometer

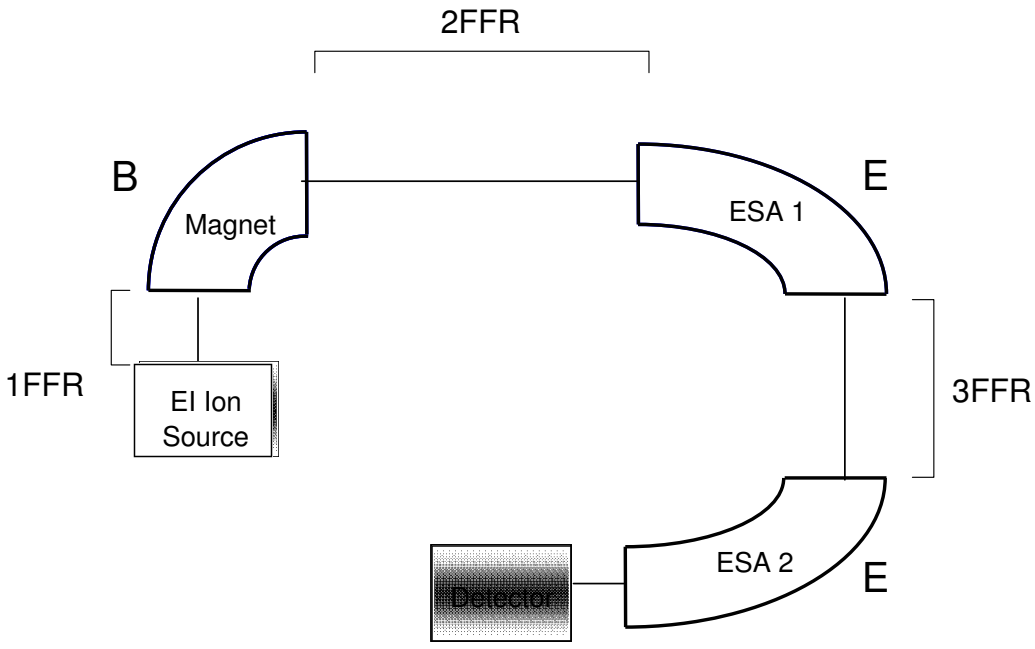

Figure 2.1 Schematic diagram of the modified VG-ZAB mass spectrometer used in this research work.

Tandem mass spectrometry experiments were performed on a modified VG-ZAB mass spectrometer [62] incorporating a magnetic sector followed by two electrostatic sectors (BEE geometry), shown in Figure 2.1. It is composed of one electron impact (EI) ion source, a magnetic mass analyzer and two electrostatic analyzers (ESA). The region between the ion source and the magnetic analyzer is the first field-free region (1FFR). The second field-free region (2FFR) is between the magnetic analyzer and the first electrostatic analyzer. The third field-free region (3FFR) is between the first electrostatic analyzer and the second electrostatic analyzer, in which three collision cells are installed. Collision experiments in this thesis were all carried out in this instrument including collision-induced dissociation CID and neutralization-reionization experiment NRMS etc. A brief introduction of the basic counterparts in the mass spectrometer is given in the next section.

2.1.1 Ion source

In this study an electron impact (EI) ion source [63] is used, the schematic diagram is shown in Figure 2.2.

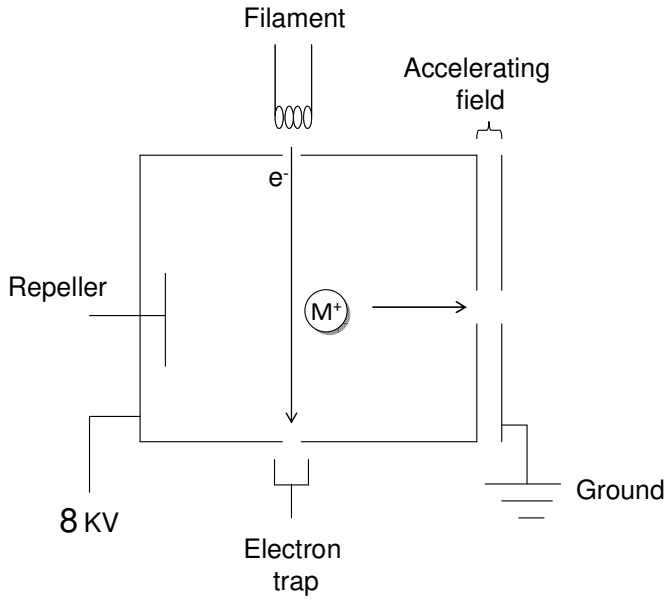

Figure 2.2 A typical electron ionization (EI) ion source used in mass spectrometers.

The major components of the EI source are the filament, electron trap and ion repeller. Electrons are formed by thermal emission from a heated filament and accelerated to approximately 80 eV from a potential difference applied between the filament and the ion source block. The filament current can be adjusted to provide a constant trap anode current and, thus, maintain steady ionizing conditions. When the sample molecules are introduced to the source chamber, this electron beam will interact with them and produce molecular ions. The ions formed are repelled by the ion repeller and pass into the accelerating field of the mass spectrometer. The kinetic energy of the ion is thus determined by the potential difference, V_{acc}, applied between the ion source and the entrance slit of the 1FFR, typically 8kV.

There are 4 sample introduction devices for the ion source: two variable leak valves (one for gas samples and one for liquid vapor), a heated liquid septum for volatile liquids and

a solid probe for solid samples.

2.1.2 Magnetic analyzer

The main job of the magnetic mass analyzer is to apply an external magnetic field to the ions exiting the ion source. It consists of two parallel electromagnets surrounding an iron core, shown in Figure 2.3.

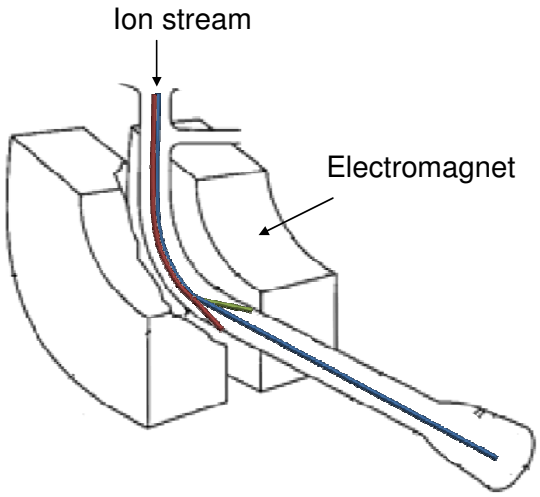

Figure 2.3 A magnetic analyzer used in mass spectrometers to select ions with specific m/z ratio.

Under the influence of the external magnetic field, the ion trajectory will bend. How much an ion's path curves depends on the momentum of the ion and its charge. This is given by the mathematical expression (eq. 2.1) [63]

$$mv = rBze \qquad (2.1)$$

where r is the curvature radius the ion will travel, v is the ion velocity, z is the ion charge and e is the unit of elementary charge.

The kinetic energy of the ion departing the ion source can be expressed using the relationship

$$zeV_{acc} = \frac{mv^2}{2} \qquad (2.2)$$

By combining these two equations, we get

$$\frac{m}{z} = \frac{B^2 r^2 e}{2V_{acc}} \qquad (2.3)$$

In this way, the mass to charge ratio (m/z) is correlated to the magnetic field intensity B, since r is fixed and V_{acc} is held constant. By applying the right magnetic field, ions with specific m/z ratio are allowed to pass through the mass analyzer while others hit the flight tube of the spectrometer vacuum chamber and are neutralized.

2.1.3 Electrostatic analyzer

The electrostatic analyzers in the VG-ZAB mass spectrometer consists of two curved parallel plates at different potentials, shown in Figure 2.4. When entering the electrostatic analyzer, the inward-pointing force generated by this electric field will cause the projectile ions' trajectories to curve in a circular motion with radius r.

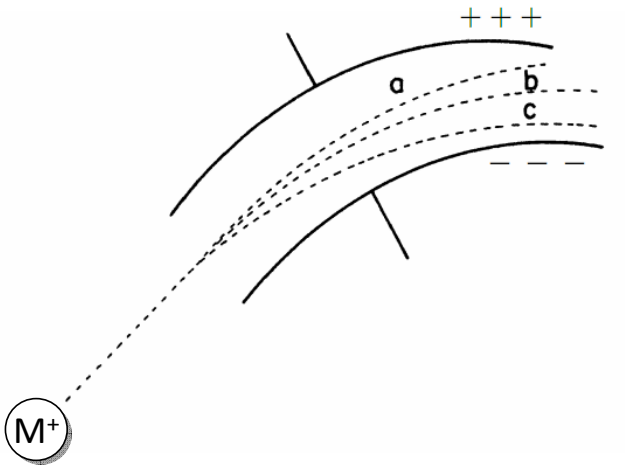

Figure 2.4 An electrostatic analyzer used in mass spectrometers to select ions with specific translational energy

Depending on their initial energy, only certain ions with "correct" translational energy can exit the analyzer while others will collide into the walls of the instrument, as described by the following expression [64]

$$V = \frac{rE}{2} \qquad (2.4)$$

where V is the translational energy of the ion, E is the electric field intensity and r is the radius of curvature.

Therefore, when the projectile ion M^+ falls apart into M_1^+ and M_2 in the 2FFR or 3 FFR without any conversion of internal energy to translational energy (eq. 2.5), the fragments will continue to move along the ion beam at the same velocity. Thus, the ratio of the translational energy follows eq. 2.6.

$$M^+ \rightarrow M_1^+ + M_2 \qquad (2.5)$$

$$\frac{V_{M_1^+}}{V_{M^+}} = \frac{m_{M_1^+}}{m_{M^+}} \qquad (2.6)$$

In this way, by measuring the translational energy of the fragment ions, their mass can be identified.

2.1.4 Ion detector

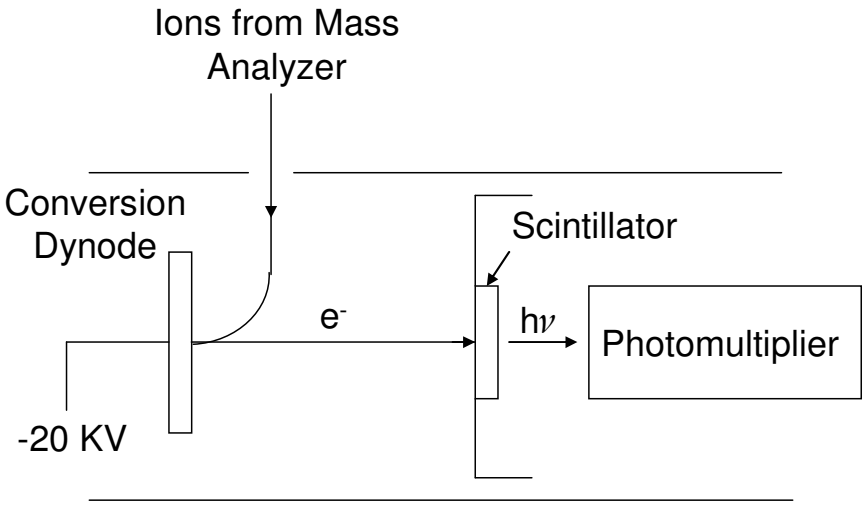

Figure 2.5 Schematic diagram of the ion detector used in the mass spectrometer.

The ion detector in VG-ZAB mass spectrometer is a gas phase ion detector that consists of a conversion dynode, a CaF_2 scintillator (phosphor screen) and a photomultiplier. Ions that hit the conversion dynode release secondary electrons. A high voltage (ca. -20,000 V) between the dynode and the scintillator accelerates the electrons onto the optically coupled photomultiplier and the signal is amplified. All spectra were recorded with the ZAB-CAT program written by Mommers Technologies [65].

2.2 Experiments performed in the VG-ZAB Mass Spectrometer

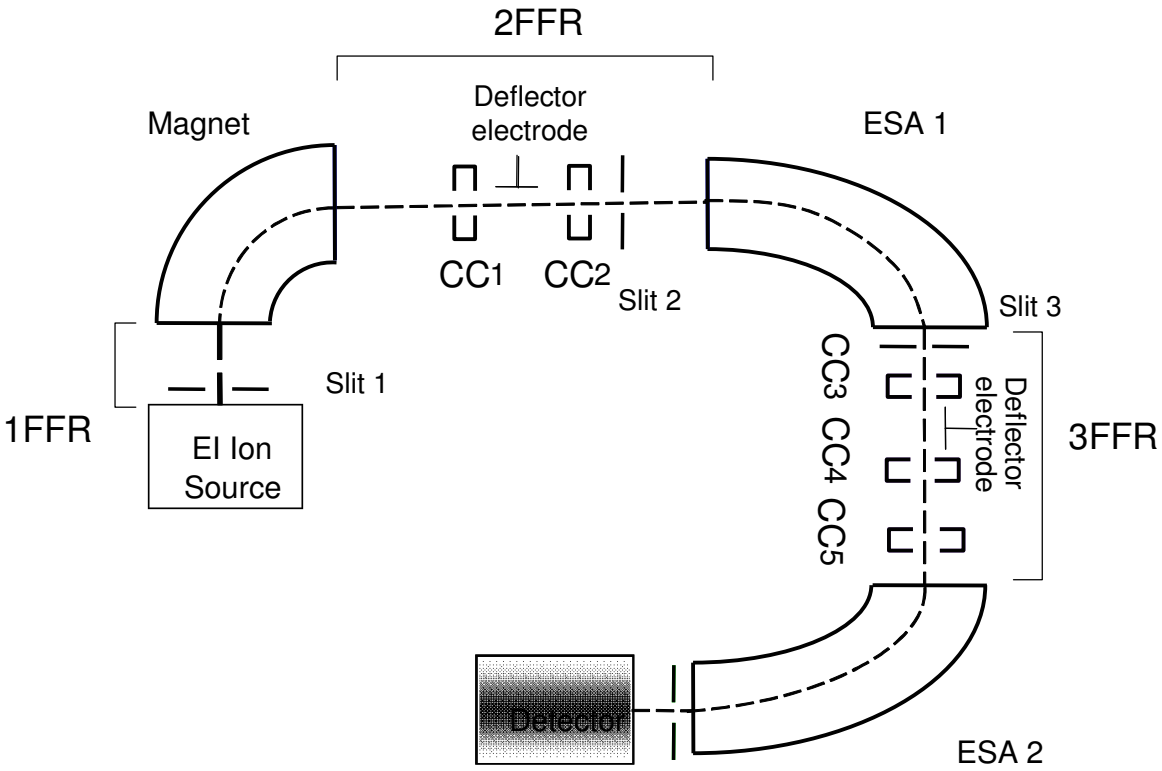

Figure 2.6 A simplified layout (not to scale) of the modified VG-ZAB with BEE geometry showing collision cells and deflector electrodes. FFR, CC and ESA represent field-free region, collision cell and electrostatic analyzer for short.

The collision experiments and spectroscopic experiments are carried out in the second and third field-free region (2FFR and 3FFR) in the VG-ZAB mass spectrometer, shown in Figure 2.6. In each field-free region there are collision cells and an ion deflector. The collision cells are 2-3cm long steel bocks with a 2mm wide groove cut through it to

allow the ion beam to pass through. The collision cells are connected to gas lines so that collision gas can be introduced. The gas pressure in the collision cells is monitored by ionization gauges placed in close proximity. Voltages can be applied to the ion deflector (e.g. 500 V) to remove ions out of the beam path.

2.2.1 Collision-induced dissociation (CID) experiments

Collision-induced dissociation (CID) experiments in the VG-ZAB mass spectrometer were carried out by introducing a target gas into the collision cell. When the ion beam (typically with a kinetic energy of 8 keV) is introduced in the collision cell, it can undergo dissociation. By scanning the ESA to measure the product ion translational energy, the CID mass spectrum is obtained.

In my CID experiments, the target gas was introduced to the collision cell until the ion flux was reduced by 10% (i.e. single collision conditions) [66]. Helium is often chosen as the target gas because it can exist in the pure state and is fast to pump away.

2.2.2 Neutralization-Reionization Mass spectrometry experiment

NRMS [67-70] is associated with the study of neutral molecules rather than ions. Generally speaking, after ions are transmitted to the first collision cell (CC1) in the second field-free region (2FFR), shown in Figure 2.6, some of the ions undergo electron transfer reaction and become neutralized (under single collision condition), other remaining ions are all deflected by a charged deflector electrode (with a voltage of +500 V). Thus, only neutral species are allowed to enter the next collision cell (CC2). In CC2, neutral molecules are reionized and dissociated by the target gas (single collision). The NRMS spectrum is then produced.

To identify the reionized ions, they were transmitted to the third field-free region (3FFR) where they undergo collision-induced dissociation. Therefore, a NR-CID spectrum can be obtained. Detailed descriptions are given in Chapter 6.

2.2.3 Collision induced emission (CIE) experiment

The goal of collision induced emission experiments is to study the emission spectroscopy produced by high energy collision between the projectile ion and relatively stationary neutral target gas. It is carried out in the third field-free region (3FFR) in VG-ZAB mass spectrometer, shown in Figure 2.7.

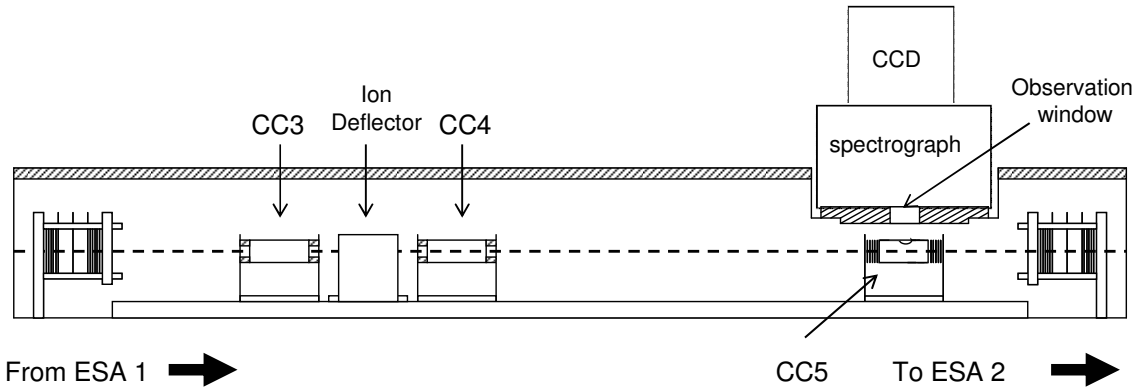

Figure 2.7 The inside of the third field-free region. CC and ESA and CCD represent collision cell, electrostatic analyzer and charge-coupled device for short.

The 3FFR, between the first and the second electrostatic analyzer, is a 1m long box that is differentially pumped by two six-inch diffusion pumps. Two optically correct rails run along the bottom of the box, allowing collision cells and other experimental hardware to be precisely located in the ion beam path.

The collision cell 5 (CC5, as is shown in Figure 2.7), where collision-induced emission is observed, is a 16 mm internal diameter aluminum cylindrical tube with a thickness of 4.7 mm and a length of 16mm. A 6 mm diameter circular hole is drilled at the top of the tube and covered by a fused silica (UV grade) window (Edmund Optics, 10 mm diameter, 1mm thickness) for photon transmission. Above the collision cell, a fused silica window of 1 cm diameter (Optikon WU-25) is embedded in the lid of the 3FFR to allow photons to exit and be detected.

Photons transmitted through the windows are dispersed by an Acton spectraPro 275 spectrograph (27.5 cm focal length, 1200 g mm^{-1} holographic grating) and detected with an

Andor thermoelectrically cooled charge-coupled device (CCD) detector (Andor DV 401-UV, front-illuminated with UV coating). The CCD detector can be cooled to -42 ^{o}C with air and to -49 ^{o}C when water cooling is used. In the experiment, the CCD is cooled to a temperature of -35 ^{o}C.

Optical emissions from 190-1020 nm were recorded by the Andor MCD 2.63.1.8 program in 14 separate fragments, each being 50-79 nm wide. The entrance slit width of the spectrograph can be adjusted from 0 to 3 mm. The emission peak width decreases as the slit narrows, increasing the spectral resolution. To maximize emission signal intensity, the slit width is set to 3.0 mm, producing a spectral resolution (full width at half maximum) of 8.5 nm for atomic lines.

A detailed description of the experimental procedure to obtain a collision-induced emission spectrum is given in chapter 3.

REFERENCES

[1] Solomon, P. M.; Klemperer, W., *Astrophys. J.* **1972**, *178*, 389.

[2] Klemperer, W., *Nature* **1970**, *227*, 1230.

[3] Mottelay, P. F., *Bibliographical History of Electricity and Magnetism* Read Books, **2007**, p. 114.

[4] Bhardwaj' A.; Gladstone, G. R., *Adv. Space Res.* **2000**, *26*, 1551.

[5] Mauk, B. H.; Clarke, J. T.; Grodent, D.; Waite, J. H. Jr.; Paranicas, C. P.; Williams, D. J., *Nature* **2002** *415*, 1003.

[6] Petrie, S.; Bohme, D. K., *Top. Curr. Chem.* **2003**, *225*, 37.

[7] Ferguson, E. E.; Fehsenfeld, F. C.; Albritton, D. L., *Ion chemistry of the earth's atmosphere*, Academic Press, New York, **1979**.

[8] McLuckey, S. A., *J. Am. Soc. Mass Spectrom.* **1992**, *3* 599.

[9] Mabud, M. A.; Dekrey, M. J.; Cooks, R. G., *Int. J. Mass Spectrom. Ion Processes* **1985**, *67*, 285.

[10] Zubarev, R. A.; Kelleher, N. L.; McLafferty, F. W., *J. Am. Chem. Soc.* **1998**, *120*, 3265.

[11] Syka, J. E.; Coon, J. J.; Schroeder, M. J.; Shabanowitz, J.; Hunt D. F. , *Proc. Natl. Acad. Sci. U.S.A.* **2004**, *101*, 9528.

[12] Thomson, J. J., *Rays of Positive Electricity and Their Application to Chemical Analysis*, Longmans, London, **1913.**, p.

[13] Aston, F. W., *Proc. Cambridge Philos. Soc.* **1919**, *19*, 317.

[14] Haddon, W. K.; McLafferty, F. W., *J. Am. Chem. Soc.* **1968**, *90*, 4745.

[15] McLafferty, F. W.; Bente, P. F.; Kornfeld, F. C.; Tsai, S.-C.; Howe, I., *J. Am. Chem. Soc.* **1973**, *95*, 2120.

[16] Holmes, J. L.; Aubry, C.; Mayer, P. M., *Assigning structures to ions in mass spectrometry*, CRC, Boca Raton, **2007.**

[17]Yost, R. A.; Enke, C. G., *J. Am. Chem. Soc.* **1978**, *100*, 2274.

[18] Marzluff, E. M.; Campbell, S.;. Rodgers, M. T.; Beauchamp, J. L., *J. Am. Chem. Soc.* **1994**, *116*, 7787.

[19] McLuckey, S. A.; Goeringer, D. E., *J. Mass Spectrom.* **1997**, *32*, 461.

[20] Baer, T.; Hase, W. L., *Unimolecular reaction dynamics, theory and experiments*, Oxford University, New York, **1996**.

[21] Baer, T.; Mayer, P. M., *J. Am. Soc. Mass Spectrom.* **1997**, *8*, 103.

[22] Shirts, R. B., *Collision Theory and Reaction Dynamics*, Wiley, New York, **1986**, p. 25.

[23] Cooks, R. G., *Collision Spectroscopy*, Plenum, New York, **1978**, p.

[24] Laidler, K. J.; Meiser, J. H., *Physical Chemistry*, Houghton Mifflin Company, Boston, **1999**, p.

[25] Durup, J. , *Mechanisms of collision-induced dissociation of fast ions*, University Park, Baltimore, **1970**, p. 921.

[26] Condon, E. U., *Amer. J. Phys.* **1947**, *15*, 366.

[27] Reid, C. J., *Int. J. Mass Spectrom. Ion Processes* **1990**, *101*, 35.

[28] Reid, C. J., *Int. J. Mass Spectrom. Ion Processes* **1991**, *105*, 191.

[29] Massey, H. S. W.; Burhop, E. H. S.; Gilbody, H. B., *Electronic and ionic impact phenomena*, Clarendon, Oxford, **1974**, p.

[30] Nikitin, E.E., *Theory of Elementary Atomic and Molecular Processes in Gases*, Clarendon, Oxford, **1974**.

[31] Massey, H. S. W., *Rep. Prog. Phys.* **1949**, *12*, 248.

[32] Massey, H. S. W.; Burhop, E. H. S., *Electronic and ionic impact phenomena*, Clarendon, Oxford, **1952**.

[33] Landau, L. D., *Phys. Zeits. Sowjetunion* **1932**, *2*, 46.

[34] Stueckelberg, E. C. G., *Helv. Phys. Acta* **1932**, *5*, 370.

[35] Zener, C., *Proc. R. Soc A* **1932**, *137*, 696.

[36] Mahan, B. H., *Acc. chem. Res.* **1970**, *3*, 393.

[37] Mahan, B.H., *J. chem. Phys.* **1970**, *52*, 5221.

[38] Chesnavich, W. J.; Bowers, M. T., *Gas Phase Ion Chemistry, Vol. l*, Academie, New York, **1979**, p. 119.

[39] Kern, K.; Schlier, Ch., *Z. Phys. D- Atoms, Molecules and Clusters* **1986**, *1*, 391.

[40] Shimma, S.; Nagao, H.; Giannakopulos, A. E.; Hayakawa, S.; Awazu, K.; Toyoda, M., *J. Mass Spectrom.* **2008**, *43*, 535.

[41] Pittenauer, E.; Allmaier, G., *Comb. Chem. High Throughput Screen* **2009**, *12*, 137.

[42] Belgacem, O.; Stubiger, G.; Allmaier, G.; Buchacher, A.; Pock, K. , *Biologicals* **2007**, *35*, 43.

[43] Stuebiger, G., Unterweger, H., Buchbauer, G.; Krist,S., *Rapid Commun. Mass Spectrom.* **2009**, *23*, 2711.

[44] Brenton, A. G., *J. Mass Spectrom.* **1995**, *30*, 657.

[45] Lock, C. M.; Brenton, A. G.; Mathur, D. , *Int. J. Mass Spectrom. Ion Processes* **1997**, *165*, 119.

[46] Greenwood, J. B.; Burns, D.; McCullough, R. W.; Geddes, J.; Gilbody, H. B. *J. Phys. B., At. Mol. Opt. Phys.* **1996**, *29*, 5867.

[47] Gilbody, H. B.; McCullough, R. W., *J. Phys.: Conf. Ser.* **2004**, *2*, 199.

[48] Huber, B. A.; Kahlert, H. J.; Wiesemann, K., *J. Phys. B* **1984**, *17*, 2883.

[49] Fournier, P.; VandeRunstraat, C. A.; Govers, T. R.; Schopman, J.; deHeer, F. J.; Los, J., *Chem. Phys. Lett.* **1971**, *9*, 426.

[50] Laramee, J. A.; Carmody, J. J.; Cooks, R. G., *Int. J. Mass Spectrom. Ion Phys.* **1979**, *31*, 333.

[51] Laramee, J. A.; Hemberger, P. H.; Cooks, R. G., *Int. J. Mass Spectrom. Ion Phys.* **1980**, *33*, 231.

[52] Hubik, A. R.; Hemberger, P. H.; Laramee, J. A.; Cooks, R. G., *J. Am. Chem. Soc.,* **1980**, *102*, 3997.

[53] Todd, P. J.; McLafferty, F. W., *Tandem Mass Spectrometry*, Wiley, New York, **1983**, p.

[54] Singh, S.; Harris, F. M.; Boyd, R. K.; Beynon, J. H. , *Int. J. Mass Spectrom. Ion Processes* **1985**, *66*, 131.

[55] Moore, J. H.; Doering, J. P., *Phys. Rev.* **1969**, *177*, 218.

[56] Lipeles, M. J., *Chem. Phys. Lett.* **1969**, *51*, 1252.

[57] Bregman-Reisler, H.; Doering, J. P., *Phys. Rev. A* **1974**, *9*, 1152.

[58] Kelley, J. D.; Bearman, G. H.; Harris, H. H.; Leventhal, J. J., *Chem. Phys. Lett.* **1977**, *50*, 295.

[59] Kelley, J. D.; Bearman, G. H.; Harris, H. H.; Leventhal, J. J., *J. Chem. Phys.* **1978**, *68*, 3345.

[60] Ehbrecht, A.; Mustafa, N.; Ottinger, C.; Herman, Z., *J. Chem. Phys.* **1996**, *105*, 9833.

[61] Mayer, P. M.; Poon, C., *J. Am. Soc. Mass Spectrom.* **2008**, *19*, 1551.

[62] Holmes, J. L.; Mayer, P. M., *J. Phys. Chem.* **1995**, *99*, 1366.

[63] Mayer, P. M., *Mass Spectrometry, Encyclopedia of Chemical Physics and Physical Chemistry, Vol. 2*, Institute of Physics, Bristol, **2001**, p. 1147.

[64] Cooks, R. G.; Beynon, J. H.; Caprioli, R. M.; Lester, G. R.*Metastable Ions*, Elsevier, Amsterdam, **1973**.

[65] Traeger, J. C.; Mommers, A. A., *Org. Mass Spectrom.* **1987**, *22*, 592.

[66] Holmes, J. L., *Org. Mass Spectrom.* **1985**, *20*, 169.

[67] Goldberg, N.; Schwarz, H., *Acc. Chem. Res.* **1994**, *27*, 347.

[68] McLafferty, F. W., *Science* **1990**, *247*, 925.

[69] Schalley, C. A.; Hornung, G.; Schroder, D.; Schwarz, H., *Chem. Soc. Rev.* **1998**, *27*, 91.

[70] Wesdemiotis, C.; McLafferty, F. W., *Chem. Rev.* **1987**, *87*, 485.

Chapter 3

Fluorescence from the A $^2\Sigma^+$ state suggests a non-Franck-Condon $N_2O^{+\bullet}$ vibrational state population after keV collisional activation with helium.

3.1 Introduction

The triatomic ion $N_2O^{+\bullet}$ is isoelectronic with NCO, $CO_2^{+\bullet}$ and BO_2. It is the intermediate in an important ion-molecule reaction in the upper atmosphere.[1]

$$O^{+\cdot}(^4S_u) + N_2\ (X^1\Sigma_g^+) \rightarrow\ N_2O^{+\bullet}\ (A\ ^2\Sigma^+) \rightarrow NO^{+\cdot}(X^1\Sigma^+) + N(^4S) \qquad (1)$$

The dominant emission band systems of $N_2O^{+\bullet}$, extending from 335 to 405 nm, are the $A\ ^2\Sigma^+ \rightarrow X\ ^2\Pi^+$ transitions from 3 dominant levels 1^0, 1^1, 3^1 of the A state. Here the capital number represents the normal vibrational mode involved (1 being the symmetric stretch, 2 being the degenerate bend and 3 the asymmetric stretch), the superscript and subscript represent the vibrational quanta in the upper and lower state, respectively).[2] Higher excited states of $N_2O^{+\bullet}$, such as the B and C states, are predissociative and not observed in emission spectra.[3] Also, the state crossings between the potential surfaces of the predissociative states and that of the $A\ ^2\Sigma^+$ state occurs near the bottom of the potential surface of the A state, restricting the number of vibrational levels in which the A state is formed.[4-6]

Emission cross sections and vibrational level ratios of $N_2O^{+\bullet}$ have been measured by a variety of techniques including photon ionization, Penning ionization, electron impact and charge exchange.[7-10] It is well known that when an ion is formed by vertical excitation, the vibrational branching ratio is equal to the ratio of the corresponding Franck-Condon factors. Tokue and coworkers determined the vibrational distributions of the 1^1 and 3^1 levels relative to the 1^0 level of the A state, using Penning ionization.[11] The branching ratio for the 1^1 level strongly depended on the excitation energy, showing non-Franck-Condon behavior, resulting from autoionization and shape resonant ionization, indicating that a vertical transition is not always available.

In this study, we have focused on keV (laboratory frame) ion-molecule collisional activation. In mass spectrometry, collisional activation is an essential method for

fragmenting ions to gain further structure determination.[12-16] When a projectile ion with keV translational energy collides with a relatively stationary target gas moiety, a portion of the ion's translational energy is converted to internal energy, sufficient for the ion to undergo dissociation reactions. Of the potential mechanisms for this energy transfer, the most widely applicable one is the curve-crossing mechanism.[17-19] The qualitative and quantitative description of curve crossing adiabatic energy transfer to produce electronic excitation has been described by Massey, Burhop, Gilloby and Nikitin. [20,21] As shown in Figure 1.7, [17] during the collision process, when the projectile ion approaches the target, the energy of the collision complex increases along the adiabatic curve of the ground state, until the ground state potential surface crosses with that of an excited state through point C. The strength of the non-adiabatic coupling of the two curves can be represented as the Massey parameter, ξ, in the Massey equation $\xi = a\Delta E / h\upsilon$ (ΔE is the smallest energy gap between two adiabatic states, a is the width of the nonadiabatic interaction region and υ is the classical nuclear velocity). The curve-crossing then brings about a radiationless transition between the ground and electronic excited state of the collision complex. During separation of the collision complex, the projectile ion may return to its original energy surface or remain in an excited electronic state. In the latter case the electronic excitation can be removed by emission of a photon or converted to ro-vibrational excitation of the ground state by IVR (intramolecular vibrational redistribution). As the relative velocity of the interacting pair increases the time of interaction decreases, decreasing the Massey parameter, thereby increasing the probability that the system crosses into an excited state. Thus, this direct T→E (translational to electronic) energy transfer is operable at keV collision energies.

Recent work by our group showed that for keV $N_2^{+\bullet}$/He and $CO_2^{+\bullet}$/He collisions, the relative emission intensity between the fragments and the projectile ions are independent of ion translational energy in the 3-8 keV range, results consistent with the formation of a discrete distribution of excited states by the curve-crossing mechanism.[22-24] The purpose of this paper is to extend our CIE study to the $N_2O^{+\bullet}$/He system, and by comparing our results to those obtained from other activation methods, to get a clearer picture of the mechanism of high energy ion-molecule collisions.

3.2 Experimental procedures

All experiments were performed on a modified VG ZAB mass spectrometer[14] with an added third field-free region (3FFR) as previously described.[25, 26]

$N_2O^{+\bullet}$ ions were generated from N_2O by 80-90 eV electron ionization in the ion source of the instrument. The ions were transmitted to the 3FFR where they collided with the target gas in the collision cell at a collision gas pressure that reduces the pre-cell ion flux by 10% (i.e. essentially single collision conditions).[14] With 80-90 eV electrons, ionization of $N_2O^{+\bullet}$ could result in $N_2O^{+\bullet}$ A $^2\Sigma^+$ being formed in the ion source.[27] However, the radiative lifetime of the A state is shorter than 400 ns.[28-30] When compared to the time required for the ions to reach the collision chamber, which ranges from 17 to 34 μs depending on the accelerating voltage, virtually all ions that are formed initially in the A $^2\Sigma^+$ would have returned to the ground state by the time they collide with the target gas.

A spectrograph (Acton SpectraPro 275, 27.5 focal length, 1200 g mm^{-1} holographic grating) and a thermoelectrically-cooled charge-coupled device (CCD) detector (Andor DV401-UV, front-illuminated with UV coating) have been installed above the collision cell for the detection of photon emissions resulting from ion-target collisions.[22] Emissions from the excited state species were directly observed with the CCD detector cooled to a temperature of -35 ºC. The time window of observation ranges from 30-60 ns for 8 keV to 4 keV $N_2O^{+\bullet}$. The entrance slit of the spectrograph was set to 3.0 mm, providing a spectral resolution of 8.5 nm (measured at full width at half-height for atomic lines). Optical emissions were recorded from 190-1020 nm using the Andor MCD 2.63.1.8 program and were recorded in 14 separate segments, each being 50-70 nm wide. Two accumulations of 30 minutes were collected at 8 keV ion translational energy for each segment at full vertical binning reading mode. For other ion translational energies, the total acquisition time for each of the separate segments ranged from 1 hour to 4 hours. Each segment was background subtracted and background spectra were collected prior to signal acquisition with exactly the same conditions except without an ion beam. Spectral spikes resulting from cosmic rays were removed digitally by the program. Horizontal binning was performed manually in the ASCII file by combining data of every 20 pixel columns and the overlapping portion of the spectrum at the two ends of each window was averaged.

A higher-resolution spectrum (330-400 nm) was obtained by reducing the entrance slit width to 1.0 mm, resulting in a spectral resolution of 3.0 nm, and the data acquisition time of each segment was increased to 4 hours.

3.3 Results and discussion

3.3.1 Emission spectrum from $N_2O^{+\bullet}$/He collisions

The emission spectrum obtained from $N_2O^{+\bullet}$/He collisions at 8 keV ion translational energy is shown in Figure. 3.2, and this is compared to those obtained at 6 and 4 keV in Figure 3.3. A summary of the peak and transition assignments is presented in Table 3.1. Emission signals observed in the lower wavelength region (330-400 nm) correspond to the $N_2O^{+\bullet}$ ($A\ ^2\Sigma^+ \rightarrow X\ ^2\Pi^+$) system. Three dominant vibrational bands, 1^1, 3^1 and 1^0 were observed. Other peaks observed in the spectrum arise from the emissions of the target gas He and electronically excited fragments $N^{+\cdot}$, N, $O^{+\cdot}$ and $O^{\cdot}$.

In our earlier study of the $CO_2^{+\bullet}$/He system,[24] two obvious band emissions resulting from electronic transitions of the $B\ ^2\Sigma_u^+$ and $A\ ^2\Pi_u$ states to the ground $X\ ^2\Pi_g$ state of $CO_2^{+\bullet}$ were observed. The vibrational progression in $CO_2^{+\bullet}$ $A\ ^2\Pi_u \rightarrow X\ ^2\Pi_g$ transition showed emission from high vibrational levels (7, 0, 0) in the $A\ ^2\Pi_u$ state. In the present $N_2O^{+\bullet}$/He system, only the expected $A\ ^2\Sigma^+ \rightarrow X\ ^2\Pi^+$ transition was observed, and in addition, emissions arise only from low (indeed v = 1) vibrational levels of the A state. Also, the $CO_2^{+\bullet}$/He CIE spectra only showed 2 atomic emissions from the oxygen radicals O(^{5}P) and O(^{3}P), meanwhile in the $N_2O^{+\bullet}$/He CIE spectra, 9 more atomic emissions from fragments $N^{+\cdot}$, N, $O^{+\cdot}$ and O were observed. The intensity ratio between the molecular emission and atomic

emission from O(^{5}P) and O(^{3}P) were calculated: $I_{N_2O^+} / I_{O(^5P)}$ and $I_{CO_2^+} / I_{O(^5P)}$ are 19 and 31; $I_{N_2O^+} / I_{O(^5P)}$ and $I_{CO_2^+} / I_{O(^5P)}$ are 11 and 22, respectively, indicating the greater tendency to form excited fragments in the collisional activation of $N_2O^{+\bullet}$, in agreement with the dissociative nature of the $N_2O^{+\bullet}$ higher excited states.[3,31] According to *ab initio* calculations of the potential surfaces by Komiha,[31,32] shown in Figure 3.4, two repulsive potential curves of $1^4\Pi$ and $1^4\Sigma^-$ state curve-cross with the A and X state surfaces, leading to different state specified fragments. Also, there are avoided crossings between $1^4\Sigma^-$ and $2^4\Sigma^-$ state. We have identified a number of higher energy fragments in our CIE spectra indicative of the dissociation of higher electronic states of $N_2O^{+\bullet}$, Table 3.1. This example shows that one benefit of the CIE experiment is that it not only offers rich information on the excited states of the projectile ion generated in a collision, but also on the excited states of CID products.

3.3.2 Relative emission intensities as a function of ion translational energy

The emission spectra over the wavelength range of 280-950 nm from 8 keV to 4 keV ion translational energy are presented in Figure 3.3. The intensities of the emissions from the target gas cannot be directly compared with those from the projectile ions or the fragments since the spatial distribution of collisions across the collision cell is unknown. The relative emission intensities of $N_2O^{+\bullet}$, $N^{+\cdot}$, $O^{+\cdot}$ and O at various collision energies are presented in Figure 3.5. The intensities have been corrected for their difference in radiative lifetime, as only a portion of the emission from each excited-state species is detected. The correction was performed based on our previous conclusion that the majority of collision events take place under the window.[22] In Figure 3.5, all the points falls on y=x line indicating that the relative

emission intensities do not change with ion translational energy, supporting the curve-crossing mechanism for collisional excitation which will produce the same distribution of excited states in the projectile ion, only the probability with which they are formed changes with translational energy according to the Massey equation.

3.3.3 Relative band strength in the A $^2\Sigma^+$ state $N_2O^{+\bullet}$

Figure 3.6 shows a higher resolution CIE spectrum of the $N_2O^{+\bullet}$ A $^2\Sigma^+ \rightarrow$ X $^2\Pi^+$ system in the 330-400 nm region produced by 8 keV collisions. The three bands 1_0^0, 1_0^1 and 3_1^1 are located at 354 nm, 338nm and 347 nm, respectively, together with related transitions $1\,{}^{0}_{1}$, $1\,{}^{0}_{2}$ and the combination band $1\,{}^{0}_{1}\ \ 3\,{}^{1}_{1}$. Each $N_2O^{+\bullet}$ A $^2\Sigma^+ \rightarrow$ X $^2\Pi^+$ vibrational band consists of a pair of subbands with nearly equal intensity due to the spin-orbit splitting of the X $^2\Pi^+$ state. The band emission intensities have been lifetime corrected for later calculation of the relative intensities.[30]

The relative emission cross section is known to be related to the vibrational branching ratios and emission intensities as described in equations below

$$\frac{\sigma_{em}(v_i^{'}, v_k^{''})}{\sigma_{em}(v_j^{'}, v_l^{''})} = . \frac{I_{em}(v_i^{'}, v_k^{''}) / \varepsilon(v_i^{'}, v_k^{''})}{I_{em}(v_j^{'}, v_l^{''}) / \varepsilon(v_j^{'}, v_l^{''})} \quad (2)$$

$$\frac{\sigma_{em}(v_i^{'}, v_k^{''})}{\sigma_{em}(v_j^{'}, v_l^{''})} = . \frac{\nu(v_i^{'}, v_k^{''})^3 q(v_i^{'}, v_k^{''}) \sigma(v_i^{'}) f(v_i^{'})}{\nu(v_j^{'}, v_l^{''})^3 q(v_j^{'}, v_l^{''}) \sigma(v_j^{'}) f(v_j^{'})} \quad (3)$$

where $I_{em}(\upsilon',\upsilon'')$ $q(\upsilon',\upsilon'')$ $\varepsilon(\upsilon',\upsilon'')$ and $\sigma_{em}(\upsilon',\upsilon'')$ are emission intensity, Franck-Condon factor, transition frequency and cross section, respectively, for the $\upsilon' - \upsilon''$ band. The $f(\upsilon')$ and $\sigma(\upsilon')$ represent the fluorescence versus predissociation branching ratio and excitation cross sections, respectively, for the υ' level of the A state. By transforming the equations and obtaining the $f(\upsilon')$ and $q(\upsilon',\upsilon'')$ value based on the photoelectron-photoion coincidence measurement,[27] the branching ratios can be determined from the relative intensities of the vibrational bands.[11,13] The band strength of the 1_0^1 and 3_1^1 relative to that of the 1_0^0 band are listed in Table 3.2, along with values from photoionization and Penning ionization. In photoionization, $I(1_0^1)/I(1_0^0)$ and $I(3_1^1)/I(1_0^0)$ maintain constant values of 0.27 and 0.05, respectively, when the photon energy is larger than 45 eV. Since the energy range above 45 eV is free of autoionization and shape resonance, these values are regarded as the branching factors in the Franck-Condon limit. Penning ionization obtained by Ne(^{3}P: 16.6eV) and He(2^3S: 19.9eV) is similar to photoionization, showed non-FC behavior when the excitation energy was lower than 45 eV. Since autoionization is from the Rydberg state of the neutral molecule and shape resonant ionization is due to the interaction of the photoelectron or metastable atom and the target neutral molecule,[34-36] neither of them have relevance to the $N_2O^{+\bullet}$/He system in this study. In the present CIE experiments, the $I(1_0^1)/I(1_0^0)$ and $I(3_1^1)/I(1_0^0)$ ratios in the $N_2O^{+\bullet}$ A state show obvious deviation from Franck-Condon behavior, unlike our previous observations with $CO_2^{+\bullet}$/He.[23] This is a clear example of collisional excitation producing a decidedly non-Franck-Condon distribution of vibrational levels. This must be due to the fact that many predissociative states (such as the $1^4\Pi$ and $1^4\Sigma^-$ states, Figure 3.4) cross with, and populate the vibrational levels of, the A state

of $N_2O^{+\bullet}$.

3.4 Conclusion

Using a modified VG-ZAB mass spectrometer, the emission from electronic excited projectile $N_2O^{+\bullet}$ ions and their collision induced dissociation products have been observed, giving a relatively full picture of the activation process. Collision-induced emission spectroscopy produced from high keV $N_2O^{+\bullet}$/He collisions showed that the relative populations of electronically excited $N_2O^{+\bullet}$, N, O, $O^{+\cdot}$ and $N^{+\cdot}$ states remains constant as the collision energy is increased from 4 keV to 8 keV, a result consistent with the curve-crossing mechanism of collisional activation. The relative vibrational branching ratios of $N_2O^{+\bullet}$ after collisional activation were compared with those obtained by different activation processes. Results indicate that due to the complex curve-crossing between predissociation states and the A and X states of $N_2O^{+\bullet}$, the vibrational population in the A state appears more evenly distributed than that resulting from Franck-Condon photoexcitation. This was also different than that seen in the case of $CO_2^{+\bullet}$/He collisions and is the result of the many predissociative higher energy states populating the vibrational levels of $N_2O^{+\bullet}$ A $^2\Sigma^+$.

REFERENCES

(1) Danilov, A.D., *Chemistry of the ionosphere*. Plenum: New York, 1970.

(2) Callomon, J.H.; Creutzberg F. *Phil. Trans. R. Soc. London*. **1974**, 277, 157.

(3) Brehm, B.; Frey, R.; Küstler, A.; Frey, A.; Eland J.H.D. *Int. J. Mass Spectrom. Ion Phys*. **1974**, 13, 251.

(4) Fellows, C. E.; Vervloet, M. *Chem. Phys.* **2001**, 264, 203.

(5) Hopper, D.G. *J. Am. Chem. Soc.* **1978**, 100, 1019.

(6) Richard-Viard, M.; Delboulbé, A.; Vervloet, M. *Chem. Phys.* **1996**, 209, 159.

(7) Berkowitz, J.; Eland, J.H.D. *J. Chem. Phys.* **1977**, 67, 2740.

(8) Ferrett, T.A.; Parr, A.C.; Southworth, S.H.; Dehmer, J.L. *J. Chem. Phys.* **1989**, 90, 1551.

(9) Tsuji, M.; Tsuji, K.; Nishimura, Y. *Int. J. Mass Spectrom. Ion Phys.* **1979**, 30, 175.

(10) Tsuji, M.; Maier J.P. *Chem. Phys.* **1988**, 126, 435.

(11) Tokue; I.; Kudo, T.; Ito Y. *Chem. Phys. Lett.* **1992**, 199, 435.

(11) Holmes, J.L.; Mayer, P.M.; Aubry, C., *Assigning Structures to Ions in the Mass Spectrometry.* CRC: New York, 2007.

(13) Cooks, R.G., *Collision Spectroscopy*. Plenum: New York, 1978.

(14) Holmes, J.L. *Org. Mass Spectrom.* **1985**, 20, 169.

(15) Levsen, K.; Schwarz, H. *Mass Spectrom. Rev.* **1983**, 2, 77.

(16) Todd, P.J.; Mclafferty, F.W., *Tandem Mass Spectrometry.* Willey: New York, 1983.

(17) Mayer, P.M; Poon, C. *Mass Spetrom. Rev.* **2009**, 28, 612.

(18) Durup, J., *Recent Developments in Mass Spectrometry.* University Park: Baltimore, 1970.

(19) Mcluckey S.A. *J. Am. Soc. Mass Spectrom.* **1992**, 3, 599.

(20) Massey, H.S.W; Burhop, E.H.S.; Gilbody H.B., *Electronic and Ionic Impact Phenomena*. Clarendon: Oxford, 1974.

(21) Nikitin, E.E., *Theory of Elementary Atomic and Molecular Processes in Gases.* Clarendon: Oxford, 1974.

(22) Poon, C.; Mayer, P.M. *J. Phys. Chem. A* **2007**, 111, 777.

(23) Poon, C.; Mayer, P.M. *J. Am. Soc. Mass Spectrom.* **2008**, 19, 1551.

(24) Poon, C.; Lin, Y.; Mayer, P.M. *J. Phys. Chem. A* **2008**, 112, 7761.

(25) Burgers, P.C.; Holmes, J.L.; Szulejko, J.E.; Mommers, A.A.; Terlouvw, J.K. *Org. Mass Spectrom.* **1983**, 18, 254.

(26) Holmes, J.L.; Mayer, P.M.; Mommers, A.A. *Int. J. Mass Spectrom. Ion Process.* **1994**, 135, 213.

(27) Hiroshi, K.; Shimada, H.; Kobayashi, M.; Tokue, I.; Ito, Y. *Chem. Phys. Lett.* **1991**, 109, 179.

(28) Van Sprang, H.A.; De Heer, F.J. *Chem. Phys.* **1978**, 33, 65.

(29) Ibuki, T.; Sugita, N. *J. Chem. Phys.* **1984**, 80, 4625.

(30) Maier, J.P.; Thommen, F. *Chem. Phys.* **1980**, 51, 319.

(31) Richard-Viard, M.; Atabek, O.; Dutuit, O.; Guyon P.M. *J. Chem. Phys.* **1990**, 93, 8881.

(32) Komiha, N., *Thèsè de Troisième cycle*. Université Pierre et Marie Curie, Paris, 1981.

(33) Kelly, L.A.; Duffy, L.M.; Space, B; Poliakoff, E.D.; Roy, P.; Southworth, S.H.; White, M.G. *J. Chem. Phys.* **1989**, 90, 1544.

(34) Braunstein, M.; Mckoy, V. *J. Chem. Phys.* **1989**, 90, 1535.

(35) Niehaus, A. *Advan. Chem. Phys.* **1981**, 45, 399.

(36) Tsuji, M.; Obase, H.; Endoh, M.; Nishimura, Y. *J. Chem. Phys.* **1988**, 89, 6753.

(37) Bashkin, S.; Stoner, J.O., *Atomic Energy Levels & Grotrian Diagrams 1*. North-Holland: New York, 1975.

(38) Wiese, W.L.; Smith, M.W.; Glenno, B.M., *Atomic Transition Probabilities*, National Bureau of Standards: Washington, D.C., 1966.

Table 3.1. Observed emissions in Figure and their corresponding radiative lifetimes

Transition			τ (ns)	λ (nm)	Ref.
$N_2O^{+\bullet}$	$A\ ^2\Sigma^+ \rightarrow X\ ^2\Pi^+$	$1\,{}^{1}_{0}$	180	338	(29)
		$3\,{}^{1}_{1}$	199	344	
		$1\,{}^{0}_{0}$	243	355	
		$1\,{}^{0}_{1}$	243	368	
		$1\,{}^{0}_{2}$	243	383	
		$1^0_1 3^1_1$	195	360	
$O^{+\cdot}$	$(3p)^6P \rightarrow (3s)^6S^0$		11	446	(36, 37)
	$(3p)^4D^0 \rightarrow (3s)4P$		39	468	
O	$(3d)\ ^5P \rightarrow (3s)\ ^5S^0$		27	779	(36, 37)
	$(3p)\ ^4P^0 \rightarrow (3s)\ ^4P$		34	822	
	$(3p)\ ^3P \rightarrow (3s)\ ^3S^0$		31	847	
$N^{+\cdot}$	$(3d)\ ^3F^0 \rightarrow (3p)\ ^3D$		8	503	(36, 37)
	$(3p)\ ^3S \rightarrow (3s)\ ^3P^0$		13	503	
	$(3p)\ ^3D \rightarrow (3s)\ ^3P^0$		18	570	
	$(3p)\ ^3P \rightarrow (4l)\ ^3P^0$		33	659	
N	$(3p)\ ^4S^0 \rightarrow (3s)\ ^4P$		31	748	(36, 37)
	$(3p)\ ^4D^0 \rightarrow (3s)\ ^4P$		44	872	
	$(3d)\ ^2P \rightarrow (3p)\ ^2S^0$		52	906	
	$(3p)\ ^2F^0 \rightarrow (3s)\ ^2D$		39	906	
He	$(3p)\ ^3P^0 \rightarrow (2s)\ ^3S$		18	389	(36, 37)
	$(3d)\ ^3D \rightarrow (2p)\ ^3P^0$		14	590	
	$(3d)\ ^1D \rightarrow (2p)\ ^1P^0$		16	671	

Table 3.2 Band emission intensities of 1_0^1 and 3_1^1 relative to the $1\,{}^{0}_{0}$ band of $N_2O^{+\bullet}$ (A → X).

Method	Ionizing energy (eV)	$I(1_0^1)/I(1_0^0)$	$I(3_1^1)/I(1_0^0)$	Ref.
CIE		0.227 (2)	0.124 (3)	This work
PI	17.1-26.8	0.162(17)	0.057(6)	38
	17	0.237(6)	0.047(2)	32
	20	0.113(4)	0.038(3)	
	45-53	0.272(6)	0.049(3)	
He(2^3S)-FA	Thermal	0.137(12)	0.062(3)	9
Ne(^{3}P)-FA	Thermal	0.208(43)	0.019-0.061(9)	10
He(2^3S)-FA	0.15	0.105(7)	0.045(3)	11

[a] PI: photoionization; FA: Penning ionization

[b] Numbers in parentheses represent uncertainties attached to the last digit

Figure Captions

Figure 3.1. A simplified diagram illustrating curve-crossings during ion-target collisions. The behavior of the excited states is drawn as a single entity.

Figure 3.2 Collision-induced emission spectra (190-1020 nm) of $N_2O^{+\bullet}$/He collisions at 8 keV. Collision gas pressure corresponded to 90% ion beam transmission. The arrows with different shapes  represent photoemission from $O^{+\cdot}$, $N^{+\cdot}$, He, N and O, respectively.

Figure 3.3 Collision-induced emission spectra (190-1020 nm) of $N_2O^{+\bullet}$/He collisions at 8, 6 and 4 keV. Collision gas pressure corresponded to 90% ion beam transmission.

Figure 3.4 Ab initio potential curves for a collinear $N_2O^{+\bullet}$ geometry calculated by Komiha (Ref. 32). Reprinted with permission from Richard-Viard, M.; Atabek, O.; Dutuit, O.; Guyon P.M. *J. Chem. Phys.* **1990**, 93, 8881. Copyright 1990, American Institute of Physics.

Figure 3.5 The plot of the lifetime-corrected relative emission intensities of $N_2O^{+\bullet}$, $N^{+\cdot}$, N, and O at various ion translational energies vs. those at 8 keV. All ion translational energies were obtained by varying the source accelerating voltages. Spectra are normalized to the ion flux at 8 keV. Collision gas pressure corresponded to 90% ion beam transmission.

Figure 3.6 Collision-induced emission spectrum (330-400 nm) of 8 keV $N_2O^{+\bullet}$/He collisions obtained with an entrance slit width of 1.0 mm (total data acquisition time per section: 8 hours).

Figure. 3.1: refer to Figure 1.7 in the introduction part.

Figure. 3.2

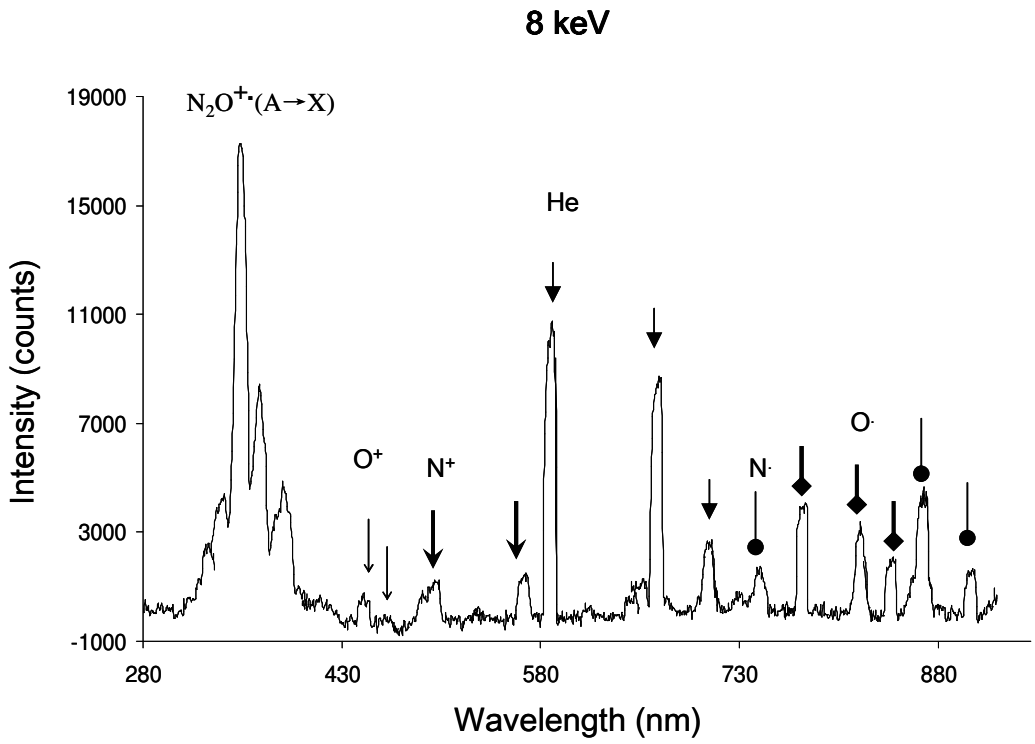

Figure 3.3

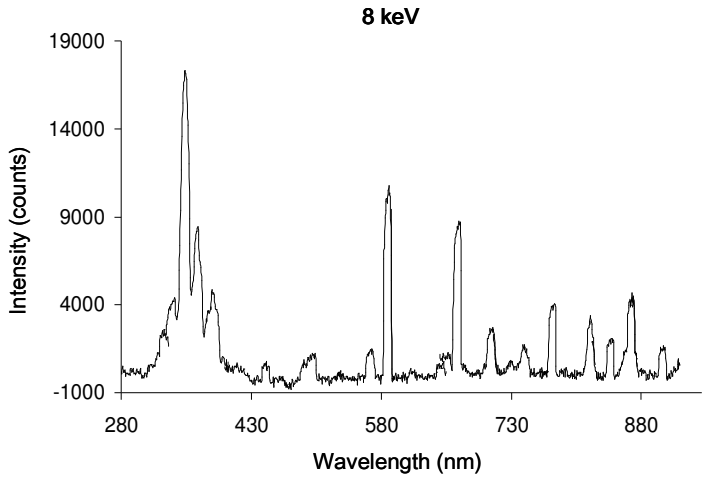
8 keV
19000
14000
9000
4000
-1000
Intensity (counts)
280
430
580
730
880
Wavelength (nm)

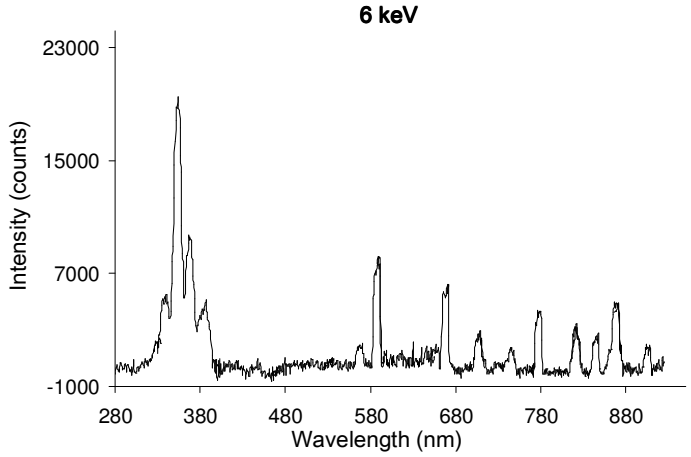
6 keV
23000
15000
7000
-1000
Intensity (counts)
280
380
480
580
680
780
880
Wavelength (nm)

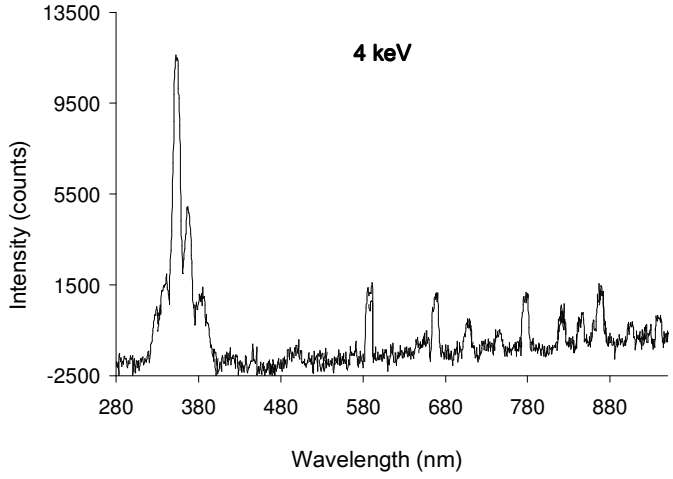
4 keV
13500
9500
5500
1500
-2500
Intensity (counts)
280
380
480
580
680
780
880
Wavelength (nm)

Figure 3.4

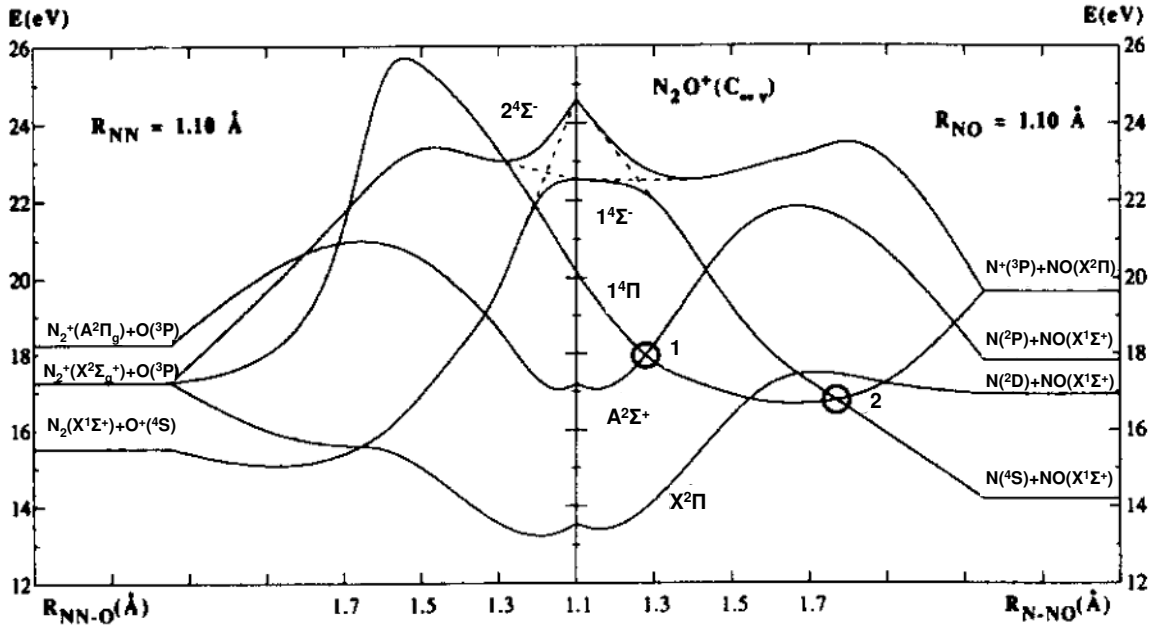
E(eV)
E(eV)
$N_2O^+(C_{\infty v})$
R_{NN} = 1.10 Å
R_{NO} = 1.10 Å
$2^4\Sigma^-$
$1^4\Sigma^-$
$1^4\Pi$
$A^2\Sigma^+$
$X^2\Pi$
1
2
$N_2^+(A^2\Pi_g)+O(^3P)$
$N_2^+(X^2\Sigma_g^+)+O(^3P)$
$N_2(X^1\Sigma^+)+O^+(^4S)$
$N^+(^3P)+NO(X^2\Pi)$
$N(^2P)+NO(X^1\Sigma^+)$
$N(^2D)+NO(X^1\Sigma^+)$
$N(^4S)+NO(X^1\Sigma^+)$
R_{NN-O}(Å)
R_{N-NO}(Å)
26
24
22
20
18
16
14
12
1.7
1.5
1.3
1.1
1.3
1.5
1.7

Figure 3.5

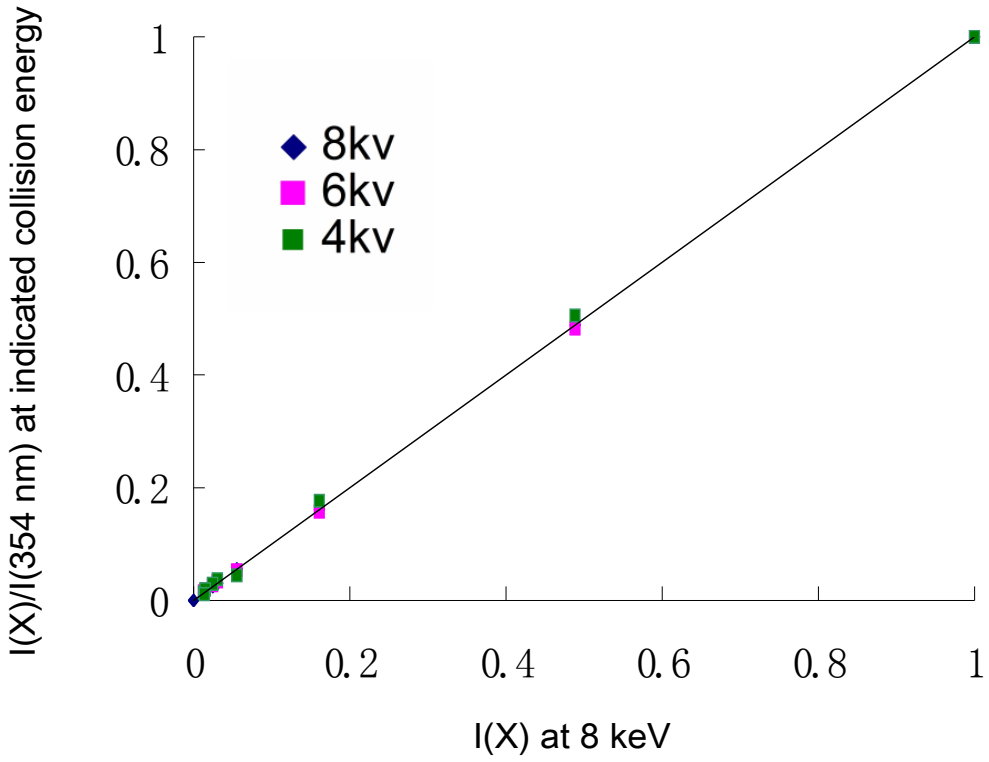
I(X)/I(354 nm) at indicated collision energy
1
0.8
0.6
0.4
0.2
0
8kv
6kv
4kv
0
0.2
0.4
0.6
0.8
1
I(X) at 8 keV

Figure 3.6

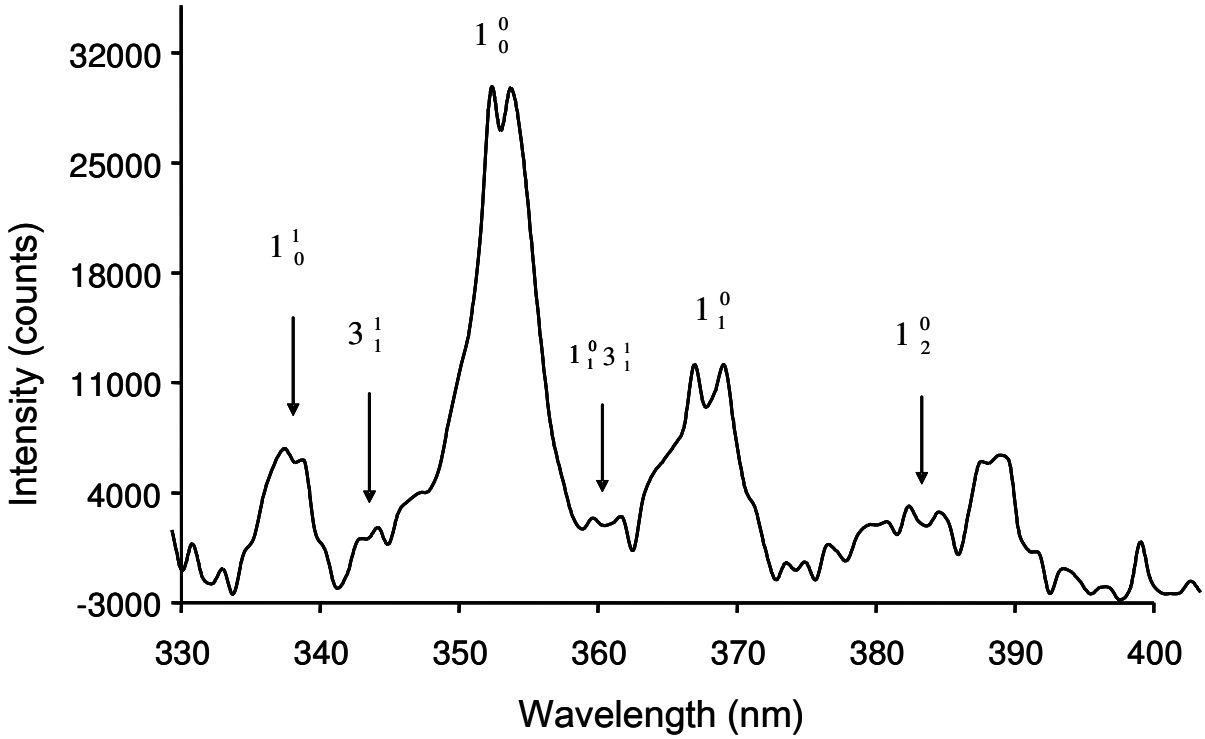
Intensity (counts)
32000
25000
18000
11000
4000
-3000
330
340
350
360
370
380
390
400
Wavelength (nm)
1^{0}_{0}
1^{1}_{0}
3^{1}_{1}
$1^{0}_{1}3^{1}_{1}$
1^{0}_{1}
1^{0}_{2}

Chapter 4

A comparison of the charge transfer and collisional activation processes in ionized CO_2/He collisions

4.1 Introduction

The fluorescence of $CO_2^{+\bullet}$ and its dissociation products had been observed to be the important components of the dayglow of Mars in 1968 [1,2]. The emission band systems of $CO_2^{+\bullet}$ arise from the transitions between the excited A $^2\Pi_u^+$ and B $^2\Sigma^+_u$ states to the ground

state X $^2\Pi_g$ [2,3]. Prominent transitions of the A $^2\Pi_u^+ \rightarrow$ X $^2\Pi_g$ system, ranging from 280 to 500 nm, are the symmetric (ν_1) vibrational progressions, while the unsymmetrical (ν_2 and ν_3) vibrational progressions do not make a great contribution [4,5]. The B $^2\Sigma^+_u \rightarrow$ X $^2\Pi_g$ band system, located at 288nm, displays a dominant $\Delta\nu = 0$ sequence. Higher lying electronic states of $CO_2^{+\bullet}$ are found to be efficiently predissociative [6-9]. For example, the C $^2\Sigma^+_g$ state of $CO_2^{+\bullet}$ has been determined by photoionization experiments to be able to fully predissociate into $O^{+\bullet}$ +CO and $CO^{+\bullet}$+O [10].

Various studies of ionization and dissociative excitation of CO_2 have been published, such as electron ionization [11-13], Penning ionization [14-16], photon impact [17,18] and charge transfer ionization [19-21]. In 1980, the photoelectron-photon coincidence experiments by Maier et al. [22] showed the existence of interelectronic state coupling between the A and B states of $CO_2^{+\bullet}$. The A and B state coupling can result in photon emission between 330 and 450 nm, changing the vibrational distribution of the A state.

A recent paper from our lab studied the collision induced emission of $CO_2^{+\bullet}$ formed by the keV (laboratory frame) ion-molecule collisional activation ($CO_2^{+\bullet}$/He) [23]. Results confirmed that the activation follows the curve-crossing mechanism [24-26]. The qualitative and quantitative description of curve crossing adiabatic energy transfer to produce electronic excitation has been described by Massey, Burshop, Gilbody and Nikitin [27-28]. During the $CO_2^{+\bullet}$/He collision process, when the projectile ion approaches the target, the electronic energy of the collision complex increases along the adiabatic curve of the ground state (at the expense of translational energy), until the ground state potential surface crosses with that of

an excited state. The strength of the non-adiabatic coupling of the two curves can be represented as the Massey parameter, ξ, in the Massey equation $\xi = a\Delta E / h\upsilon$ (ΔE is the smallest energy gap between two adiabatic states, 'a' is the width of the nonadiabatic interaction region and υ is the classical nuclear velocity). The curve-crossing then brings about a radiationless transition between the ground and electronic excited state of the collision complex. During separation of the collision complex, the projectile ion may return to its original energy surface or remain in an excited electronic state. In the latter case the electronic excitation can be removed by emission of a photon or converted to ro-vibrational excitation of the ground state by IVR (intramolecular vibrational relaxation).

As a comparison, the charge transfer reactions of $He^{+\bullet}$ with CO_2 were studied via the collision-induced emission (CIE) spectrum from the collision of $He^{+\bullet}$ with stationary CO_2 at laboratory frame collision energies of 4-8 keV. The photoemission spectrum with higher resolution was also obtained in the wavelength range of 280-500 nm, sufficient for the measurement of vibrational populations.

4.21 Experimental procedures

All experiments were performed on a modified VG ZAB mass spectrometer[29] with an added third field-free region (3FFR) as previously described [30-31]. $He^{+\bullet}$ ions were generated from He by 80-90 eV electron ionization in the ion source of the instrument. The ions were transmitted to the 3FFR where they collided with the target gas CO_2 in the cell at a

collision gas pressure that reduces the pre-cell ion flux by 10% (i.e. essentially single collision conditions) [29]. With 80-90 eV electrons, ionization of He could result in $He^{+\bullet}$ excited states being formed in the ion source. However, most of the radiative lifetimes of those states are under 100 ns [32]. When compared to the time required for the ions to reach the collision chamber, which ranges from 5 to 10 μs depending on the accelerating voltage, virtually all ions that are formed initially in excited states would have returned to the ground state by the time they collide with the target gas. To ensure that excited states of $He^{+\bullet}$ were not playing a significant role, He was ionized with <50 eV electrons. The resulting 8 keV collision-induced emission spectrum is indistinguishable from that obtained with >80 eV electron ionization (Table 4.2 and supporting information).

A spectrograph (Acton SpectraPro 275, 27.5cm focal length, 1200 g mm^{-1} holographic grating) and a thermoelectrically-cooled charge-coupled device (CCD) detector (Andor DV401-UV, front-illuminated with UV coating) have been installed above the collision cell for the detection of photon emissions resulting from ion-target collisions [33]. Emissions from the excited state species were directly observed with the CCD detector cooled to a temperature of -35 ºC. The time window of observation ranges from 14-19 ns for 8 keV to 4 keV $He^{+\bullet}$. The entrance slit of the spectrograph was set to 3.0 mm, providing a spectral resolution of 8.5 nm (measured at full width at half-height for atomic lines). Optical emissions were recorded from 190-1020 nm using the Andor MCD 2.63.1.8 program and were recorded in 14 separate segments, each being 50-70 nm wide. Two accumulations of 30 minutes were collected at 8 keV ion translational energy for each segment at full vertical binning reading mode. For other ion translational energies, the total acquisition time for each

of the separate segments ranged from 1 hour to 2 hours. Each segment was background subtracted and background spectra were collected prior to signal acquisition with exactly the same conditions, except without an ion beam. Spectral spikes resulting from cosmic rays were removed digitally by the program. Horizontal binning was performed manually in the ASCII file by combining data of every 20 pixel columns and the overlapping portion of the spectrum at the two ends of each window was averaged. A higher-resolution spectrum (280-450 nm) was obtained by reducing the entrance slit width to 1.0 mm, resulting in a spectral resolution of 3.0 nm, and the data acquisition time of each segment was increased to 4 hours.

4.2.2 Potential energy curves calculation of collision complex $CO_2^{+\bullet}$-He

Adiabatic potential curves for the ionized collision complex CO_2/He as a function of collision coordinate were calculated at the CISD/6-311+g(2df) level of theory using the Gaussian 98 suite of programs [34]. The collision trajectory in Cartesian coordinates is shown in Figure 4.1. Single-point energy calculations of ionized CO_2/He were performed as a function of α, from 0 to 3 Å in steps of 0.1 Å with a specific impact parameter β. (β value varies from 0.5 to 0.8 Å) The collision trajectory was chosen in this way so that the collision complex always possesses C_{2v} symmetry and the adiabatic curves in the C_{2v} point group will have different irreducible representations, allowing us to identify which state crossings are involved in the collision processes. Due to the relative ionisation energies of the two species, the curves relate specifically to a collision between ionized CO_2 and neutral He. The potential energy curves of the A $^2\Pi_u^+$ state and the ground state X $^2\Pi_g$ of CO_2^+-He contain

more than one individual orbital component; the A state consists of A_1 and B_1 components, the ground state consists A_2 and B_2 components, respectively.

4.3 Results and discussion

4.3.1 Emission spectrum from $He^{+\bullet}/CO_2$ collisions

The emission spectrum obtained from $He^{+\bullet}/CO_2$ collisions at 8 keV ion translational energy is shown in Figure 4.2. A summary of the peak and transition assignments is presented in Table 4.1. Emission signals observed in the lower wavelength region (290-440 nm) correspond to the A $^2\Pi_u^+ \rightarrow$ X $^2\Pi_g$ and B $^2\Sigma^+_u \rightarrow$ X $^2\Pi_g$ transitions of $CO_2^{+\bullet}$, emissions from the neutralized $He^{+\bullet}$ and emissions from C, $C^{+\cdot}$, and O dissociation fragments. The continuum at 500 nm is due to the $He^{+\bullet}$ ion beam striking the silica window [35,36]. Almost all of the species observed in the CIE spectrum must be from charge transfer reactions (including dissociative charge transfer) indicating that this is the dominant reaction during the $He^{+\bullet}/CO_2$ collision process.

The strongest emission band is from the $CO_2^{+\bullet}$ B→X system. The remainders of the molecular emissions at longer wavelengths are vibrational transitions in the $CO_2^{+\bullet}$ A→X system. The 0,0,0-7,0,0 appear to be the dominant vibrational levels populated. The relative peak intensity ratios for the molecular emission of $CO_2^{+\bullet}$ are shown in Table 4.2. Among the vibrational transition progressions of $CO_2^{+\bullet}$ A→X system, $\Delta\nu$ = +5, +4, +3, +2, +1, 0, -1, -2, $\Delta\nu$ = +2 (326nm) is the most prominent one. $I_{(B\rightarrow X)} / I_{(A\rightarrow X, \Delta\nu=+2)}$ = 250:100 (where I is the

intensity of the designated band). In our earlier study of the $CO_2^{+\bullet}$/He system [23], both A→X and B→X band emissions were also observed, however, the $\Delta\nu = +1$ (338nm) instead of $\Delta\nu = +2$ (326 nm) was the most intense progression in the A→X system. In addition, the intensity (relative to the A→X system) of the B→X band was lower than in the present experiment ($I_{(B\rightarrow X)} / I_{(A\rightarrow X, \Delta\nu=+1)}$ = 102:100, as compared to the present value of 250:100, Table 4.2). So, due to the exothermic nature of the collisional charge transfer, and the slightly shorter interaction time (factor of ~ 3), excitiation of neutral CO_2 to form $CO_2^{+\bullet}$ has more Franck-Condon character (similar to photoexcitation) than the excitation of $CO_2^{+\bullet}$ upon collision with neutral He. In the latter case, interelectronic coupling of the B and A states produces more IVR [22], reducing the population of the B state and producing a more evenly distributed vibrational excitation in the A state.

Figure 4.1 presents the adiabatic potential energy curves of the $CO_2^{+\bullet}$/He collision complex at β=0.6 Å using the CISD/6-311+g(2df) level of theory. Since the excited states of He are much higher than those of $CO_2^{+\bullet}$, the lowest excited states of the collision complex are the interaction of the ground state of He with excited states of $CO_2^{+\bullet}$. Figure 4.3 shows the calculated potential curves with 0.5, 0.7 and 0.8 Å as the β values. In all cases, the A_2 component of the X $^2\Pi_g$ state crosses with the A_1 component of the A $^2\Pi_u$ state and the $B^2\Sigma^+_u$ state crosses with A_2 component of the A $^2\Pi_u$ state, in agreement with the $CO_2^{+\bullet}$ A→X and B→X band emission observed in the $CO_2^{+\bullet}$/He experiment. Also, note that the potential curves of A and B states are crossing during the collision process, which could promote the A and B electronic state coupling, thus explaining the discrepancy between the $CO_2^{+\bullet}$/He and $He^{+\bullet}/CO_2$ spectra.

4.3.2 Vibrational distribution in the A state $CO_2^{+\bullet}$ ion

Figure 4.4 shows a higher resolution CIE spectrum of the $CO_2^{+\bullet}$ A $^2\Pi_u^+ \rightarrow$ X $^2\Pi_g$ system in the 280-440 nm region produced by 8 keV collisions. Stretching vibrational progressions $\Delta\nu$ = +5,+4,+3, +2, +1, 0, -1, -2, -3,-4 were observed. In addition, another vibrational progression marked by asterisks was seen. The assignment of this series is also included in Table 4.1. The vibrational distribution is known to be related to the emission intensities and Franck-Condon factor as described in the equation below [40]

$$I_{em}^{\nu'\nu''} = K \frac{N_{\nu'}}{(\lambda_{\nu',\nu''})^4} \overline{R}_e^{\,2} q_{\nu',\nu''} \qquad (1)$$

where $I_{em}^{\nu'\nu''}$ $q_{\nu',\nu''}$ $\lambda_{\nu',\nu''}$ are emission intensity, Franck-Condon factor and emission wavelength, respectively, for the ν'–ν'' band. $N_{\nu'}$ is the vibrational population of ν' level and $\overline{R}_e$ is the average electronic transition moment which is nearly constant within a sequence. Each peak in A $^2\Pi_u^+ \rightarrow$ X $^2\Pi_g$ transition is composed of several individual components corresponding to transitions between different vibrational states, for example the peak of $\Delta\nu = 0$ sequence contains contribution from transitions 0-0, 1-1, 2-2, 3-3 etc. Therefore, each peak in the A $^2\Pi_u^+ \rightarrow$ X $^2\Pi_g$ transition in Figure 4.4 can be fitted by combining those $(\nu_i,0,0) \rightarrow (\nu_j,0,0)$ transitions with the same $\Delta\nu$ values in A $^2\Pi_u^+ \rightarrow$ X $^2\Pi_g$ system, as shown below

$$H(\lambda) = K'\left(\frac{N_i}{(\lambda_{ij})^4} \cdot \frac{q_{ij}}{q_{tot}} G(\lambda) + \frac{N_{i+1}}{(\lambda_{i+1\,j+1})^4} \cdot \frac{q_{i+1\,j+1}}{q_{tot}} G(\lambda) + \frac{N_{i+2}}{(\lambda_{i+2\,j+2})^4} \cdot \frac{q_{i+2\,j+2}}{q_{tot}} G(\lambda) + \ldots\right) \quad (2)$$

where $H(\lambda)$ is the emission peak to be fitted, $G(\lambda)$ is Gaussian function, K' is a constant, λ_{ij} and q_{ij} are the emission wavelength and Franck-Condon factor between $(v_i,0,0)$ of the A state and $(v_j,0,0)$ of the B state, respectively.

Figure 4.5 shows the result of the fits for $He^{+\bullet}/CO_2$ spectrum. Also, the previously reported $CO_2^{+\bullet}$/He spectrum [23] was fitted using the same equation. The relative vibrational populations for states $(0,0,0)$ to $(7,0,0)$ are listed in Table 4.3 along with those produced by electron ionization and photoionization. The vibrational population obtained from $He^{+\bullet}/CO_2$ collisions is quite similar to that obtained from the photoelectron spectrum. The relative peak intensities of each sequence in A $^2\Pi_u^+ \rightarrow$ X $^2\Pi_g$ emission barely change in going from 4-8 keV. This again shows that when the velocity of $He^{+\bullet}$ is larger than 3.1×10^7 cm/s, the excitation of the A state in $CO_2^{+\bullet}$ is similar to that using photoexcitation, due to the short reaction time and high exothermicity of the charge transfer reaction that produces the excited A state. The vibrational population obtained derived from the previously reported $CO_2^{+\bullet}$/He collisions is different from $He^{+\bullet}/CO_2$ but similar to the result from electron ionization (Table 4.3). Compared with photoionization, $CO_2^{+\bullet}$/ He collisions show a more even distribution among levels i = 0-4, that are likely the result of the initial formation of higher dissociative states of $CO_2^{+\bullet}$ from curve-crossing excitation followed by intramolecular vibrational redistribution (IVR) before emission.

4.4 Conclusion

The emission spectra produced by $He^{+\bullet}$ impact on CO_2 at 4-8 keV ($He^{+\bullet}$ / CO_2) have been observed using a modified VG-ZAB mass spectrometer. The spectra consist almost exclusively of emissions from dissociative charge transfer products, confirming dissociative charge transfer reactions dominate the collisional activation process. The vibrational distribution of the resulting $CO_2^{+\bullet}$ A $^2\Pi_u^+$ state indicate that the excitation mechanism is similar to the photo-excitation. For the previously reported case of $CO_2^{+\bullet}$ impact on He ($CO_2^{+\bullet}$ /He), newly calculated adiabatic potential energy surfaces show the direct crossing of the $CO_2^{+\bullet}$ A $^2\Pi_u^+$ and B $^2\Sigma^+_u$ states. Differences in the vibrational populations of the A state in these two types of collisions is likely due to IVR following the formation of higher $CO_2^{+\bullet}$ states when it is the projectile ion.

.

REFERENCES

[1] S.S. Penner, A. Boni, J. Quant. Spectrosc. Radiat. Transfer 8 (1968) 847.

[2] A. Dalgarno, T.C. Degges, A.I. Stewart, Science 167 (1970) 1490.

[3] C.A. Barth, W.G. Fastie, C.W. Hord, J.B. Pearce, K.K. Kelly, A.I. Stewart, G.E. Thomas, G.P. Anderson, O.F. Raper, Science 165 (1969) 1004.

[4] G. Herzberg, Electronic Spectra of Polyatomic Molecules, Van Nostrand, Princeton,1967.

[5] D.L. Judge, G.S. Bloom, A.L. Morse, Can. J. Phys. 47 (1969) 489.

[6] J. H. D. Eland, Int. J. Mass Spectrom. Ion Phys. 9 (1972) 397.

[7] A.W. Potts, T.A. Williams, J. Electron Spectrosc. Relat. Phenom. 3 (1974) 3.

[8] A.P. Hitchcock, C.E. Brion, M.J. van der Wiel, Chem. Phys. 45 (1980) 461.

[9] T. Wyttenbach, D.D. Evard, J.P. Maier, J. Chem. Phys. 90 (1989) 4645.

[10] J.H.D. Eland, J. Berkowitz, J. Chem. Phys. 67 (1977) 2782.

[11] J.W. McConkey, D.J. Burns, J.M. Woolsey, J. Phys. B: At. Mol. Phys. 1 (1968) 71.

[12] H. Nishimura, J. Phys. Soc. Japan 24 (1968) 130.

[13] S. Tsurubuchi, T. Iwai, T. Horie, J. Phys. Soc. Japan 36 (1974) 537.

[14] T.S. Wauchop, H.P. Broida, J. Quant. Spectrosc. Radiat. Transfer 12 (1972) 371.

[15] G. Taieb, H.P. Broida, Chem. Phys. 21 (1977) 313.

[16] M. Endoh, M. Tsuji, Y. Nishimura, J. Chem. Phys. 77 (1982) 4027.

[17] L.C. Lee, D.L. Judge, J. Chem. Phys. 57 (1972) 4443.

[18] C.R. Brundle, D.W. Turner, J. Mass Spectrom Ion Phys. 2 (1969) 195.

[19] H. Bregman-Reisler, J.P. Doering, J. Chem. Phys, 62 (1975) 3109.

[20] M.J. Haugh, J.H. Birely, J. Chem. Phys. 60 (1974) 264.

[21] M. Tsuji, M. Endoh, T. Susuki, K. Mizukami, Y. Nishimura, J. Chem. Phys. 81 (1984) 3559.

[22] J. P. Maier, F. Thommen, Chem. Phys., 51 (1980) 319.

[23] C. Poon, P.M. Mayer, J. Am. Soc. Mass Spectrom. 19 (2008) 1551.

[24] P.M Mayer, C. Poon, Mass Spec. Rev. 28 (2009) 612.

[25] J. Durup, Recent Developments in Mass Spectrometry, University Park, Baltimore, 1970.

[26] S.A. McLuckey, J. Am. Soc. Mass Spectrom. 3 (1992) 599.

[27] H.S.W. Massey, E.H.S. Burshop, H.B. Gilbody, Electronic and Ionic Impact Phenomena, Clarendon, Oxford, 1974.

[28] E.E. Nikitin, Theory of Elementary Atomic and Molecular Processes in Gases, Clarendon, Oxford, 1974.

[29] J.L. Holmes, Org. Mass Spectrom. 20 (1985) 169.

[30] P.C. Burgers, J.L. Holmes, J.E. Szulejko, A.A. Mommers, J.K. Terlouw, Org. Mass Spectrom. 18 (1983) 254.

[31] J.L. Holmes, P.M. Mayer, A.A. Mommers, Int. J. Mass Spectrom. Ion Processes 135 (1994) 213.

[32] W.L. Wiese, M.W. Smith, B.M. Glennon, Atomic Transition Probabilities, National Bureau of Standards, Washington, 1966.

[33] C. Poon, P.M. Mayer, J. Phys. Chem. A 111 (2007) 777.

[34] M.J. Frisch, G.W. Trucks, H.B. Schlegel, G.E. Scuseria, M.A. Robb, J.R. Cheeseman, V.G. Zakrzewski, J.A. Montgomery, Jr., R.E. Stratmann, J.C. Burant, S. Dapprich, J.M. Millam, A.D. Daniels, K.N. Kudin, M.C. Strain, O. Farkas, J. Tomasi, V.Barone, M.Cossi, R. Cammi, B. Mennucci, C. Pomelli, C. Adamo, S. Clifford, J. Ochterski, G.

A. Petersson, P. Y. Ayala, Q. Cui, K. Morokuma, D. K. Malick, A. D. Rabuck, K. Raghavachari, J. B. Foresman, J. Cioslowski, J. V. Ortiz, B. B. Stefanov, G. Liu, A. Liashenko, P. Piskorz, I. Komaromi, R. Gomperts, R. L. Martin, D. J. Fox, T. Keith, M. A. Al-Laham, C. Y. Peng, A. Nanayakkara, C. Gonzalez, M. Challacombe, P. M. W. Gill, B. Johnson, W. Chen, M. W. Wong, J. L. Andres, C. Gonzalez, M. Head-Gordon, E. S. Replogle, and J. A. Pople, in, Gaussian, Inc., Pittsburgh PA, 1998.

[35] M. Kimura, T. Iwai, T. Horie, Electronic and Atomic Collisions, Institute of Physics, Belgrade, 1973, p. 674.

[36] C. B. Liu, in Ph.D. Dissertation, U. of California, Santa Barbara, 1969.

[37] P.J. Linstrom, W.G. Mallard, Eds., in NIST Standard Reference Database Number 69, National Institute of Standards and Technology, Gaithersburg MD, 20899, retrieved June 2, 2010,http://webbook.nist.gov.

[38] A. Crowe, J.W. McConkey, J. Phys. B 7 (1974) 349.

[39] J. Appell, J. Durup, F. Heitz, J. Advan. Mass Spectrom. 3 (1964) 457.

[40] G. Herzberg, Molecular Spectra and Molecular Structure. I. Spectra of Diatomic Molecules, Van Nostrand Reinhold, New York, 1950, p. 200.

[41] M. Bloch, D.W. Turner, Chem. Phys. Lett. 30 (1975) 344.

[42] J. P. Maier, F. Thommen, Chem. Phys. 51 (1980) 319.

[43] D. Gauyacq, M Horani, S. Leach, J. Rostas, Can. J. Phys. 53 (1975) 2040.

[44] D. Gauyacq, C. Larcher, J. Rostas, Can. J. Phys. 57 (1979) 1634.

[45] J. Liu, W. Chen, C.W. Hsu, M. Hochlaf, M. Evans, S. Stimson, C. Y. Ng, J. Chem. Phys. 112 (2000) 10767.

[46] J. Liu, M. Hochlaf , C.Y. Ng, J. Chem. Phys. 113 (2000) 7988.

[47] L.S. Wang, J.E. Reutt, Y.T. Lee, D.A. Shirley, J. Electron Spectrosc. Relat. Phenom. 47 (1988) 167.

[48] S. Bashkin, J.O. Stoner, Atomic Energy Levels and Grotrian Diagrams. Vol. 1, North Holland, New York, 1975.

[49] I. Tokue, H. Shimada, A. Masuda, Y. Ito, H. Kume, J. Chem. Phys. 93 (1990) 4812.

Table 4.1. Observed emissions in the collison of $He^{+\bullet}$ with neutral CO_2.

Transition[a]		τ (ns)	[c]λ_{obs} (nm)	[c] λ_{ref} (nm)	Ref.
$CO_2^{+\bullet}$	$B^2\Sigma^+_u \rightarrow X\ ^2\Pi_g$				41-43
	(n,0,0) → (n,0,0) ($\Delta\nu$ = 0)	~ 145	288	288	
	$A\ ^2\Pi_u^+ \rightarrow X\ ^2\Pi_g$				
	(n,0,0) → (n-5,0,0) ($\Delta\nu$ = 5)		295	294	
	(n,0,0) → (n-4,0,0) ($\Delta\nu$ = 4)		305	304	
	(n,0,0) → (n-3,0,0) ($\Delta\nu$ = 3)		315	315	
	(n,0,0) → (n-2,0,0) ($\Delta\nu$ = 2)	~ 120	327	326	
	(n,0,0) → (n-1,0,0) ($\Delta\nu$ = 1)		338	338	41-42
	(n,0,0) → (n,0,0) ($\Delta\nu$ = 0)		354	351	44-47
	(n,0,0) → (n+1,0,0) ($\Delta\nu$ = -1)		368	368	
	(n,0,0) → (n+2,0,0) ($\Delta\nu$ = -2)		388	386	
	where n = 0, 1, 2 …				
	[b](n,0,0) → (n-2,0,2) ($\Delta\nu$ = 2)*	—	362	361	
	(n,0,0) → (n-1,0,2) ($\Delta\nu$ = 1)*		377	361	
	(n,0,0) → (n,0,2) ($\Delta\nu$ = 0)*		396	392	45-47
	(n,0,0) → (n+1,0,2) ($\Delta\nu$ = -1)*		413	411	
	(n,0,0) → (n+2,0,2) ($\Delta\nu$ = -2)*		435	434	
	where n = 0, 1, 2 …				
O	$(3p)\ ^3P \rightarrow (3s)\ ^3S^0$	36	845	845	
	$(3p)\ ^5P \rightarrow (3s)\ ^5S^0$	29	779	777	
	$(3p')\ ^3D \rightarrow (3p)\ ^1D^0$	46	944	939-944	
	$(3d)\ ^5D^0 \rightarrow (3p)\ ^5P$	24	929	926	
	$(4d)\ ^5D^0 \rightarrow (3p)\ ^5P$	142	617	616	
	$(4d')\ ^3G^0 \rightarrow (3p')\ ^3F$	159	626	626	
C	$(3p)\ ^3P \rightarrow (3s)\ ^3P^0$	40	908	906-911	32, 48
$C^{+\cdot}$	$(3p)\ ^4D \rightarrow (3s)\ ^4P^0$	27	678	678-681	
	$(3d)\ ^2D \rightarrow (3p)\ ^2P^0$	22	727	723-724	
	$(3p)\ ^2P^0 \rightarrow (3s)\ ^2S$	21	658	658	
He	$(3d)\ ^3D \rightarrow (2p)\ ^3P0$	14	590	588	
	$(3d)\ ^1D \rightarrow (2p)\ ^1D^0$	16	669	668	
	$(3s)\ ^3S \rightarrow (2p)\ ^3P^0$	65	707	706	

[a]Transition written in notation (ν_1, ν_2, ν_3). For $CO_2^{+\bullet}$, ν_1 =symmetric stretch, ν_2 =bending mode and ν_3 = asymmetric stretch.

[b] The * refers to the sequence of (ν_1,0,0)→(ν_1,0,2) transitions.

[c]λ_{obs} and λ_{ref} refer to the wavelength values observed in this study and those reported in the literature, respectively.

Table 4.2. The relative peak intensity ratios for the molecular emission of $CO_2^{+\bullet}$

Method	[a] $I_{B\rightarrow X}$	[a] $I_{A\rightarrow X}$					
		294 [b]	304	315	326	338	351
[c] $CO_2^{+\bullet}$/ He	102	9	20	43	76	100	74
[d] $He^{+\bullet}$ /CO_2 (80-90 eV)	250	12	31	81	100	66	38
[e] $He^{+\bullet}$ /CO_2 (50 eV)	258	12	29	81	100	66	37

[a] The relative peak intensity of $CO_2^{+\bullet}$emission peak, the most intense peak in the $CO_2^{+\bullet}$ A $^2\Pi_u^+ \rightarrow$ X $^2\Pi_g$ system is taken as 100.

[b] The wavelength of each progression transition in $CO_2^{+\bullet}$ A $^2\Pi_u^+ \rightarrow$ X $^2\Pi_g$ band emission, in nm.

[c] 8 keV collisions between projectile $CO_2^{+\bullet}$ ions and stationary He target gas, from Ref. 23

[d] 8 keV collisions between projectile $He^{+\bullet}$ ions (produced by electron energy at 80-90 eV) and stationary CO_2 target gas, this study.

[e] 8 keV collisions between projectile $He^{+\bullet}$ ions (produced by electron energy at 50 eV) and stationary CO_2 target gas, this study. The spectrum is included in the supporting material.

Table 4.3. The relative vibrational populations for states (0,0,0) to (7,0,0) in the $CO_2^{+\bullet}$ A $^2\Pi_u^+$ state.

Method	Electron energy	Vibrational level (i,0,0)							
		0	1	2	3	4	5	6	7
$He^{+\bullet}/CO_2$ [a]		**3**	**12**	**28**	**21**	**16**	**12**	**6**	**2**
PES [b]		8	18	28	18	12	9	4	2
$CO_2^{+\bullet}$/ He [c]		13	19	19	18	18	5	5	2
EI [d]	30	12	26	21	19	13	6	2	1
	50	13	23	22	20	13	6	2	1
	100	13	23	21	19	14	6	2	1
	300	14	23	23	20	14	5	2	1

[a] 8 keV collisions between projectile $He^{+\bullet}$ ions and stationary CO_2 target gas, this study

[b] PES Photo-excitation spectrum, Ref. 18

[c] 8 keV collisions between projectile $CO_2^{+\bullet}$ ions and stationary He target gas, described in Ref. 23

[d] EI Electron ionization, Ref. 49

Figure Captions

Figure 4.1 Collision trajectory of $CO_2^{+\bullet}$/He collisions and adiabatic potential energy curves of the $CO_2^{+\bullet}$-He collision complex calculated with impact parameter $\beta = 0.6$ Å at the CISD/6-311+g(2df) level of theory.

Figure 4.2 Collision-induced emission spectra (190-1020 nm) of $He^{+\bullet}/CO_2$ collisions at 8 keV. Collision gas pressure corresponded to 90% ion beam transmission. The arrows with different shapes ↓↓↓ represent photoemission from C, He, O and $C^{+\cdot}$, respectively. Numbers refer to vibrational transitions listed in Table 4.1.

Figure 4.3 Adiabatic potential energy curves of the $CO_2^{+\bullet}$/He collision complex at various β values calculated at the CISD/6-311+g(2df) level of theory.

Figure 4.4 Collision-induced emission spectrum (330-400 nm) of 8 keV $He^{+\bullet}/CO_2$ collisions obtained with an entrance slit width of 1.0 mm (total data acquisition time per section: 8 hours). Numbers refer to vibrational transitions listed in Table 4.1.

Figure 4.5 Peaks in the $CO_2^{+\bullet}$ A $^2\Pi_u^+ \rightarrow$ X $^2\Pi_g$ emission obtained from $He^{+\bullet}/CO_2$ collisions fitted with equation (2). Individual vibrational transitions from (i,0,0) of the A $^2\Pi_u^+$ state to (j,0,0) of the X $^2\Pi_g$ state are represented as i-j.

Figure 4.1.

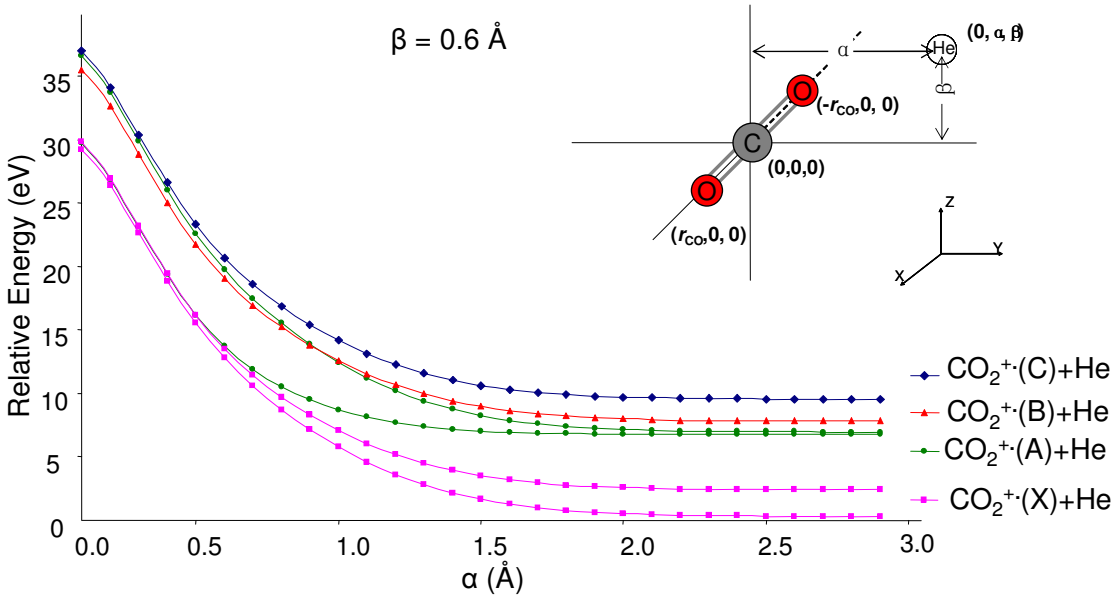
β = 0.6 Å
Relative Energy (eV)
α (Å)
0
5
10
15
20
25
30
35
0.0
0.5
1.0
1.5
2.0
2.5
3.0
α
β
He
(0, α, β)
O
(-rCO, 0, 0)
C
(0,0,0)
O
(rCO, 0, 0)
Z
Y
X
CO2+·(C)+He
CO2+·(B)+He
CO2+·(A)+He
CO2+·(X)+He

Figure 4.2.

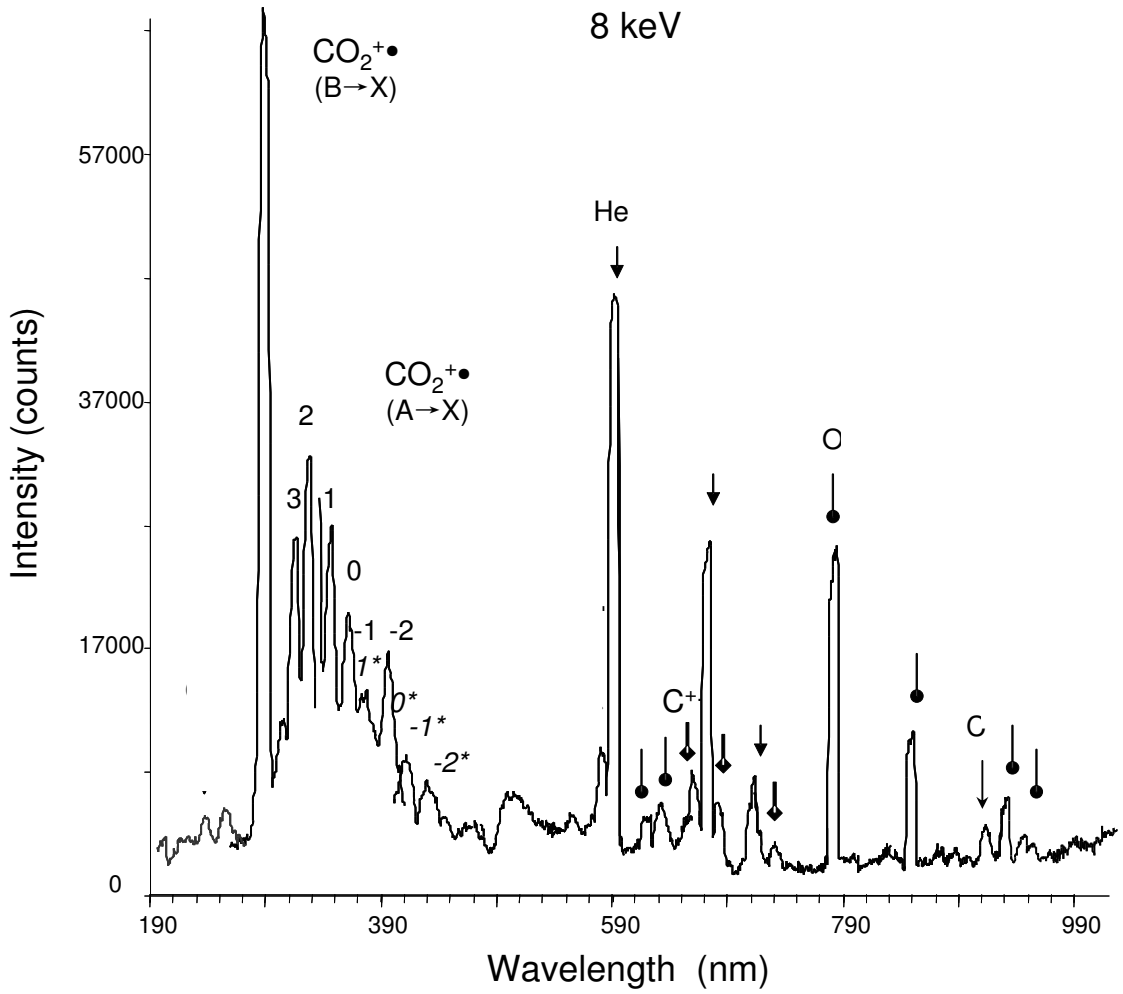
8 keV
$CO_2^{+\bullet}$ (B→X)
$CO_2^{+\bullet}$ (A→X)
He
C+
O
C
2
3
1
0
-1
-2
1*
0*
-1*
-2*
Intensity (counts)
57000
37000
17000
0
190
390
590
790
990
Wavelength (nm)

Figure 4.3.

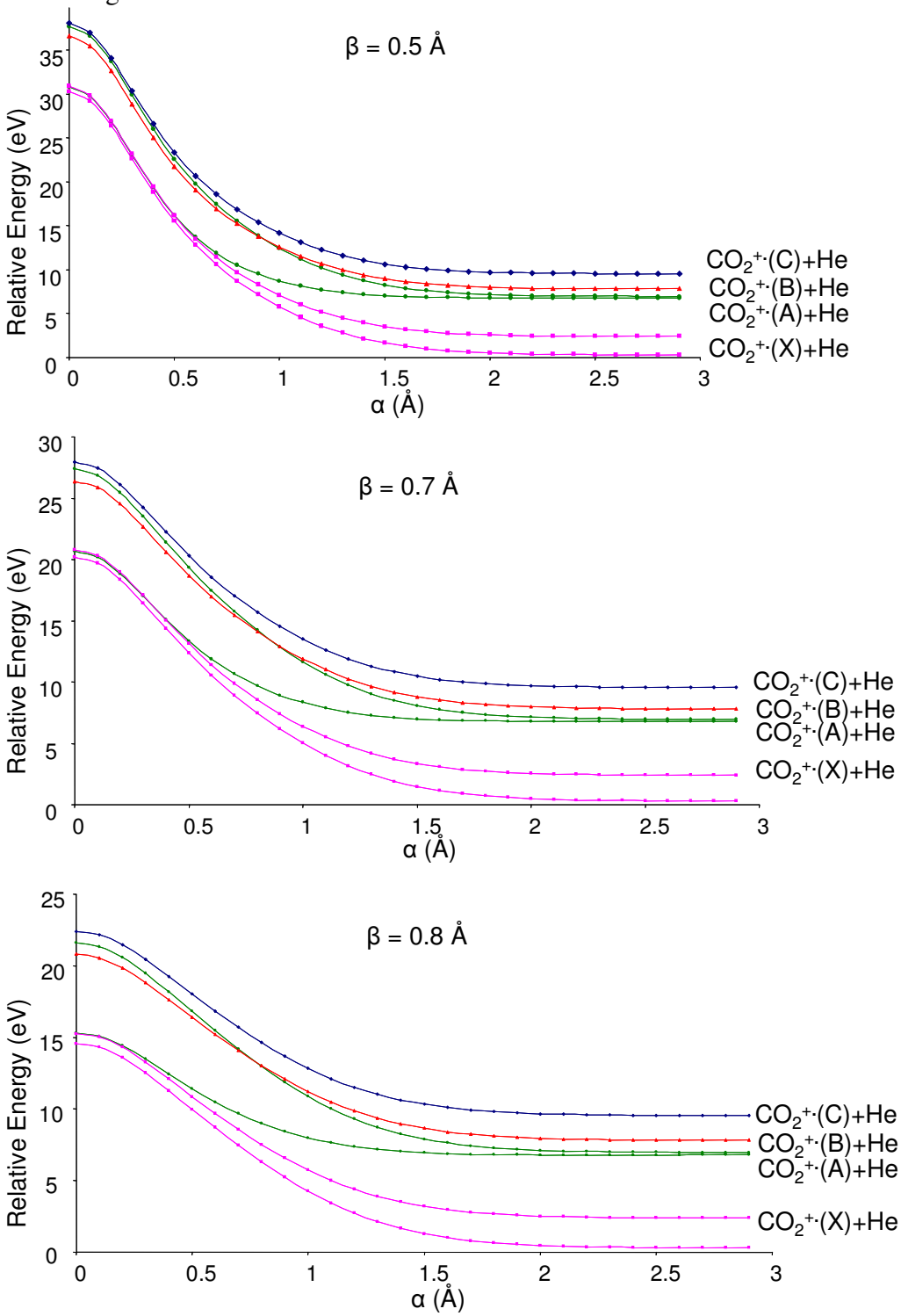
β = 0.5 Å
Relative Energy (eV)
α (Å)
$CO_2^{+\cdot}$(C)+He
$CO_2^{+\cdot}$(B)+He
$CO_2^{+\cdot}$(A)+He
$CO_2^{+\cdot}$(X)+He
β = 0.7 Å
Relative Energy (eV)
α (Å)
$CO_2^{+\cdot}$(C)+He
$CO_2^{+\cdot}$(B)+He
$CO_2^{+\cdot}$(A)+He
$CO_2^{+\cdot}$(X)+He
β = 0.8 Å
Relative Energy (eV)
α (Å)
$CO_2^{+\cdot}$(C)+He
$CO_2^{+\cdot}$(B)+He
$CO_2^{+\cdot}$(A)+He
$CO_2^{+\cdot}$(X)+He

Figure 4.4

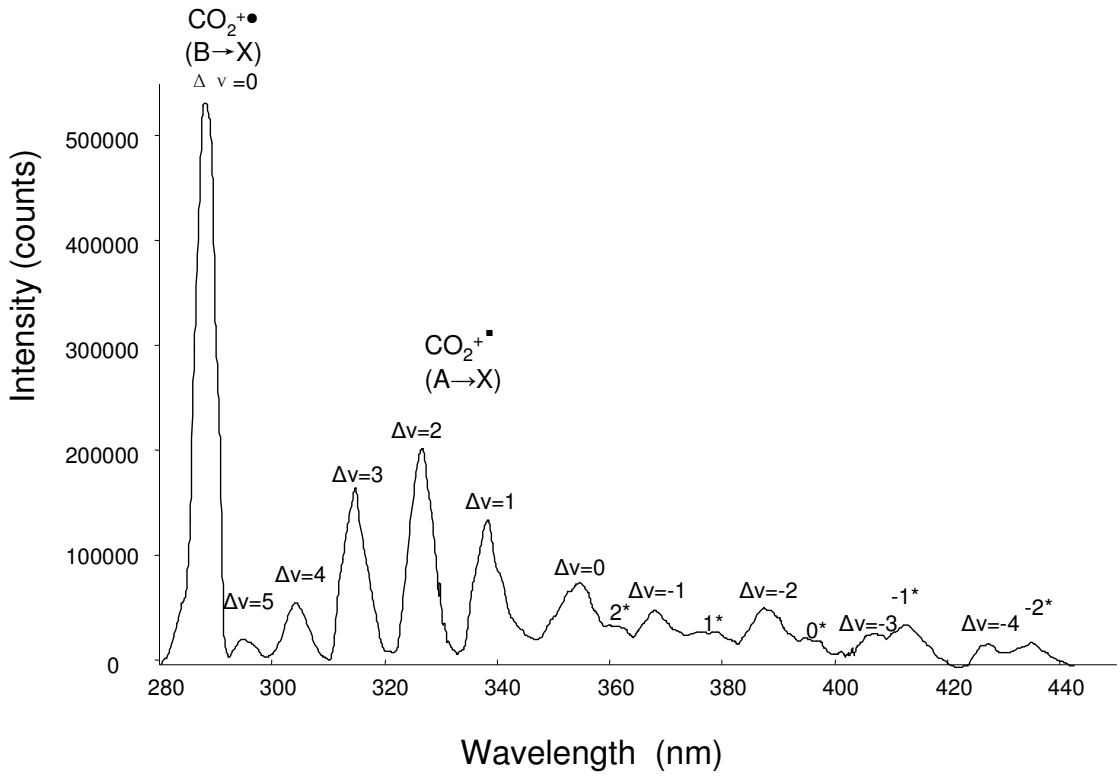
$CO_2^{+\bullet}$
(B→X)
Δ ν =0
$CO_2^{+\blacksquare}$
(A→X)
Δv=5
Δv=4
Δv=3
Δv=2
Δv=1
Δv=0
Δv=-1
Δv=-2
Δv=-3
Δv=-4
2*
1*
0*
-1*
-2*
Intensity (counts)
0
100000
200000
300000
400000
500000
280
300
320
340
360
380
400
420
440
Wavelength (nm)

Figure 4.5

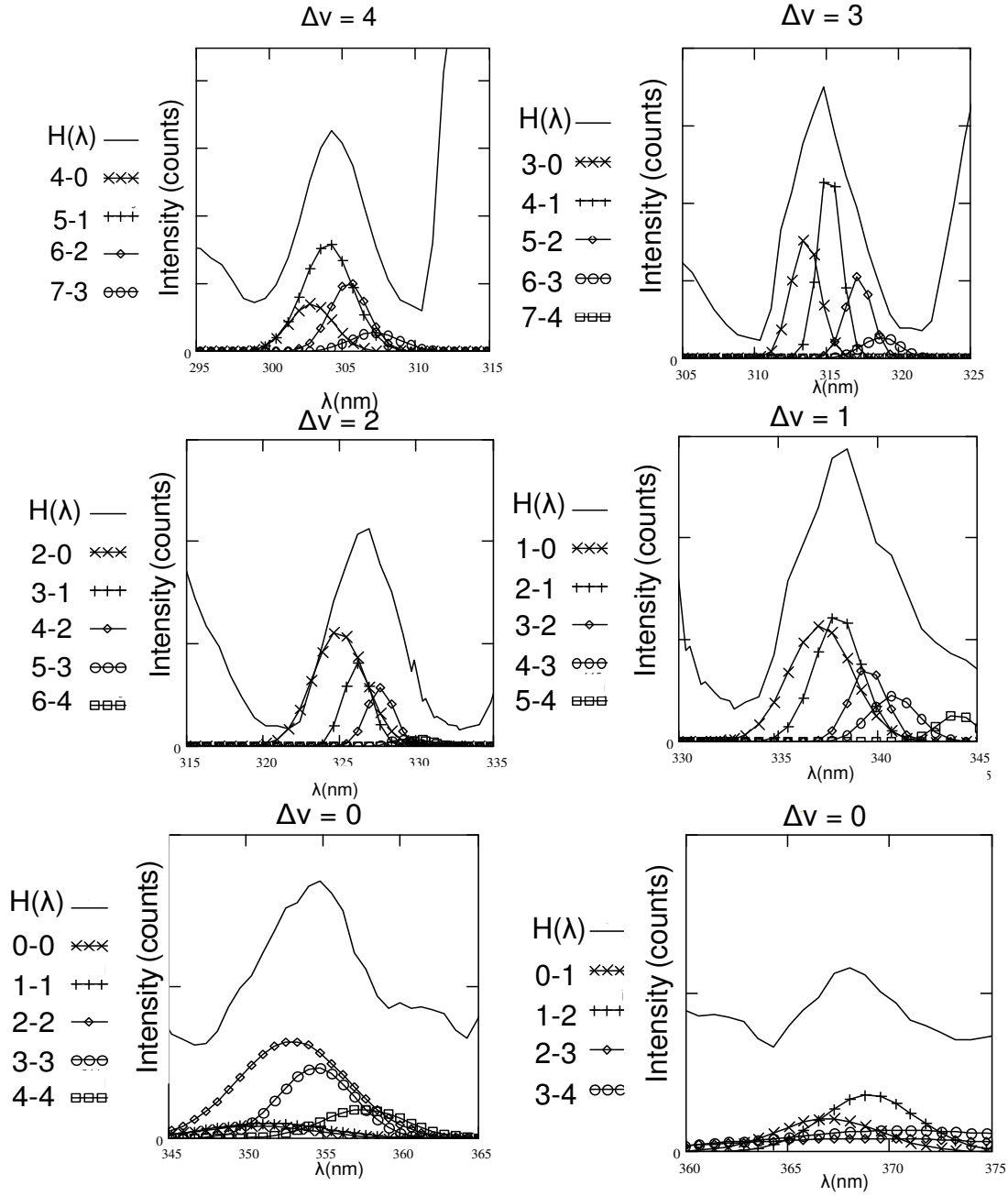
Δv = 4
H(λ)
4-0
5-1
6-2
7-3
Intensity (counts)
λ(nm)
Δv = 3
H(λ)
3-0
4-1
5-2
6-3
7-4
Intensity (counts)
λ(nm)
Δv = 2
H(λ)
2-0
3-1
4-2
5-3
6-4
Intensity (counts)
λ(nm)
Δv = 1
H(λ)
1-0
2-1
3-2
4-3
5-4
Intensity (counts)
λ(nm)
Δv = 0
H(λ)
0-0
1-1
2-2
3-3
4-4
Intensity (counts)
λ(nm)
Δv = 0
H(λ)
0-1
1-2
2-3
3-4
Intensity (counts)
λ(nm)

Chapter 5

Do the O_2 Shumann-Runge bands participate in keV collision-induced dissociation experiments?

5.1 Introduction

In mass spectrometry, dissociation of the ions may either occur spontaneously (metastable ion) or can result from intentionally supplied additional activation. Typically the activation is from collisions with neutral target gases, a process called collision-induced dissociation (CID). In a magnetic sector mass spectrometer, CID mass spectra are obtained

by mass selected ions colliding ions having keV lab frame energies with a stationary target gas. During the keV ion-target collision, part of the translational energy of the projectile ion can be converted into its internal energy and the internal energy of the ion is assumed to be redistributed statistically among the internal degrees of freedom, in the form of vibrational energy in the ground state, prior to dissociation [1, 2]. With this assumption, the produced CID mass spectra, resulting from the competition of different dissociation pathways, are independent of how the internal energy got into the ion in the first step.

To obtain CID mass spectra, various target gases can be used, such as N_2, Ar and He. According to empirical observations, the CID mass spectra using different target gases are quite similar [3]. However, O_2 behaves differently from most of the target gases in that it can particularly favor some specific fragmentation reactions. This nonergodic behavior of O_2-enhanced dissociation then arouses interests of several groups. Flammang et al. reported a series of O_2 enhanced dissociations in CID mass spectra compared with other common target gases such as N_2 and Ar [4-8]. Holmes et al. [9,10] did a systematic study of the O_2 enhanced dissociations: the $CH_3^{\cdot}$ loss from CH_3CH^+X (X=OH, NH_2, SH, CH_3); $CH_3^{\cdot}$ and $Cl^{\cdot}$ loss from $CH_3C^+(Cl)CH_3$; $C_2H_5^{\cdot}$ loss from $CH_3CH_2CH^+X$ (X=OH and NH_2); $H^{\cdot}$ loss from $^+CH_2OH$ and $^+CH_2NH_2$; O loss from 1,2-, 1,3- and 1,4-$C_6H_4(NO_2)_2^+$, etc. They found that these dissociation reactions share some common features in that they are all high-energy simple bond cleavage reactions. Moreover, their minimum energy requirements all fall in a relatively narrow energy range (450-565 kJ/mol). Some examples are shown in Figure 5.1. In the $^+CH_2OH$ CID mass spectrum, the peak with m/z 30 (fragment ion from $H^{\cdot}$ loss of $^+CH_2OH$) is more intense using O_2 as the target gas as compared to He, indicating that $H^{\cdot}$ loss from $^+CH_2OH$ is an O_2-enhanced dissociation. The $^+CH_2NH_2$ CID mass spectrum shows the

same pattern. The reaction leading to O loss from Nitromethane cation, $CH_3NO_2^{+\cdot}$ (producing m/z 45), thermochemically does not fall in the above energy window (229 kJ/mol), however enhancement is still observed. Note that the fragment ion peak exhibits significant broadening due to kinetic energy release during the dissociation, an indication that this channel involves a large reverse-energy barrier. This means though the reaction energy, ΔH, is 229 kJ/mol, the real energy requirement for this fragmentation, Ea, could still fall in the 450-565 kJ/mol energy range. This again is in agreement with the O_2-enhanced dissociation pattern. To rationalize these observations, the specific energy range of the dissociations was correlated to a property of the O_2 target itself. It has been reported [16] that the B $^3\Sigma_u^+$state of O_2 has a long lifetime in the range of milliseconds, and also its potential energy relative to the X $^3\Sigma_g^-$ ground state is from 598 to 682 kJ/mol (the later being the dissociation limit of O_2 to O(^{3}P) to O(^{1}D), shown in Figure 5.2), which is close to the O_2-enhancement dissociation energy window. Accordingly, it was proposed [10] that O_2 was excited from the ground X $^3\Sigma_g^-$ state to the B $^3\Sigma_u^+$ state (belonging to B $^3\Sigma_u^+$— X $^3\Sigma_g^-$ Shumann-Runge system) and that this B state of O_2 resonantly transfers this energy quanta back to the projectile ion in the collision complex, allowing the ion to undergo dissociations whose activation energy lies within that range.

Although the hypothesis explained the experimental results very well, there has been no concrete experimental evidence for the formation of the O_2 B state during the collision. It is known that when the excited states of a species are produced in the collision process, some of them will transit to lower states giving out characteristic photon emissions with specific wavelengths, (collision-induced emission, CIE). In this study, the CIE spectra were obtained

from different ion-O_2 collisions to probe the produced excited electronic states, especially the O_2 B $^3\Sigma_u^+ \rightarrow$ X $^3\Sigma_g^-$ SR emission band (the only observed emission involved with the B $^3\Sigma_u^+$ state [16]).

5.2 Experimental procedures

All experiments were performed on a modified VG ZAB mass spectrometer. The original, double-focusing mass spectrometer [11-13] with an added third field-free region (3FFR) as previously described [14, 15]. Ions were generated 80-90 eV electron ionization in the ion source of the instrument. The ions were transmitted to the 3FFR where they collided with the target gas in the collision cell at a collision gas pressure that reduces the pre-cell ion flux by 10% or 40% as needed.

A spectrograph (Acton SpectraPro 275, 27.5 focal length, 1200 g mm^{-1} holographic grating) (Acton Research Corp, Acton, Mass, USA) and a thermoelectrically-cooled charge-coupled device (CCD) detector (Andor DV401-UV, front-illuminated with UV coating, Andor Technology, Belfast, Northern Ireland) have been installed above the collision cell for the detection of photon emissions resulting from ion-target collisions [15]. Emissions from the excited state species were directly observed with the CCD detector cooled to a temperature of -35 ºC. The entrance slit of the spectrograph was set to 3.0 mm, providing a spectral resolution of 8.5 nm (measured at full width at half-height for atomic lines). Optical emissions were recorded from 190-1020 nm using the Andor MCD 2.63.1.8 program and were recorded in 14 separate segments, each being 50-70 nm wide. Two accumulations,

ranging from 1 hour to 4 hours, were collected at 8 keV ion translational energy for each segment at full vertical binning reading mode. Each segment was background subtracted and background spectra were collected prior to signal acquisition with exactly the same conditions except without an ion beam. Spectral spikes resulting from cosmic rays were removed digitally by the program. Horizontal binning was performed manually in the ASCII file by combining data of every 20 pixel columns and the overlapping portion of the spectrum at the two ends of each window was averaged.

Higher-resolution spectra were obtained by reducing the entrance slit width to 1.0 or 0.5 mm, resulting in a spectral resolution of 3.0 and 2.4 nm, and the data acquisition time of each segment was increased to 8 and 10 hrs.

During the whole accumulation, the ion flux intensity was monitored and adjusted to remain stable, and each segment is normalized according to the flux intensity of the ion beam.

5.3 Results and discussion

The Shumann-Runge (SR) system ($B\ ^3\Sigma_u^+ \rightarrow X\ ^3\Sigma_g^-$) is the most extensively studied system of O_2, with more than a hundred lines of this system being identified. The emission bands range from 207-535 nm, they are red-degraded and show no prominent band heads. Most other O_2 transitions are considerably weaker than the $B\ ^3\Sigma_u^+ \rightarrow X\ ^3\Sigma_g^-$ system, being forbidden by electric dipole selection rules.

5.3.1 CIE spectra of $CH_3NO_2^{+\cdot}/O_2$ and $CH_3NO_2^{+\cdot}$/He

The $CH_3NO_2^{+\cdot}$-target system has been studied since $CH_3NO_2^{+\cdot}$ ions can undergo an O_2-enhanced dissociation as mentioned in the introduction. In the experiment, $CH_3NO_2^{+\cdot}$ ion beams of same intensity were prepared and target gas were supplied to get 10% beam reduction (i.e. essentially single collision conditions [11]). The resulting CIE spectra were obtained after two hours signal accumulation for each section. Figure 5.3a shows the CIE spectra obtained from $CH_3NO_2^{+\cdot}/O_2$ and $CH_3NO_2^{+\cdot}$/He in the range of 190-570 nm, respectively. The $CH_3NO_2^{+\cdot}/O_2$ CIE spectra exhibit 3 narrow atomic emission peaks of C (3s $^1P^0 \rightarrow$ 1p ^1D), $H^{\cdot}_{\beta}$ (n=4→n=2) and $H^{\cdot}_{\lambda}$ (n=5→n=2) [17] as well as a broad emission band ranging from 190-310 nm, falling right in the range of the SR band. In contrast, the CIE spectrum of $CH_3NO_2^{+\cdot}$/He collisions exhibits no obvious emissions in this spectral range. Although the CIE spectrum of $CH_3NO_2^{+\cdot}/O_2$ indicates that a large amount of excited C and $H^{\cdot}$ have been produced during the collision, the ion fragment at m/z 49 (corresponding to loss of C) is not shown in the O_2 CID mass spectrum. The m/z 60 (loss of $H^{\cdot}$) peak is of similar intensity in both the He and O_2 CID mass spectra. Mclafferty et al. in 1987 [18] reported that the efficiency of the CID process was related to the ionization potential of the target gas and the Cooks group [19] showed that CID efficiency is greater for He targets because losses due to scattering and neutralization are reduced. Accordingly, the significant amount of excited C and $H^{\cdot}$, as shown in the CIE spectrum of $CH_3NO_2^{+\cdot}/O_2$ only, could be produced from dissociative charge transfer rather than CID.

To enhance the signal-to-noise ratio, target gas pressures were increased to produce 40% beam reduction. The resulting CIE spectra are shown in Figure 5.3b. In the CIE

spectrum of $CH_3NO_2^{+\cdot}/O_2$, the peak appeared at 314 nm was identified as atomic emission of $O^{+\cdot}$ ($4s\ ^4P^0 \rightarrow 3p\ ^4D^0$) [17], again confirming the charge transfer reactions existed during ion-O_2 collisions. Although the strength of the broad peak increased, it was still too weak to be identified. The CIE spectrum of $CH_3NO_2^{+\cdot}$/He shows no obvious emissions, indicating that the unidentified broad peak could come from the target O_2.

5.3.2 CIE spectra of $N_2^{+\cdot}/O_2$ and $N_2^{+\cdot}$/He

The simpler $N_2^{+\cdot}$/target gas system has also been studied. Figure 5.4 shows the CIE spectra obtained from $N_2^{+\cdot}/O_2$ and $N_2^{+\cdot}$/He collisions in the range of 190-570 nm. Both spectra show molecular emission from $N_2^{+\cdot}$ and N_2 [20-22]. The broad feature in this region is now more intense, but again appears only in the $N_2^{+\cdot}/O_2$ CIE spectrum, while $N_2^{+\cdot}$/He collisions give only a helium atomic emission. Figure 5.5a shows a higher resolution CIE spectrum for which the slits were narrowed from 3mm to 1mm and the accumulation time was increased from 2 hrs to 8 hrs. The unknown broad peak showed obvious vibrational structure and can now be indentified. The best match to the experimental data was found not to be the O_2 SR bands but rather the $A\ ^2\Pi_u \rightarrow X\ ^2\Pi_g\ O_2^{+\cdot}$ ion emission, which falls in the same energy window (Figure 5.2). The $O_2^{+\cdot}$ A→X emissions have obvious band heads and they are red-degraded and double-headed. The wavelengths of the $O_2^{+\cdot}$ A→X bands range from 194 to 653 nm, heavily overlapped with the SR band making emission identification difficult. The vertical lines in Figure 5.5a show the $O_2^{+\cdot}$ A→X emission bands reported in the literature [16] and agreement with the experimental data is excellent. However, the characteristic double head of the bands was not observed, due to low resolution. Fig 5.5b shows the CIE spectrum with the slit width reduced to 0.5 mm. The spectrum shows that

though the peak intensity becomes weaker we now observe the characteristic splitting of the A→X $O_2^{+\cdot}$ emission bands, confirming the existence of a significant amount of $O_2^{+\cdot}$ from charge transfer reactions. A full list of experimentally observed band heads and the reported $O_2^{+\cdot}$ A→X emission bands is available as supporting information.

5.3.3 CIE spectra of CH_3^+/O_2

Based on the above observation of the O_2 excited states produced, it is proposed that there are two possibilities: one is that there is no SR band formed in the collision; the other is the A→X $O_2^{+\cdot}$ emission produced from the charge transfer reaction between $N_2^{+\cdot}$ and O_2 is so intense that it masks the SR emission. To exclude the latter case, CH_3^+ was chosen as a projectile ion (ionization energy = 9.84 eV, compared to 12.07 eV for O_2) [23], so that the charge transfer reaction producing $O_2^{+\cdot}$ ion is not thermochemically favored. Figure 5.6 shows the CIE spectrum of CH_3^+/O_2 collisions compared to the $N_2^{+\cdot}/O_2$ system. The $N_2^{+\cdot}$ and N_2 emissions were not observed, of course, and two atomic emissions $C^{\cdot}$ (3s $^1P^0$→ 1p ^1D) and $O^{+\cdot}$ (4d ^4P→3p $^4S^0$) were found. The band emission is also present and compared with $N_2^{+\cdot}/O_2$ it is of lower intensity and shows no well resolved sequences. The accumulation time was increased from 2 hrs to 10 hrs, and the resulting spectrum obtained is shown in Figure 5.6b. The vertical lines show the wavelength of $O_2^{+\cdot}$ A→X emission. The band emission agrees with A→X $O_2^{+\cdot}$ emissions. When compared with the literature SR bands, shown in Figure 5.7, there are several peaks, marked by arrows, that don't agree with SR band values.

Above all, there is no strong evidence for the formation of a significant amount of the B state of O_2. However, the A→X $O_2^{+\cdot}$ emission bands and dissociative charge transfer

products emissions were consistently observed, even when charge transfer is thermochemically unfavorable, indicating that a considerable amount of the A state of $O_2^{+\cdot}$ can be generated during ion-O_2 collisions. Combining this with the fact that the energy difference between the A and X $O_2^{+\cdot}$ states is close to that between the B and X O_2 states [16], a second potential mechanism can be put forward to rationalize the O_2-enhancement effect: during ion-O_2 collisions, electron transfer in the collision complex forms a significant amount of $O_2^{+\cdot}$ A state. During the separation of the collision complex, some of the $O_2^{+\cdot}$ ions remain in their A state (collisional charge transfer) and emit, while others back-charge transfer to the projectile re-forming O_2 in its ground state, leaving the A→X energy quanta in the projectile ion, allowing it to undergo O_2-enhanced dissociation.

5.4 Conclusions

Strong $O_2^{+\cdot}$ A→X emission was observed in N_2^+/ O_2 CIE experiments, due to the charge transfer reaction between N_2^+ and O_2. This emission band is also observed CH_3^+/O_2 collisions, even though charge transfer is thermochemically unfavorable. It is postulated that the source of the observed O_2-enhancement for certain dissociation channels in O_2 CID experiments could result not from the participation of the O_2 Shumann-Runge bands (as previously hypothesized) but rather from the participation of this charge-transfer band.

REFERENCES

1. Mcluckey, S. A. Principles of Collisional Activation in Analytical Mass Spectrometry. *J. Am. Soc. Mass Spectrom*. **1992**, *3*, 599–614.
2. Mayer, P. M.; Poon, C. The Mechanisms of Collision Activation of Ions in Mass Spectrometry. *Mass Spetrom. Rev.* **2009**, *28*(3), 608-639.
3. Holmes, J. L.; Aubry, C.; Mayer, P. M. *Assignning structures to ions in mass spectrometry*; CRC Press: Boca Raton, 2007;
4. Flammang, R.; Gallez, L.; VanHaverbeke, Y.; Wong, M. W.; Wentrup C. An Unexpected Effect of the Nature of the Collision Gas in Collisional Activation Mass Spectrometry. *Rapid Commun. Mass Spectrom.* **1996**, *10*(2), 232-234.
5. Gerbaux, P.; Barbieux-Flammang, M.; VanHaverbeke, Y.; Flammang, R. Characterization of Ionized hetero- cyclic Carbenes by Ion-molecule Reactions. *Rapid Commun. Mass Spectrom.* **1999**, *13*(17), 1707-1711.
6. Flammang R.; Gerbaux P.; Wong M. W. Identification of Singlet and Triplet CNOS+ Cations in the Gas Phase. *Chem. Phys. Lett.* **1999**, *300*(1), 183-188.
7. Flammang, R.; Henrotte, V.; Gerbaux, P.; Nguyen, M. T. Collisional Interaction of Ionized Pyridine N-oxides with Various Targets in a New Hybrid Mass Spectrometer. *Eur. Mass Spectrom.* **2000**, *6*(1), 3-9.
8. Gerbaux, P.; Sciamanna, V.; Flammang R.; Nguyen, M. High-energy collisional activation of the molecular ions of thiophene-2-one with different target gases. *J. Mass. Spectrom.* **2001**, *36*(1), 97-101.
9. Aubry, C.; Holmes, J. L. A Butyl Cations and their Gas-Phase Dissociation Chemistry: Uniting Experiments with Theory *J. Phys. Chem.* **1998**, *102*(32), 6441-6447.

10. Aubry, C.; Holmes, J. L. The Behavior of Oxygen as a Collision-induced Dissociation Target Gas. *J Am. Soc. Mass Spectrom.* **2000**, *12*(1), 23-29.

11. Holmes, J. L. Assigning structures to ions in the gas phase. *Org. Mass Spectrom*. **1985**, *20*(3), 169-183.

12. Burgers, P. C.; Holmes, J. L.; Szulejko, J. E.; Mommers, A. A. and Terlouw, J. K. The Gas Phase Ion Chemistry of the Acetyl Cation and Isomeric $[C_2H_3O]^+$ Ions. On the Structure of the $[C_2H_3O]^+$ Daughter Ions Generated from the Enol of Acetone Radical Cation.Organic Mass Spectrometry, *Org. Mass Spectrom*. **1983**, *18*(6), 254-262.

13. Holmes, J. L.; Mommers, A. A.; Terlouw, J. K. and Hop, C. E. C. A., The Mass Spectrometry of Neutral Species produced from Mass-selected Ions by Collision and by Charge Exchange. Experiments with tandem collision gas cells. *Int. J. Mass Spectrom. Ion Processes*. **1986**, *68*(3), 249-64.

14. Holmes, J. L.; Mayer, P. M.; Mommers, A. A. Photon Emissions from $N_2^{\cdot+}$ Ion Beam-target gas Collisions in a Modified Commercial Sector Mass Spectrometer. *Int. J. Mass Spectrom. Ion Process*. **1994**, *135*(2-3), 213-28.

15. Poon, C.; Mayer, P. M. Experimental Evidence for the Curve Crossing Mechanism for Collisional Excitation in keV N_2^{+}bul./He Collisions by Emission Spectroscopy. *J. Phys. Chem.* A. **2007**, *111*(5), 777-782.

16. Krupenie, Paul H. Spectrum of Molecular Oxygen. *J. Phys. Chem. Ref. Data*. **1972,** *1*(2), 423-534.

17. Bashkin, S.; Stoner, J. O., Jr. *Atomic energy levels and Grotnan diagrams.* North Holland Press: New York, 1975;

18. Kim, M. S; McLafferty, F. W. Collisional Activation and Metastable Ion Characteristics. 59. Efficiency of Collisional Activation of Gaseous Organic ions. *J. Am. Chem. Soc.* **1978**, 100 (11) 3279-3282.

19. Laramee, J. A.; Cameron, D.; Cooks, R. G. Collision-induced Dissociation Mass spectrometry: Target Gas Effects upon Scattering and Charge Exchange. *J. Am. Chem. Soc.* **1981**, *103*(1), 12-17.

20. Bennett, R. G.; Dalby, F. W. Experimental determination of the oscillator strength of the first negative bands of $N_2^{+\cdot}$. *J. Chem. Phys.* **1959**, *31*, 434-41.

21. Hesser, J. E.; Dressler, K. J. Radiative Lifetimes of Ultraviolet Molecular Transitions. *Chem. Phys.* **1966**, *45*(8), 3149-3150.

22. Lofthus, A.; Krupenie, P. H. The Spectrum of Molecular Nitrogen. *J. Phys. Chem. Ref. Data*. **1977**, *6*(1), 113-307.

23. Linstrom, P. J.; Mallard, W. G Eds., in NIST Standard Reference Database Number 69, National Institute of Standards and Technology, Gaithersburg MD, 20899, retrieved June 2, 2010,http://webbook.nist.gov

Figure Captions

Figure 5.1. Partial He and O_2 CID mass spectra of (a) source $^{+}CH_2OH$ (b) source $^{+}CH_2NH_2$ (c) $CH_3NO_2^{+\cdot}$ by Holmes et al. (Ref. 9). (Reprinted from J Am. Soc. Mass Spectrom. 2000, 12(1), Aubry, C.; Holmes, J. L The Behavior of Oxygen as a Collision-induced Dissociation Target Gas p23-29 with permission from Elsevier)

Figure 5.2. Potential energy diagram of O_2 and $O_2^{+\cdot}$ by Krupenie (Ref.16).

Figure 5.3. a) CIE spectra of $CH_3NO_2^{+\cdot}/O_2$ versus $CH_3NO_2^{+\cdot}$/He, 10% beam reduction; slit width 3mm; accumulation time 1hr. b) CIE spectra of $CH_3NO_2^{+\cdot}/O_2$; 40% beam reduction; slit width 3mm; accumulation time 2hrs.

Figure 5.4. CIE spectrum of $N_2^{+\cdot}/O_2$ versus $N_2^{+\cdot}$/He, 40% beam reduction; slit width 3 mm, accumulation time 2hrs. The bands appeared in the wavelength range larger than 290 nm, marked by a circle, were identified as the emissions from $N_2^{+\cdot}$ and N_2.

Figure 5.5. a) CIE spectrum of $N_2^{+\cdot}/O_2$, 40% beam reduction; accumulation time 8hrs; slit width 1mm, b) CIE spectrum of $N_2^{+\cdot}/O_2$, 40% beam reduction; accumulation time 8hrs; slit width 0.5mm. Superimposed on the spectrum are the A $^2\Pi_u \rightarrow$ X $^2\Pi_g$ $O_2^{+\cdot}$ emission bands reported in the literature (Ref.15).

Figure 5.6. a) CIE spectrum of $N_2^{+\cdot}/O_2$ versus CH_3^+/O_2, 40% beam reduction; accumulation time 8hrs; slit width 1 mm. b) CH_3^+/O_2, 40% beam reduction; accumulation time 10 hrs; slit width 0.5 mm. Superimposed on the spectrum are the A $^2\Pi_u \rightarrow$ X $^2\Pi_g$ $O_2^{+\cdot}$ emission band reported in the literature (Ref.15).

Figure 5.7. CIE spectrum of CH_3^+/O_2, 40% beam reduction; accumulation time 10hrs; slit width 0.5 mm. Superimposed on the spectrum are the Shumann-Runge (B $^3\Sigma_u^+$ — X $^3\Sigma_g^-$) O_2 emission bands reported in the literature (Ref.15).

Figure 5.1.

a) $^{+}CH_2OH \longrightarrow {}^{+}CH_2O + H^{\cdot}$

$\Delta H = 477\ kJ\ mol^{-1}$

b) $^{+}CH_2NH_2 \longrightarrow {}^{+}\dot{C}H_2NH + H^{\cdot}$

$\Delta H = 552\ kJ\ mol^{-1}$

c) $CH_3NO_2^{+\cdot} \longrightarrow CH_3NO^{+\cdot} + O$

$\Delta H = 229\ kJ\ mol^{-1}$

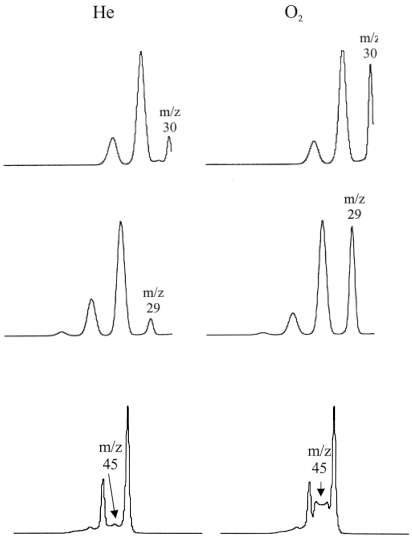

Figure 5.2.

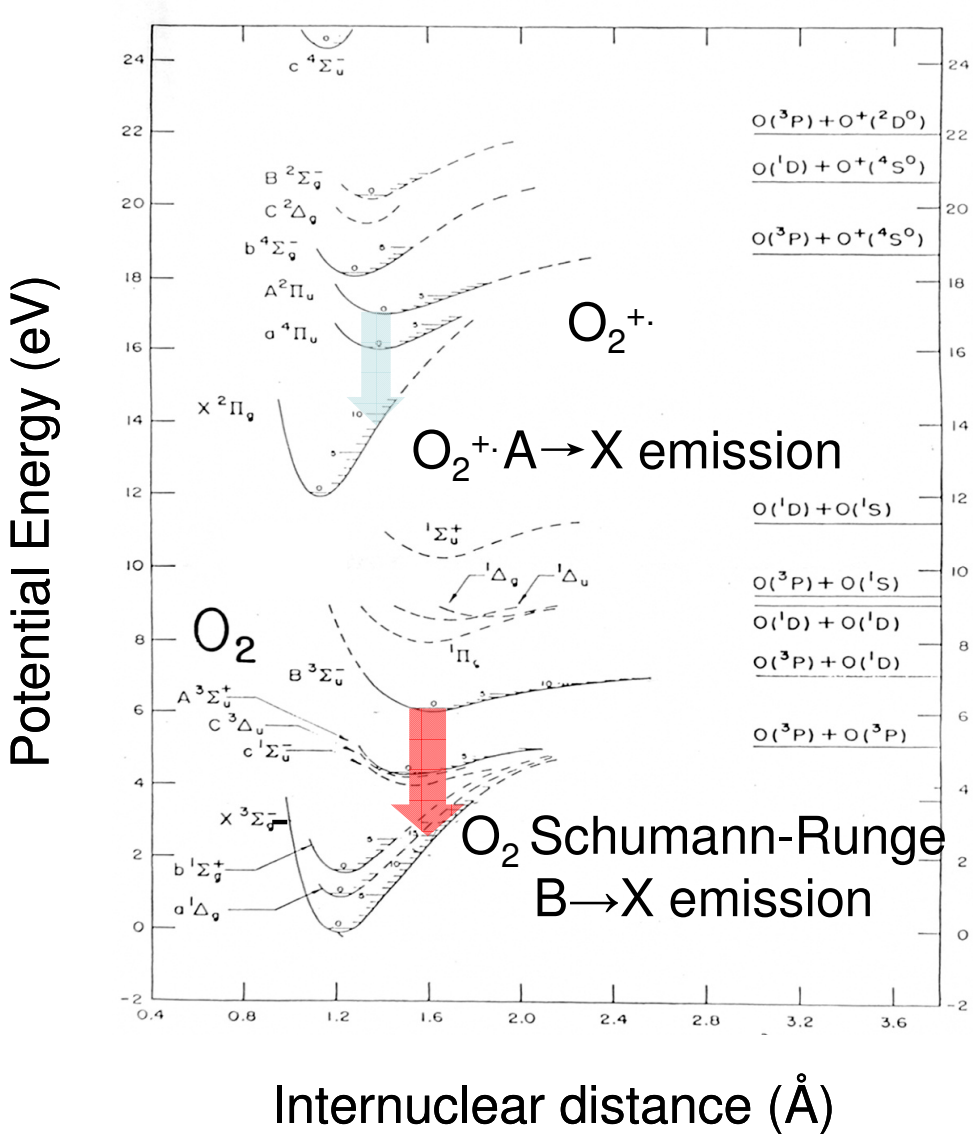
Potential Energy (eV)
Internuclear distance (Å)
$O_2^{+\cdot}$
$O_2^{+\cdot}$ A→X emission
O_2
O_2 Schumann-Runge
B→X emission
$O(^3P) + O^+(^2D^o)$
$O(^1D) + O^+(^4S^o)$
$O(^3P) + O^+(^4S^o)$
$O(^1D) + O(^1S)$
$O(^3P) + O(^1S)$
$O(^1D) + O(^1D)$
$O(^3P) + O(^1D)$
$O(^3P) + O(^3P)$

Figure 5.3.

a)

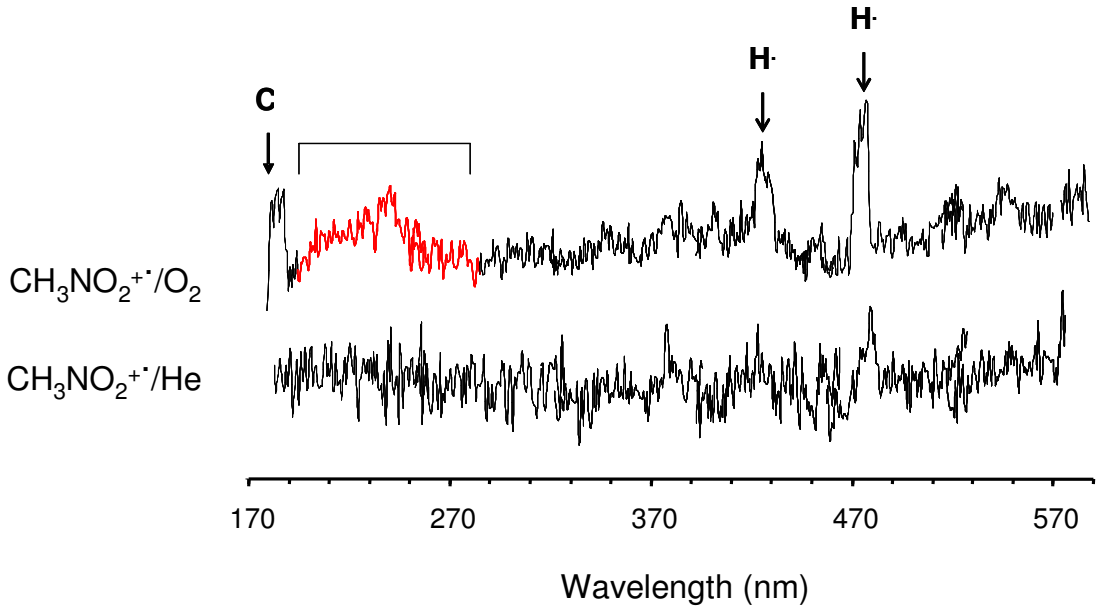
C
H·
H·
CH3NO2+·/O2
CH3NO2+·/He
170
270
370
470
570
Wavelength (nm)

b)

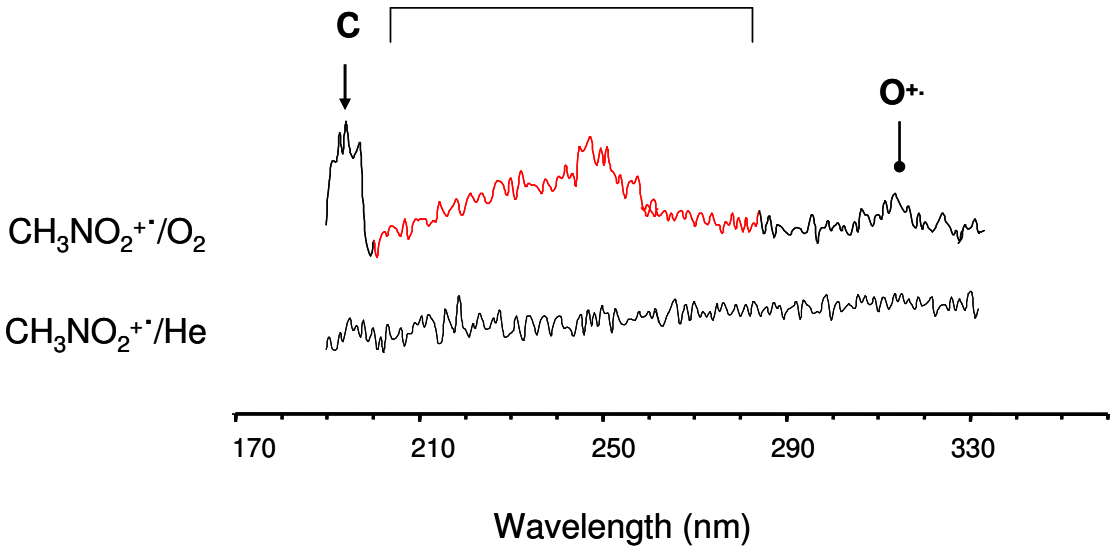
C
O+·
CH3NO2+·/O2
CH3NO2+·/He
170
210
250
290
330
Wavelength (nm)

Figure 5.4.

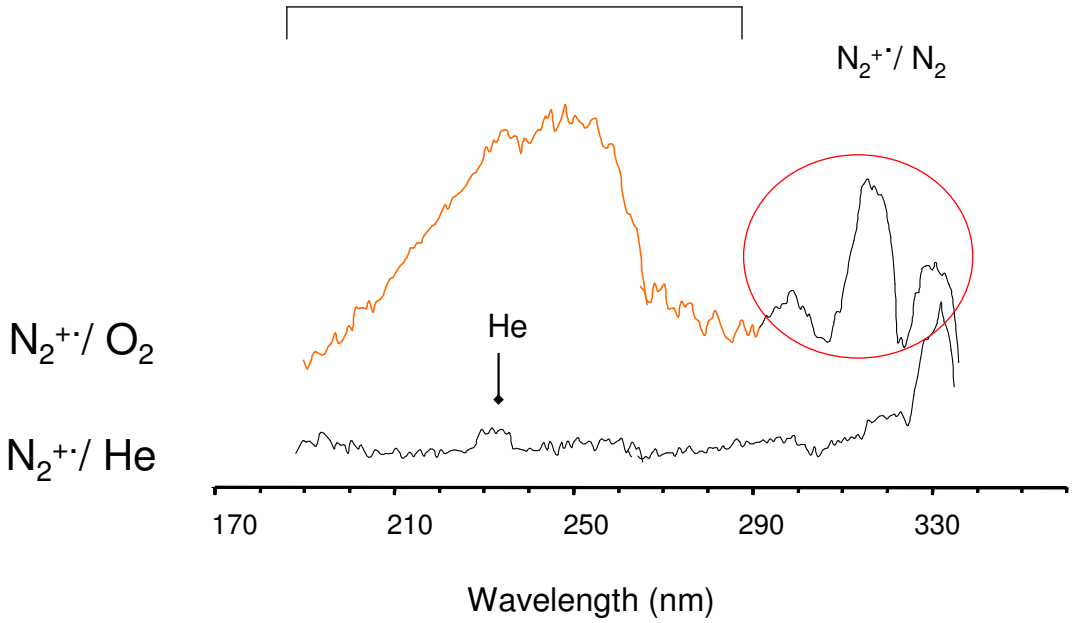
$N_2^{+\cdot}$/ N_2
$N_2^{+\cdot}$/ O_2
He
$N_2^{+\cdot}$/ He
170
210
250
290
330
Wavelength (nm)

Figure 5.5

a)

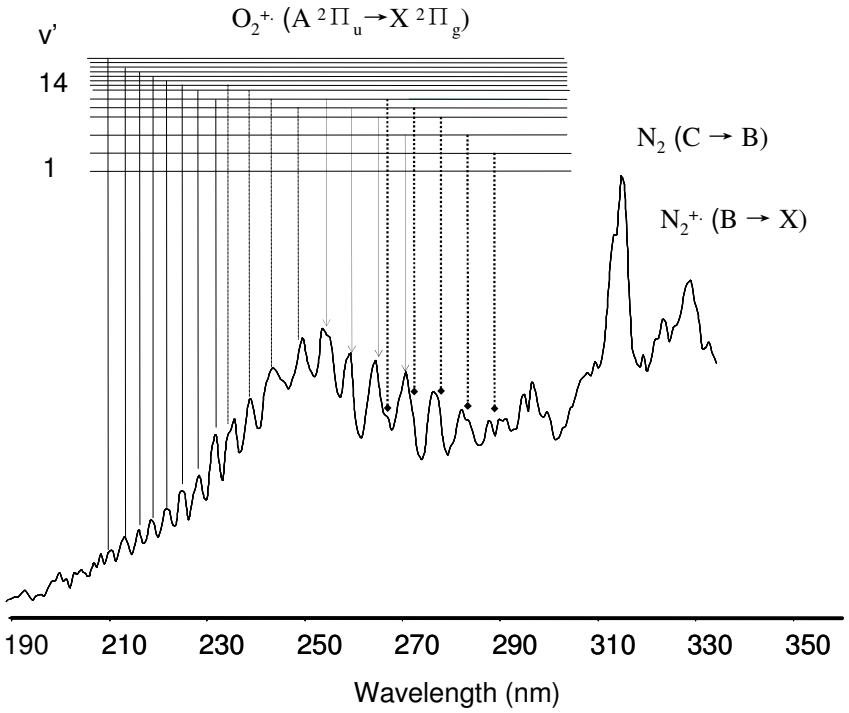
$O_2^{+\cdot}$ ($A\,^2\Pi_u \rightarrow X\,^2\Pi_g$)
v'
14
1
N_2 (C → B)
$N_2^{+\cdot}$ (B → X)
190
210
230
250
270
290
310
330
350
Wavelength (nm)

b)

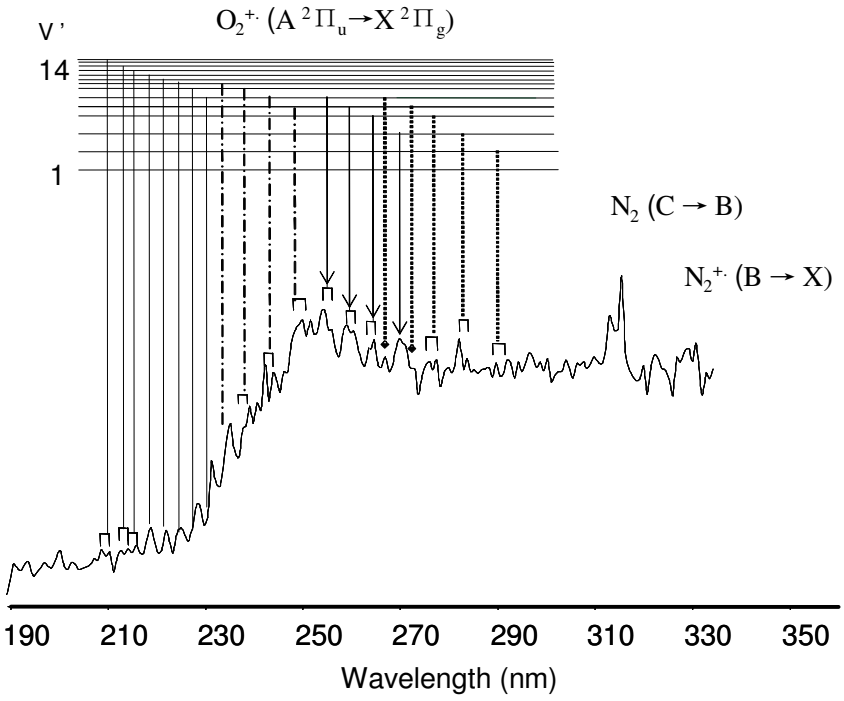
$O_2^{+\cdot}$ ($A\,^2\Pi_u \rightarrow X\,^2\Pi_g$)
v'
14
1
N_2 (C → B)
$N_2^{+\cdot}$ (B → X)
190
210
230
250
270
290
310
330
350
Wavelength (nm)

Figure 5.6

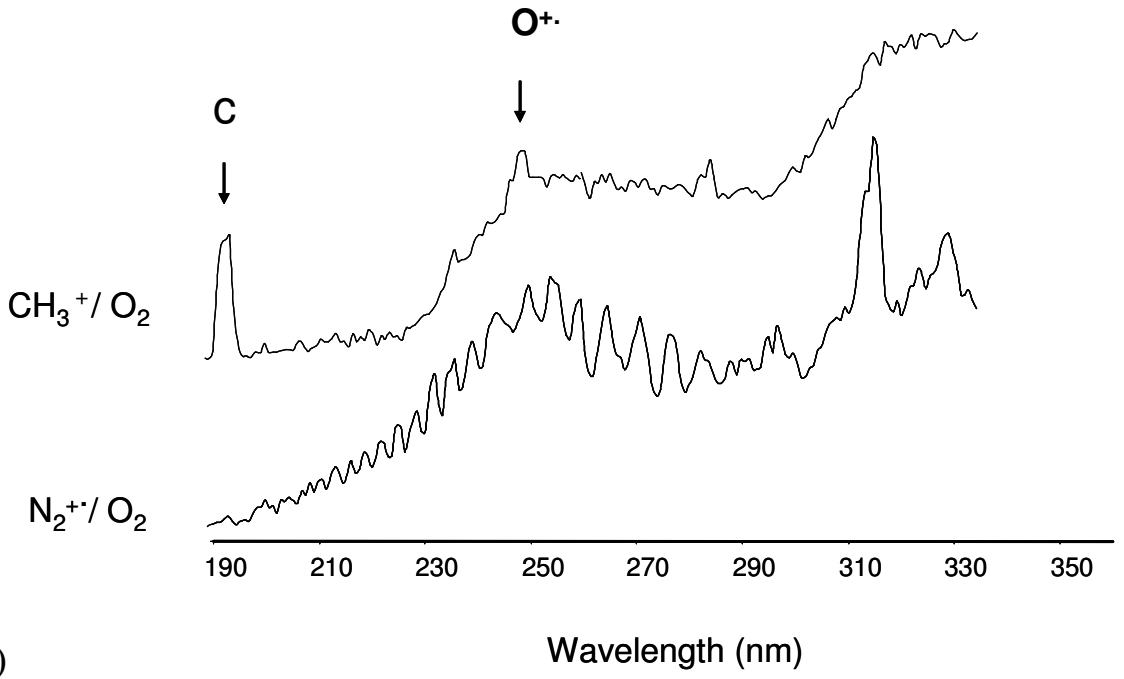
O+·
C
CH3+/ O2
N2+·/ O2
190
210
230
250
270
290
310
330
350
Wavelength (nm)

a)

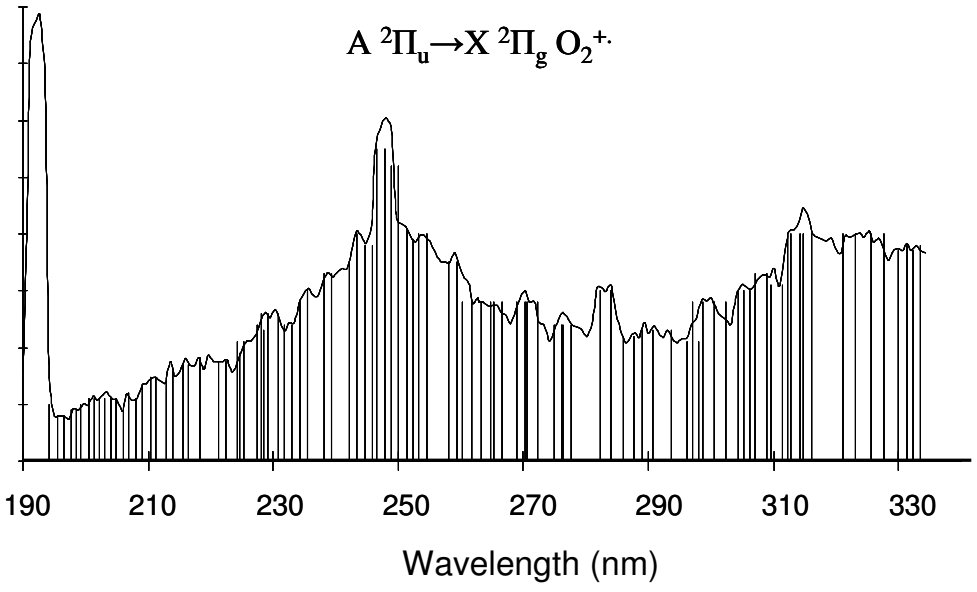
A 2Πu→X 2Πg O2+·
190
210
230
250
270
290
310
330
Wavelength (nm)

b)

Figure 5.7.

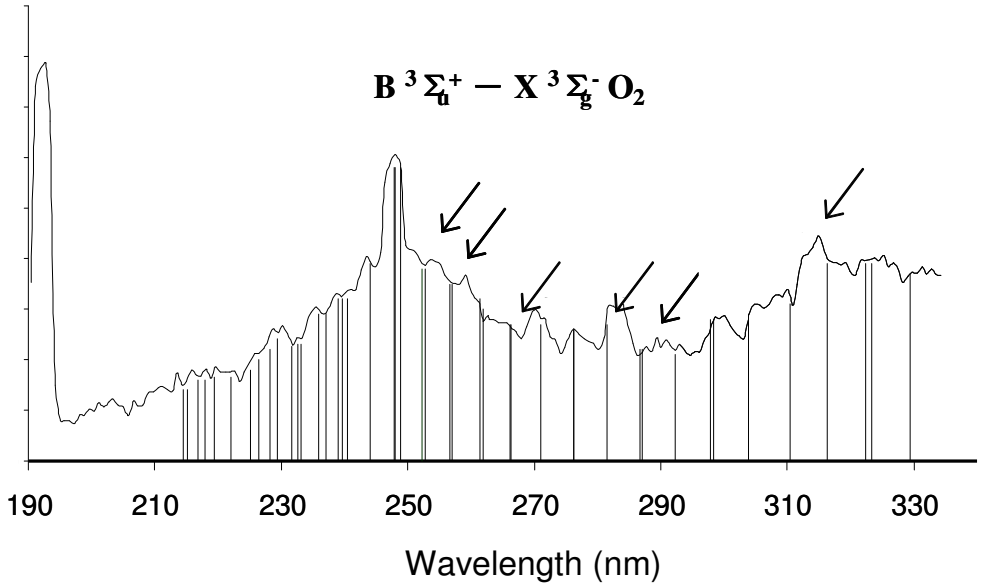

Chapter 6

Can neutral hydroxymethylene play a significant role in interstellar space? - A neutralization-reionization and reactivity mass spectrometry study

6.1 Introduction

The Green bank telescope (GBT), the world's largest fully steerable single aperture antenna, has been used to identify interstellar glycolaldehyde, the simplest aldehyde sugar in

space, one of the building blocks for life. This discovery was made by Hollis et al in 2001 [1]. One theoretical possibility for its formation is that *trans*-hydroxymethylene (*trans*-HCOH, **1a**) is first formed, which can readily combine with formaldehyde (H_2CO, **2a**) to produce glycolaldehyde, Equation 1 [2]:

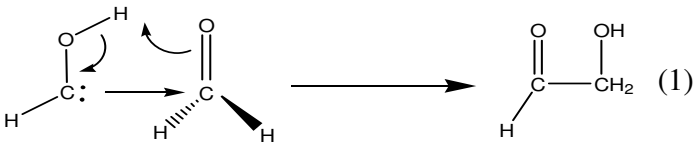

(1)

If interstellar **1a** were observed it would provide strong support for the mechanism by which glycolaldehyde is formed and also could be applied to the synthesis of more complex sugars in space.

Trans-HCOH, **1a**, an isomer of formaldehyde, is highly reactive because of its divalent carbon atom. It is an important intermediate in many chemical reactions, but due to its high reactivity all attempts to observe this species failed, until 2008 when Schreiner et al [3] first reported the generation of **1a** by high-vacuum flash pyrolysis of glyoxylic acid and its capture by matrix isolation. Under the conditions they employed it was found that **1a** rearranges to **2a** by hydrogen tunnelling through the isomerisation barrier.

In the present study we employ both neutralisation-reionization mass spectrometry (NRMS) and proton transfer reactions to generate neutral hydroxymethylene. The NRMS technique that has been described in detail elsewhere and has been used to generate a wide range of transient neutral species which are often inaccessible by standard preparative chemistry [4-7]. In the NRMS method, neutral species are first generated by a charge transfer

reaction between mass-selected projectile ions and the stationary neutralization target gas in a magnetic sector mass spectrometer. Subsequent reionization of the neutralized species further along the flight path provides a way to estimate the lifetime of the generated neutral. In this study, the projectile ion was accelerated to 8 keV translational energy so that the charge transfer process is quasi-vertical, the reaction time being fast relative to internuclear motion. The energetics of the neutralization reaction follow Equation 2

$$Q_N = NE(\text{precursor ion}) - IE(\text{neutralization gas}) \quad (2)$$

Where Q_N, NE and IE are the energy deficit of the reaction, the neutralization energy of the precursor ion and the ionization energy of the neutralization gas, respectively. When $Q_N = 0$ the reaction is said to be a symmetrical resonance charge transfer and an enhancement of the reaction cross section will occur [8]. In this way, by applying target gases with different ionization energies and observing the resulting reaction cross section, the vertical neutralization energy, NE_v, of the mass selected ion can be deduced.

In 1980s Mclafferty [9] and Holmes [10] reported the identification of $HCOH^+$ based on its CID mass spectrum, this allows structure identification of the neutralized HCOH in our NRMS experiment. The main goal of the present paper is to generate and identify hydroxymethylene (**1a)** by the NRMS technique and to compare our experimental results with quantum chemical calculations.

The neutral is also generated by ion-molecule reaction in which a proton is transferred from CH_2OH^+ to a base and the kinetic isotope effect for deprotonation at the C

atom is determined (this part of work were carried out by Crestoni and Fornarini from the univeriety of Roma).

6.2 Experimental procedure

6.2.1 Chemicals

CD_3OH (99.8 atom % D), CH_3OD (99.5 atom % D), and all other chemicals were research grade products purchased from Sigma-Aldrich.

6.2.2 Neutralization-reionization mass spectrometry

Tandem mass spectrometry experiments were performed on a modified VG ZAB mass spectrometer [7, 11] incorporating a magnetic sector followed by two electrostatic sectors (BEE geometry), shown in Figure 6.1. Precursor $[C,H_2,O]^+$ ions were generated from methanol and formaldehyde respectively by electron ionization in the ion source of the instrument using an electron energy of 100 eV. The sequence of events in NRMS is described below. The $[C,H_2,O]^+$ ion, with a m/z ratio of 30, was accelerated to 8 keV, mass selected by the magnetic sector and transmitted into the first collision cell (CC1) where it encountered the neutralization target gas. The mixture of ionic and neutral species leaving the first collision cell was separated by the beam deflector electrode to which a potential of +500 volts was applied so that only the neutrals continue on to the second collision cell (CC2) where they were reionized by collision with oxygen gas. The mass spectrum was obtained by

scanning the potential on the electrostatic analyser. Neutralization gases were chosen so that their IEs spanned the range between ~8.2 to ~12.5 eV (Table 6.1). To do a NR-CID experiment, the recovery signal, with m/z ratio of 30, was selected according to its kinetic energy with the first ESA and transmitted into the third field-free region and to the next collision cell (CC3) containing oxygen as the target gas. The resulting mass spectrum is called a NR-CID mass spectrum. To obtain reliable relative peak intensity values, all NR-CID spectra have been smoothed by combining data from every 10 pixel columns.

In all the collision experiments, collision gas was introduced into the collision cell to achieve a 20% beam reduction in the precursor ion beam flux. The pressure in the collision cells was read with ionization gauges located above the diffusion pump situated beneath each cell. The pressure value was in the range of 8×10^{-7} to 3×10^{-6} Torr.

6.2.3 FT-ICR mass spectrometry

The experiments were run on a Bruker BioApex 4.7 T Fourier transform ion cyclotron resonance (FT-ICR) mass spectrometer equipped with a cylindrical "infinity" cell within a 4.7 T superconducting magnet. Neutral compounds were leaked in the cell, maintained at ca. 300K, through needle valves up to constant pressures in the range of 0.5 - 6.0 $\times$ 10^{-8} mbar. The pressure were measured with a cold cathode sensor (IKR Pfeiffer Balzers S.p.A., Milan, Italy), calibrated by using the rate constant k = 1.1 $\times$ 10^{-9} cm^3 s^{-1} for the reference reaction $CH_4^{\cdot+} + CH_4 \rightarrow CH_5^+ + CH_3^{\cdot}$, and weighted by individual response factors. The ion of interest was isolated by ejection routines and allowed to react with the selected neutral. Pseudo-first-order rate constants were obtained from the slope of

semilogarithmic decrease of reactant ion abundance versus reaction time. The kinetics obeyed a pseudo first order rate law and the rate constants (k_{obs}) were obtained from the slope of the semilogarithmic decrease of reactant ion abundance versus reaction time. The pseudo first order rate constants divided by the substrate concentration yield the bimolecular rate constants (k_{exp}). The reaction efficiencies were calculated as % ratio of k_{exp} relative to the collision rate constant (k_c) calculated by parameterized trajectory theory [12]. The relative abundances of the BH^+ and BD^+ product ions were obtained by plotting the $[BH^+]/[BD^+]$ ratio as a function of time and taking the intercept at initial time. In this way spurious effects due further proton/deuteron transfer reactions or H/D exchange on the ions primarily formed are minimized. The elemental composition of the product ions was verified by m/z measurements at high resolution.

CD_2OH^+ and CH_2OD^+ ions were produced by electron ionization at 35 eV of labeled methanol, either CD_3OH or CH_3OD, respectively. In the presence of a base such as acetone (PA = 812 kJ mol^{-1}) exclusive H^+ or D^+ transfer was observed, respectively from CD_2OH^+ and CH_2OD^+ ions.

6.3 Theoretical procedure

6.3.1 Geometry Optimizations and Frequency Calculations

Standard *ab initio* molecular orbital calculations [13] were performed by using the Gaussian-03 suite of programs [14]. The geometries for all the species were calculated at

both the CCSD(T)/6-311++G(3df,2p) and QCISD/6-311+G(d,p) levels of theory. The optimized bond lengths and bond angles for **1a**, **2a**, $HCOH^+$ (**1b**) and H_2CO^+ (**2b**) are listed at Table 6.2. The resulting geometries and zero-point energies (ZPE) were used to obtain G3 total energies [15].

Transition states are further confirmed by the intrinsic reaction coordinate (IRC) procedure in the Gaussian programs. An IRC calculation starts at the saddle point, steps along the reaction path in both directions from the transition state in several small steps while optimize the geometry of the molecular system at each point along the path. As a transition state is a maximum along the reaction coordinate, IRC calculations should result in lowering the energy. A subsequent geometry optimization on the IRC structure should result in a local minimum. This procedure confirms that the saddle point found is the true transition state connecting the two minima on a potential energy surface.

6.3.2 Gaussian-3 (G3) Calculation

Gaussian 3 (G3) is one of the quantum chemistry composite methods that aim for high accuracy by combining the results of several calculations. They combine methods with a high level of theory and a small basis set with methods that employ lower levels of theory with larger basis sets. They are commonly used to calculate thermodynamic quantities such as enthalpies of formation, atomization energies, ionization energies and electron affinities. They aim for chemical accuracy which is usually defined as within 1 kcal/mol of the experimental value.

In G3 theory, an optimized geometry was used to carry out single-point energy calculations at the following levels of theory: MP4/ 6-31G(d), MP4/ 6-31G+(d), MP4/ 6-31G(2df,2p), QCISD(T)/6-31G(d) and MP2(full)/G3large.

The resulting energies are mathematically manipulated and modified by a series of corrections. Details of the G3 calculation can be found in the original publication by Curtiss et al [16]. The zero-point vibrational energy (ZPE) scale factors for QCISD/6-311+g(d,p) is 0.9812 [15]. The zero-point vibrational energy (ZPE) scale factors for CCSD(T)/6-311++G(3df,2p) have not been published, so we used the CCSD(T)/6-311+G(d,p) scale factor [15]. The resulting energy diagram is presented in Figure 6.2.

6.4 Results and discussion

6.4.1 CID experiments for $HCOH^+$ (1a) and H_2CO^+ (2a)

$[C,H_2,O]^+$ has 3 possible isomers, the formaldehyde ion **2b**, the hydroxymethylene ion **1b** and the oxonium ion COH_2^+. The latter has never been generated and characterized by experiment. **1b** and **2b** can be generated by the ionization of formaldehyde and dissociative ionization of methanol, respectively [9, 10]. The m/z 12 to m/z 18 region of their CID spectra differ sufficiently to allow identification these two isomers. In Figure 6.3, we present the CID mass spectra of the $[C,H_2,O]^+$ ion generated from formaldehyde and methanol. Ionized formaldehyde produces a CID mass spectrum in which the most prominent peak is m/z 14 (loss of O) while the most prominent peak is m/z 13 (loss of OH) when m/z 30 is formed from methanol, in agreement with earlier reports [9, 10]. CID experiments were performed

on different days and using two different collision cells, CC1 and CC3. The spectra are reproducible, confirming that the two isomers can be distinguished based on the intensity ratio of peaks with m/z 13 and m/z 14 (Table 6.2). The calculated geometries for **1** and **2** (ions and neutrals), listed in Table 6.3, are in close agreement with those reported by Matus et al [17]. The presently calculated adiabatic ionization energy IE_a of H_2CO is 10.89 and 10.90 eV, by the QCISD and CCSD(T) levels of theory, respectively, in good agreement with the experimental value 10.88 ± 0.001 eV [18]. The calculated energy barrier for the isomerization of **2a** to **1a** is 183.4 kJ/mol (QCISD) and 184.4 kJ/mol (CCSD); both are smaller than that obtained from a previous MP3/6-31G**calculation [19], 192.9 kJ/mol.

6.4.2 Neutralization-reionization (NR) for *trans*-^{1}HCOH (1b) and H_2CO (2b)

The NR mass spectra of m/z 30 ions generated from formaldehyde and methanol are presented in Figure 6.4. Strong recovery signals were observed in both spectra confirming that the [C,H_2,O] neutrals, whose life times are long enough for them to travel the distance between the CC1 and CC2, 100 mm, were produced during the neutralization process [7]. By using standard equations [20], we estimate that the lifetime of [C,H_2,O] neutrals exceeds 13.9 μs at 8000 eV, but the question remains as to whether the neutrals are formaldehyde or hydroxymethylene. If the neutrals produced in NR were all of the formaldehyde structure, then the NR-CID spectra should only have the features of formaldehyde CID mass spectrum. Thus, by comparing the CID mass spectra with the corresponding NR-CID mass spectra, the [C,H_2,O] neutrals produced in CC1 can be identified.

6.4.3 NR-CID experiments to identify *trans*-^{1}HCOH (1b)

The NR-CID mass spectra obtained, using oxygen as target gas in CC1, CC2 and CC3 and 500eV on the ion deflector, are shown in Figure 6.5. The signal intensities for both spectra are obviously weaker than the CID and NR mass spectra. This is because only a fraction of the precursor ions were neutralized and reionized before being transmitted to the 3FFR. The relative peak intensities for both spectra are listed in Table 6.2. The formaldehyde NR-CID mass spectrum, with a relative peak intensity of 20:100 for fragment ions m/z 13 and 14, is quite similar to its CID spectrum (23:100), indicating that the [C,H_2,O] species produced by the charge transfer neutralization in CC2 retain the formaldehyde structure. The NR-CID mass spectrum of m/z 30 ions generated from methanol, with a relative peak intensity ratio of 54:100, is very different from that of formaldehyde indicating that most of the neutrals produced are evidently not solely formaldehyde. However, compared with the corresponding CID mass spectrum of hydroxymethylene (relative peak intensity of 100:60) the neutral species produced are not mostly hydroxymethylene either, but are a mixture of formaldehyde and hydroxymethylene, the former resulting from the fast rearrangement of neutral hydroxymethylene.

6.4.4 Vertical neutralizaiton energy (NEv) experiments

As described in the introduction, to maximize the yield of hydroxymethylene, a neutralization gas whose IE equals the NEv of $HCOH^+$ should be used. In our calculation, the energy of *trans*-^{1}HCOH **(1b)** relative to H_2CO **(2b)**, 219.9 kJ/mol (QCISD) and 219.8 kJ/mol (CCSD), is smaller than that reported by Schreiner et al (225.9 kJ/mol) [3] and slightly larger than a recently reported value 214.6 kJ/mol from CCSD(T)/CBS by Kiselev et al [21]. The calculated isomerization energy barrier of **1b** (126.8 kJ/mol (QCISD) and 127.4

kJ/mol (CCSD)) is in close agreement with the CCSD(T)/CBS calculated value (126.8 kJ/mol) [21]. The vertical neutralization NE_v of **1a** (Figure 6.2) is 8.22 eV (QCISD) and 8.20 eV(CCSD). Three neutralization target gases dimethylamine, *trans*-2-butene and 1-butene with IEs ranging from 8.2 to 9.6 eV were used. The properties of the neutralization gases are summarized in Table 6.1. The resulting NR-CID mass spectra of m/z 30 generated from methanol employing each of these gases in CC1 are shown in Figure 6.6. The relative peak intensities obtained from each spectrum are listed in Table 6.1, along with the calculated ratios of formaldehyde and hydroxymethylene in the [C,H_2,O] mixtures. As indicated from the Table, when the IE of the chosen neutralization gas energy is 8.22 eV, the calculated NEv value of **1a**, the fraction of neutrals having the HCOH connectivity increased due to the enhancement of the charge-transfer cross section. Note that even when the neutralization gas used is dimethylamine (IE 8.24 eV), there is still 40% of formaldehyde produced. To explain this result, note that the energy barrier for **1a** to isomerize to **2a** is 27.3 kJ/mol (QCISD) and 27.2 kJ/mol (CCSD) higher than that for **1b** to isomerize to **2b.** Some of the $HCOH^+$ ions from the ion source may have internal energies in excess of 127.4 kJ/mol and still be below the ion isomerization barrier. After undergoing neutralization with dimethylamine, this excess energy is sufficient to allow HCOH to overcome the energy barrier and isomerize to H_2CO, as is shown in Figure 6.2.

6.4.5 Proton transfer reactions

We also attempted to trap neutral hydroxymethylene in the gas phase by ion-molecule reaction. The hydroxylmethyl cation, CH_2OH^+, could yield hydroxymethylene upon reaction with a base strong enough to abstract a proton from carbon [22]. Deprotonation

from oxygen is favoured, though, by the difference in enthalpy of formation of the two conjugate bases, namely formaldehyde and hydroxymethylene, amounting to 219.8 kJ/mol (Figure 6.2). It was reasoned that if the active basic site was placed in the same molecule holding a functional group that could act as a methylene scavenger, the proton transfer could be followed by a fast trapping reaction within the ion-molecule complex. To this end 2-vinylpyridine was selected as a probe owning to both a highly basic N atom and a double bond susceptible to cyclopropanation by carbenes, Equation 3 [23].

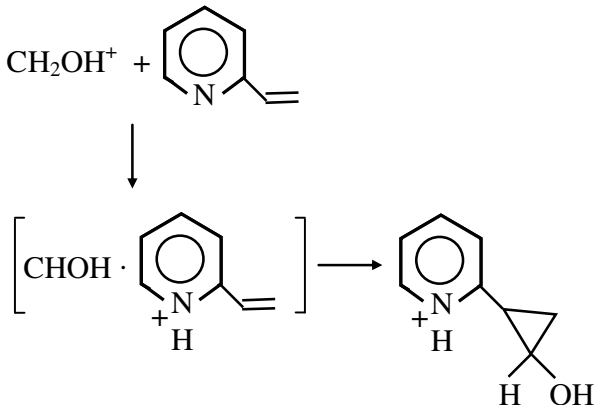

(3)

The expected reaction was, however, not observed, the only product ion being the protonated base. The effectiveness of carbon deprotonation by pyridine bases has been further confirmed examining the reaction of deuterium labeled ions with pyridine and 4-methylpyridine (4-picoline) as bases (B), whose proton affinity is reported equal to 930 and 947 kJ/mol [18]. The reaction of CD_2OH^+ and CH_2OD^+ with B yields both BH^+ and BD^+ product ions in the relative ratios listed in Table 6.4. The proton transfer from CH_2OD^+ and the deuteron transfer from CD_2OH^+ confirm that carbon deprotonation is occurring and the product ratios lend themselves to estimate the relative kinetic isotope effect (KIE) associated to the reaction (Equation 6.4 and 6.5).

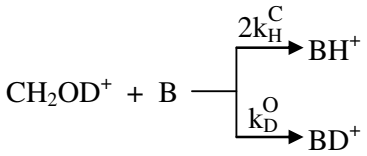

$$\frac{[BH^+]}{[BD^+]} = \frac{2k^C_H}{k^O_D} = \begin{matrix} 2.46 \pm 0.26 \text{ (B = pyridine)} \\ 1.83 \pm 0.16 \text{ (B = 4-picoline)} \end{matrix} \qquad (6.4)$$

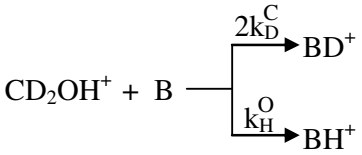

$$\frac{[BD^+]}{[BH^+]} = \frac{2k^C_D}{k^O_H} = \begin{matrix} 0.76 \pm 0.16 \text{ (B = pyridine)} \\ 0.70 \pm 0.06 \text{ (B = 4-picoline)} \end{matrix} \qquad (6.5)$$

In order to evaluate the net kinetic isotope effect affecting deprotonation at carbon (k^C_H/k^C_D) one needs to know the KIE for deprotonation at the hydroxyl group. The latter reaction is strongly exothermic, given a PA of formaldehyde of 713 kJ/mol [18]. The ratio k^O_H/k^O_D is then expected to be close to 1 [24]. To obtain an experimental value supporting this assumption, the ion corresponding to protonated methanol D-labelled on the hydroxyl group, CH_3OHD^+, was allowed to react with either pyridine or 4-picoline in the FT-ICR cell (Equation 6.6).

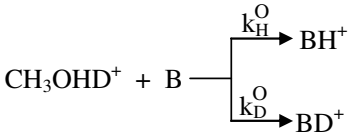

$$\frac{[BH^+]}{[BD^+]} = \frac{k^O_H}{k^O_D} = \begin{matrix} 1.06 \pm 0.02 \text{ (B = pyridine)} \\ 1.15 \pm 0.02 \text{ (B = 4-picoline)} \end{matrix} \qquad (6.6)$$

The so-obtained ratios of the relative abundances of BH^+ and BD^+ formed in the initial stages of the reactions are also listed in Table 6.4. The data yield $k^O_H/k^O_D = 1.06 \pm 0.02$ (B = pyridine) and $k^O_H/k^O_D = 1.15 \pm 0.02$ (B = 4-picoline), two values reasonably close to unity. Taking them into account the KIE for reaction at C, $k^C_H/k^C_D = 3.05$ (B = pyridine) and 2.27 (B = 4-picoline) are obtained. The higher KIE for carbon deprotonation by pyridine is accounted for by the thermoneutrality of the reaction which instead becomes exothermic

by about 20 kJ mol^{-1} in the case of 4-picoline (the PA at C of HCOH is 933 kJ mol^{-1}, based on the PA of formaldehyde and the relative energies of **1b** and **2b** shown in Figure 6.2). These findings thus confirm that deprotonation at the carbon atom of the hydroxymethyl cation can provide a viable route to hydroxymethylene that may potentially be exploited for further investigations about this fleeting species of astrochemical and pre-biotic interest. On quantitative grounds it has been possible to measure the KIE affecting the proton transfer from carbon to two exemplary pyridine bases of known proton affinity.

6.5 Conclusions

We have calculated the optimized equilibrium geometries of neutral and ionized hydroxymethylene and formaldehyde at the QCISD/6-311+G(d,p) and CCSD(T)/6-311++G(3df,2p) levels of theory, along with their G3 energies based on the QCISD/6-31G(d) theory level. The vertical IE_v and NE_v have also been calculated.

The existence of hydroxymethylene, with a life time exceeding 13.9 μs, has been confirmed using neutralization-reionization mass spectrometry. The maximum in the relative charge-transfer cross section as a function of IE of the neutralization gas has also been investigated and found to occur at ~8.2 eV, in agreement with our calculated NE_v of $HCOH^+$. Neutral hydroxymethylene can also be produced by proton transfer from CH_2OH^+ to a strong base such as pyridine. There is a kinetic isotope effect for H^+ vs. D^+ transfer from C of ~ 3 due to the near thermoneutrality of the reaction.

REFERENCES

1. Hollis, J. M.;Vogel, S. N.; Snyder, L. E.; Jewell, P. R.; Lovas, F. J. The Spatial Scale of Glycolaldehyde in the Galactic Center. *Ap. J.* **2001**, *554*(1-2), 81-85.
2. Hollis, J. M., Complex Molecules and the GBT: Is Isomerism the Key? In *Proceedings of the International Astronomical Union*, Lis, D. C.; Blake, G. A.; Herbst, E., eds.; Cambridge University Press: Cambridge, 2005; p. 227.
3. Schreiner, P. R.; Reisenauer, H. P.; Frank, C. P. IV; Simmonett, A. C.; Allen, W. D.; Mátyus E.; Császár, A. G. Capture of Hydroxymethylene and its Fast Disappearance through Tunnelling. *Nature.* **2008**, *453*(7197), 906-909.
4. Tureček, F. Transient Intermediates of Chemical Reactions by Neutralization-Reionization Mass Spectrometry. *Top. Curr. Chem.* **2003**, *225*, 77-129.
5. Cacace, F.; de Petris, G.; Troiani, A. Experimental Detection of the H_2NO_3 Radical. *Chem. Phys.* **2003**, *4*(10), 1128-1131.
6. Holmes, J. L.; Aubry, C.; Mayer, P. M. *Assigning Structures to Ions in Mass Spectrometry*, CRC: Boca Raton, 2006; p. 65.
7. Rennie, E. E.; Mayer, P. M. Confirmation of the "long-lived" Tetra-nitrogen (N4) Molecule using Neutralization-reionization Mass Spectrometry and *ab initio* Calculations. *J. Chem. Phys.* **2004**, *120*(22), 10561-10578.
8. Parker, J. E.; Lehrle, R. S. Ion-Molecule Reactions. *Int. J. Mass Spectrom. Ion Phy.* **1971**, *7*(6), 421-469.
9. Wesdemiotis, C.; McLafferty, F. W. Mass Spectral Evidence for the Hydroxymethylene Radical Cation. *Tetrahedron Lett.* **1981**, *22*(36), 3479-3480.

10. Burgers, P. C.; Mommers, A. A.; Holmes, J. L. Ionized Oxycarbenes: Hydroxymethylidyne Cation ($[COH]^+$), Hydroxymethylene Cation ($[HCOH]^+$.bul.), Dihydroxymethylene Cation ($[C(OH)_2]^+$.bul.), Formoxylium Cation ($[HCO_2]^+$) and Carboxyl Cation ($[COOH]^+$), Their Generation, Identification, Heat of Formation, and Dissociation Characteristics. *J. Am. Chem. Soc.* **1983**, *105*(19), 5976-5979.
11. Holmes, J. L.; Mayer, P. M. A Combined Mass Spectrometric and Thermochemical Examination of the C_2,H_2,N Family of Cations and Radicals. *J. Phys. Chem.* **1995**, *99*(4), 1366-1370.
12. Su, T.; Chesnavich, W. J. Parametrization of the Ion-polar Molecule Collision Rate Constant by Trajectory Calculations. *J. Chem. Phys.* **1982**, *76*(10), 5183-5185.
13. Hehre, W. J.; Radom, L.; Schleyer, P. v.R.; Pople, J. A. *Ab Initio Molecular Orbital Theory*, Wiley Interscience: New York, 1986.
14. Gaussian 03, Revision C.02, Frisch, M. J.; Trucks, G. W.; Schlegel, H. B.; Scuseria, G. E.; Robb, M. A.; Cheeseman, J. R.; Montgomery, Jr., J. A.; Vreven, T.; Kudin, K. N.; Burant, J. C.; Millam, J. M.; Iyengar, S. S.; Tomasi, J.; Barone, V.; Mennucci, B.; Cossi, M.; Scalmani, G.; Rega, N.; Petersson, G. A.; Nakatsuji, H.; Hada, M.; Ehara, M.; Toyota, K.; Fukuda, R.; Hasegawa, J.; Ishida, M.; Nakajima, T.; Honda, Y.; Kitao, O.; Nakai, H.; Klene, M.; Li, X.; Knox, J. E.; Hratchian, H. P.; Cross, J. B.; Bakken, V.; Adamo, C.; Jaramillo, J.; Gomperts, R.; Stratmann, R. E.; Yazyev, O.; Austin, A. J.; Cammi, R.; Pomelli, C.; Ochterski, J. W.; Ayala, P. Y.; Morokuma, K.; Voth, G. A.; Salvador, P.; Dannenberg, J. J.; Zakrzewski, V. G.; Dapprich, S.; Daniels, A. D.; Strain, M. C.; Farkas, O.; Malick, D. K.; Rabuck, A. D.; Raghavachari, K.; Foresman, J. B.; Ortiz, J. V.; Cui, Q.; Baboul, A. G.; Clifford, S.; Cioslowski, J.; Stefanov, B. B.; Liu, G.; Liashenko, A.; Piskorz, P.; Komaromi, I.; Martin, R. L.; Fox, D. J.; Keith, T.; Al-Laham,

M. A.; Peng, C. Y.; Nanayakkara, A.; Challacombe, M.; Gill, P. M. W.; Johnson, B.; Chen, W.; Wong, M. W.; Gonzalez, C.; and Pople, J. A.; Gaussian, Inc., Wallingford CT, 2004.

15. Merrick, J. P.; Moran, D.; Radom, L. An Evaluation of Harmonic Vibrational Frequency Scale Factors. *J. Phys. Chem. A.* **2007**, *111*(45), 11683-11700.
16. Curtiss, L. A.; Raghavachari, K.; Redfern, P. C.; Rassolov, V.; Pople, J. A. Gaussian-3 (G3) Theory for Molecules Containing First and Second-row Atoms. *J. Chem. Phys.* **1998**, *109*(18), 7764-7776.
17. Matus, M. H.; Nguyen, M. T.; Dixon, D. A. Heats of Formation and Singlet-triplet Separations of Hydroxymethylene and 1-hydroxyethylidene. *J. Phys. Chem. A.* **2006**, *110*(28), 8864-8871.
18. NIST Chemistry WebBook, NIST Standard Reference Database Number 69,National Institute of Standards and Technology,Gaithersburg MD, 20899, http://webbook.nist.gov, P.J. Linstrom and W.G. Mallard, Eds., (retrieved June 2, 2010)
19. Glaser, R. Diazonium Ions: A Theoretical Study of Pathways to Automerization, Thermodynamic Stabilities, and Topological Electron Density Analysis of the Bonding. *J. Phys. Chem.* **1989**, *93*(24), 7993–8003.
20. Barnard, G. P. *Modern Mass Spectrometry*, The Institute of Physics: London, 1953; p. 42
21. Kiselev, V. G.; Swinnen, S.; Nguyen, V. S.; Gritsan, N. P.; Nguyen, M. T. Fast Reactions of Hydroxycarbenes: Tunneling Effect versus Bimolecular Processes. *J. Phys. Chem. A.* **2010**, *114*(17), 5573–5579.
22. Pau, C. F.; Hehre, W. J. Relative Thermochemical Stabilities of Hydroxymethylene and Formaldehyde by Ion Cyclotron Double Resonance Spectroscopy *J. Phys. Chem.* **1982**, *86*(8), 1252-1253.

23. Smith, M. B.; March, J. *March's Advanced Organic Chemistry: Reactions, Mechanisms, and Structure*, 6th ed.; John Wiley & Sons: New Jersey, 2007.

24. Melander, L. C. S.; Saunders, W. H. *Reaction Rates of Isotopic Molecules* R. E. Kruger: Melbourne, 1987

Table 6.1. Properties of neutralization gases and data from the corresponding NR-CID mass spectra

Neutralization gas	[a]Ionization energy (eV)	Polarizability [a] $Å^3$	[b]I_{13}:I_{14}	[c]HCOH : H_2CO
Dimethylamine	8.24	5.447	91 : 100	60 : 40
trans-2-butene	9.13	8.49	62 : 100	38: 62
1-butene	9.55	7.97	49 : 100	27 : 73
Oxygen	9.59	1.5812	46 : 100	24 : 76

[a] Obtained from Ref. [18]

[b] I_{13} and I_{14} represent the peak intensities of ions with m/z 13 and m/z 14 in the NR-MS spectra

[c]HCOH : HCHO the estimated ratio of HCOH and H_2CO yield, relative to $\Sigma = 100$

Table 6.2. Peak intensity ratios of ions having m/z 13 realtive to those with m/z 14 in the CID and NR-CID mass spectra of $[C,H_2,O]^+$ ions

[a]I_{13}:I_{14} from mass spectra of the C,H_2,O isomers		
Reagent[b]	CID	NR-CID
[a]H_2CO	23:100	20:100
[b]CH_3OH	100:60	46:100

[a] To calculate the relative peak intensities, all NR-CID spectra have been smoothed by combining data from every 10 pixel columns.

[b]m/z 30 ions were obtained from electron impact of H_2CO and CH_3OH vapour

Table 6.3. Optimized Bond Lengths (Å) and Bond Angles (°) for **1a**, **2a**, **1b** and **2b**

molecule	Level of theory	r_{HC}	r_{CO}	r_{OH}	∠HCO	∠HCH	∠HCOH
^1H_2CO	QCISD(T)/6-311G(d, p)	1.1038	1.2078		121.8	116.5	180.0
2a	CCSD(T)/6-311++G(3df, 2p)	1.1038	1.2078		121.8	116.5	180.0
	[a]exp	1.1005	1.2033		121.9	116.2	180.0
	[b]CCSD(T)/aVDZ	1.1031	1.2115		121.7	116.6	180.0
H_2CO^+	QCISD(T)/6-311G(d, p)	1.1156	1.2019		119.4	121.1	180.0
2b	CCSD(T)/6-311++G(3df, 2p)	1.1152	1.1957		119.4	120.98	180.0
	[b]CCSD(T)/aVDZ	1.1143	1.2001		119.4	121.2	180.0
molecule	Level of theory	r_{HC}	r_{CO}	r_{OH}	∠HCO	∠COH	∠HCOH
trans-^{1}HCOH	QCISD(T)/6-311G(d, p)	1.1168	1.3173	0.9646	102.1	107.6	180.0
1a	CCSD(T)/6-311++G(3df, 2p)	1.1140	1.3142	0.9654	102.3	107.9	180.0
	[b]CCSD(T)/aVDZ	1.1138	1.3195	0.9677	102.1	107.7	180.0
	[c]CCSD(T)/cc-pCVQZ	1.111	1.311	0.964	102.3	107.8	180.0
$HCOH^+$	QCISD(T)/6-311G(d, p)	1.1014	1.2251	0.9863	124.6	116.7	180.0
1b	CCSD(T)/6-311++G(3df, 2p)	1.0994	1.2215	0.9870	124.3	117.7	180.0
	[b]CCSD(T)/aVDZ	1.0993	1.2255	0.9895	124.4	117.3	180.0

[a] Ref. [18]

[b] Ref. [17]

[c] Ref. [3]

Table 6.4. Relative abundances (%) of the BH^+ and BD^+ product ions formed in the reaction of a base B with D-labeled hydroxymethyl cation and protonated methanol.[a]

B	CH_2OD^+		CD_2OH^+		CH_3ODH^+	
	BH^+	BD^+	BH^+	BD^+	BH^+	BD^+
Pyridine	69	31	64	36	51	49
	74	26	55	45	52	48
	73	27	60	40		
	70	30	53	47		
	69	31				
4-Picoline	61	39	57	43	54	46
	65	35	60	40	53	47
	66	34	62	38		
	66	34	57	43		

[a] The proton/deuteron transfer reactions proceed all at nearly collision controlled rate, namely with unit reaction efficiency.

Figures Captions

Figure 6.1. A simplified layout (not to scale) of the modified VG-ZAB with BEE geometry showing collision cells and deflector electrodes. FFR, CC and ESA represent field-free region, collision cell and electrostatic analyzer for short.

Figure 6.2. Schematic relative G3 energies for CCSD(T)/6-311++G(3df,2p) level of theory. Values in italics are QCISD/6-311+g(d,p) G3 energies. Numbers in brackets are NE_v values in the unit of kJ/mol. Numbers in the double arrows are the energy differences between two states.

Figure 6.3. Collision induced dissociation mass spectra of $[C,H_2,O]^+$ produced from respectively (a) formaldehyde, (b) methanol.

Figure 6.4. Neutralization-reionization mass spectra of $[C,H_2,O]^+$ produced from respectively (a) formaldehyde, (b) methanol.

Figure 6.5. Neutralization-reionization-collision induced dissociation mass spectra of $[C,H_2,O]^+$ produced from respectively (a) formaldehyde, (b) methanol.

Figure 6.6. Neutralization-reionization-collision induced dissociation mass spectra of $[C,H_2,O]^+$ produced from methanol with collision gases as respectively (a) 1-butene/ O_2/ O_2, (b) 2-butene/ O_2/ O_2, (c) dimethylamine/ O_2/ O_2.

Figure 6.1

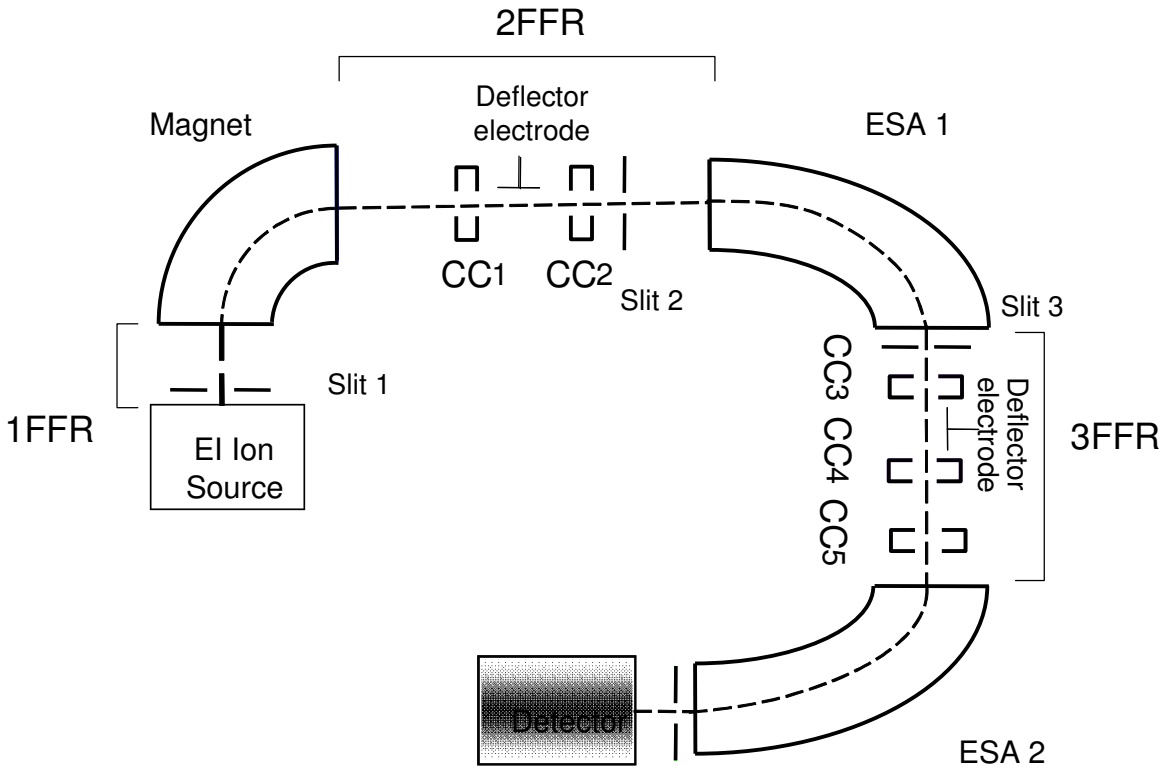
2FFR
Deflector
electrode
Magnet
ESA 1
CC1
CC2
Slit 2
Slit 3
Slit 1
1FFR
EI Ion
Source
CC3 CC4 CC5
Deflector
electrode
3FFR
Detector
ESA 2

Figure 6.2

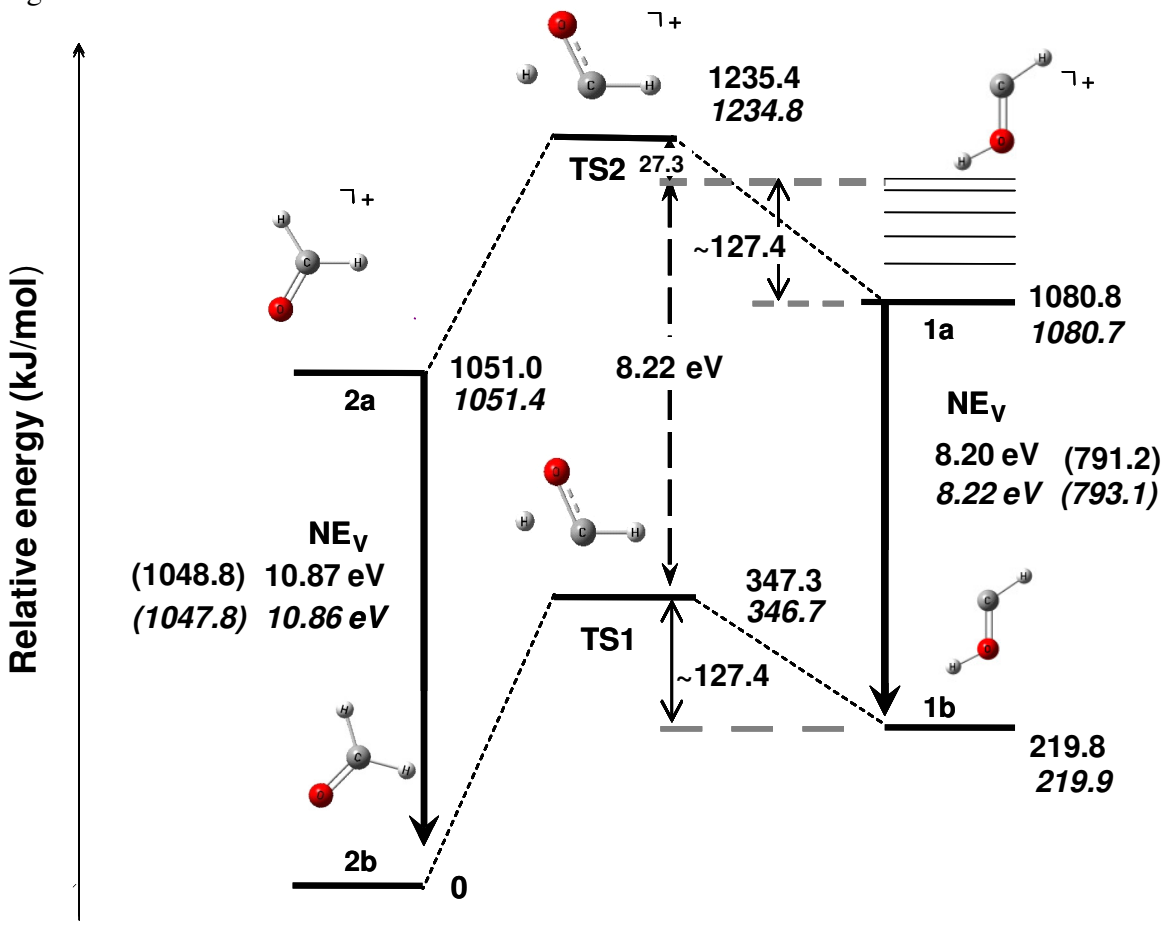
Relative energy (kJ/mol)
1235.4
1234.8
TS2
27.3
~127.4
1080.8
1080.7
1a
1051.0
1051.4
2a
8.22 eV
NE$_V$
8.20 eV (791.2)
8.22 eV (793.1)
NE$_V$
(1048.8) 10.87 eV
(1047.8) 10.86 eV
347.3
346.7
TS1
~127.4
1b
219.8
219.9
2b
0

Figure 6.3.

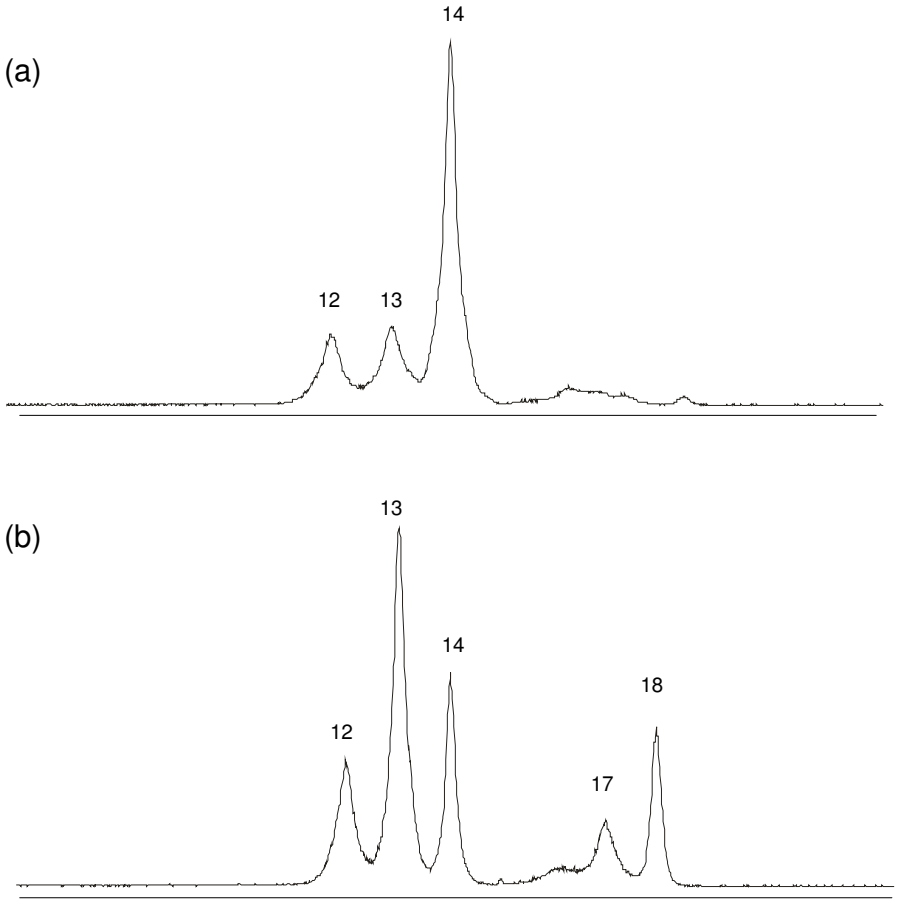

Figure 6.4

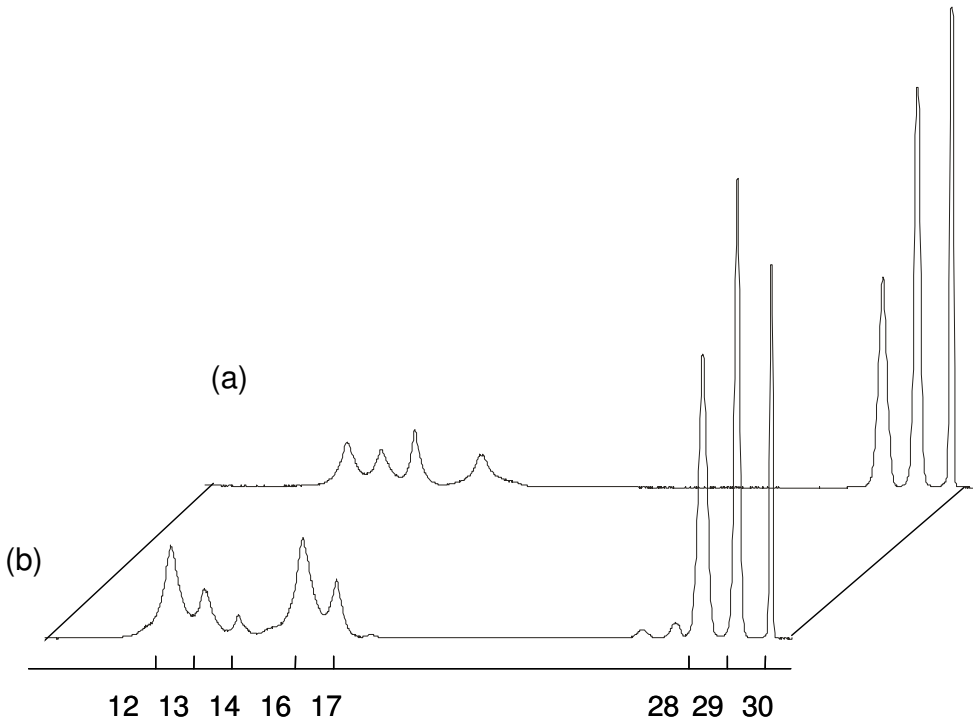

Figure 6.5.

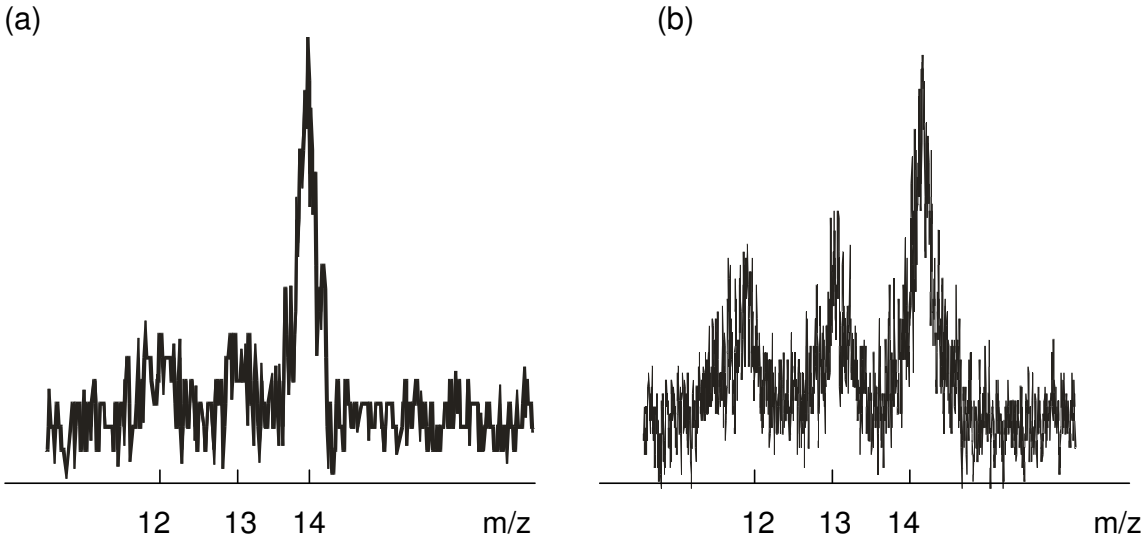

Figure 6.6.

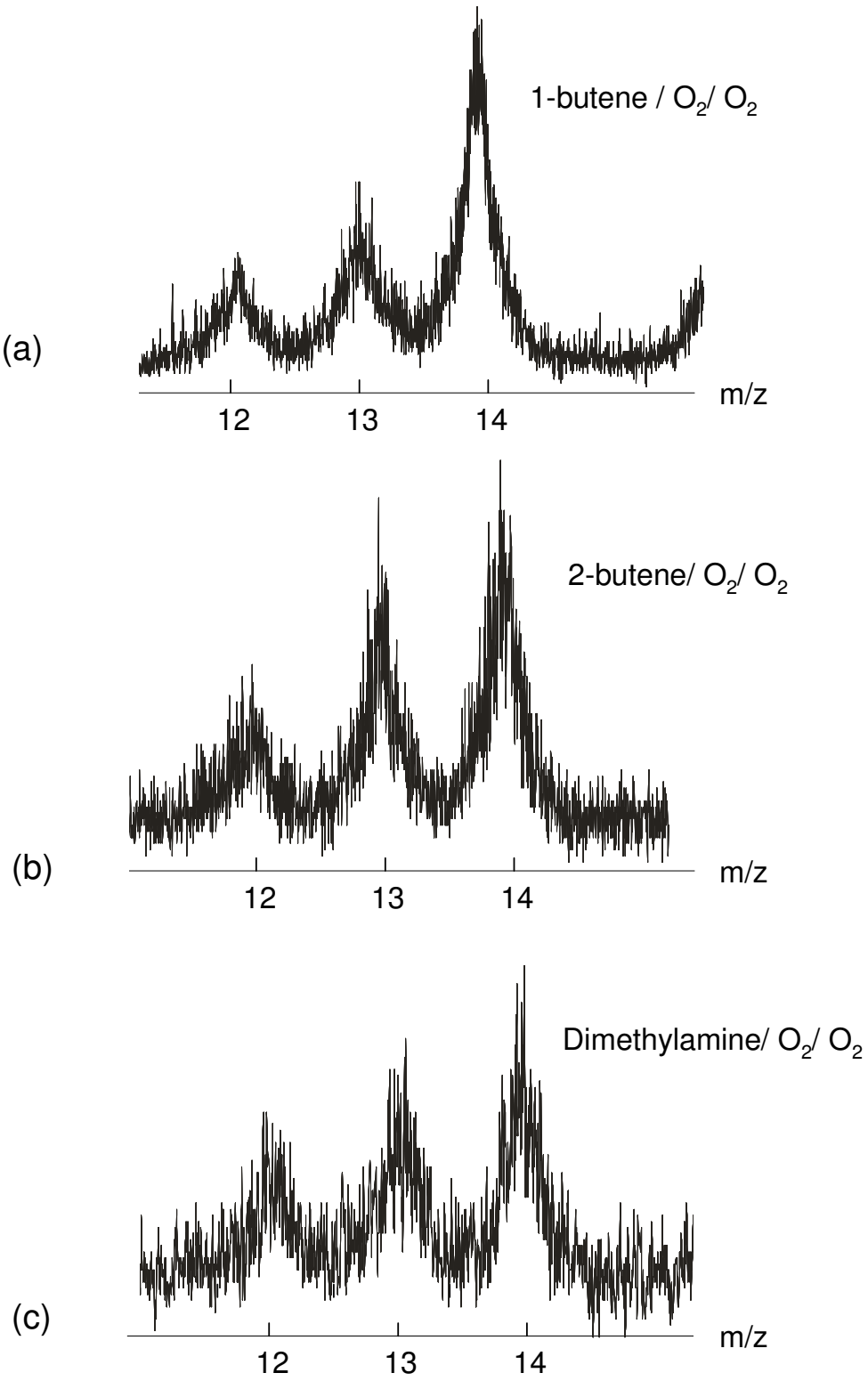
(a)
1-butene / O_2/ O_2
12
13
14
m/z
(b)
2-butene/ O_2/ O_2
12
13
14
m/z
(c)
Dimethylamine/ O_2/ O_2
12
13
14
m/z

Chapter 7 Conclusions

In this study, the activation mechanisms of high energy ion-molecule collisions have been investigated using a modified VG-ZAB mass spectrometer. In the CIE experiment of $N_2O^{+\bullet}$ /He, the relative emission intensity remains constant as the collision energy is increased from 4 keV to 8 keV, a result consistent with the curve-crossing mechanism of collisional activation. The relative vibrational branching ratios of $N_2O^{+\bullet}$ after collisional activation were compared with those obtained by different activation processes. Results confirmed the curve-crossing of different potential energy surface from another aspect.

In the investigation of CIE spectra of $He^{+\bullet}/CO_2$ collisions. The spectra confirmed that the dissociative charge transfer reactions dominate the collisional activation process. The vibrational distribution of the resulting $CO_2^{+\bullet}$ A $^2\Pi_u^+$ state indicate that the excitation mechanism is similar to the photo-excitation as compared with that of the $CO_2^{+\bullet}$ /He collisions due to the shorter reaction time. Differences in the vibrational populations of the

$CO_2^{+\bullet}$ A state in these two types of collisions is likely due to IVR following the formation of higher $CO_2^{+\bullet}$ states when it is the projectile ion.

The source of the O_2-enhancement for certain dissociation channels in O_2 CID experiments has been examined by CIE experiment. Strong $O_2^{+\cdot}$ $A \rightarrow X$ emission which is produced from charge transfer reaction was observed in N_2^+/ O_2 and CH_3^+/O_2 collisions, even though charge transfer is thermochemically unfavorable for CH_3^+/O_2 collisions. It is postulated that the O_2-enhanced dissociation is probably due to the participation of this charge-transfer band.

The existence of hydroxymethylene, with a life time exceeding 13.9 μs, has been confirmed using neutralization-reionization mass spectrometry. The maximum in the relative charge-transfer cross section as a function of IE of the neutralization gas has also been investigated and found to occur at ~8.2 eV, in agreement with our calculated NE_v of $HCOH^+$. Neutral hydroxymethylene can also be produced by proton transfer from CH_2OH^+ to a strong base such as pyridine. There is a kinetic isotope effect for H^+ vs. D^+ transfer from C of ~ 3 due to the near thermoneutrality of the reaction.

Claims to Original Research

1. Collision-induced emission spectra of keV $N_2O^{+\cdot}$/He collisions were collected at different ion translational energy from a wavelength range of 190-1020 nm. This is the first time collision-induced emissions were collected from $N_2O^{+\cdot}$/He. This allows both emissions from the precursor ions and the fragments to be observed. By observing the relative emission intensity of these two groups, it was suggested that these processes were excited by curve-crossings of the potential energy surfaces of the collision complex. The relative intensity within the $N_2O^{+\cdot}$ band does not agree with the Franck-Condon factors, which confirms the curve-crossing mechanism.
2. The collision-induced emissions of $He^{+\cdot}/CO_2$ collisions were also collected, for the first time, in a longer wavelength observation window (190-1020) nm. Atomic emissions from dissociation fragments He, C, $C^{+\cdot}$ and O were observed, showing the dominant reaction is the dissociative charge transfer reaction upon collision. The relative intensity within the $CO_2^{+\cdot}$ band follows the Franck-Condon factors as a result of short transition time at high collision energy.
3. For the first time, collision-induced emission spectra of various ion-O_2 collisions were collected at 8 keV ion translational energy to probing the source of the O_2-enhancement for certain dissociation channels in O_2 CID experiments. Strong $O_2^{+\cdot}$ A→X emissions observed from the N_2^+/ O_2 and CH_3^+/O_2 collisions indicates that the involvement of the charge transfer band of $O_2^{+\cdot}$ is the potential cause for O_2-enhanced dissociation.
4. Neutralization-reionization mass spectrometry was, for the first time, used to generate a highly reactive diradical, *trans*-hydroxymethylene. Its life time was estimated exceeding

13.9 μs. The vertical neutralization NE_v of *trans*-hydroxymethylene has also been calculated for the first time, the value has been confirmed by the experimental observation.

List of publication

1. Y. Lin and P. M. Mayer*, "Do the O_2 Shumann-Runge bands participate in keV collision-induced dissociation experiments?" J. Am. Soc. Mass Spectrom JASMS 2010-4575R1. Accepted.

2. Y. Lin and P. M. Mayer*, "A comparison of the charge transfer and collisional activation processes in ionized CO_2/He collisions" Chem. Phys. CHEMPHYS-D-10-00470R1. In press.

3. Y. Lin and P.M. Mayer*, "Fluorescence from the A $^2\Sigma^+$ state suggests a non-Franck-Condon $N_2O^{+\bullet}$ vibrational state population after keV collisional activation with helium." Can J. Chem. 25 July 2010 (special issue in honour of Tito Scaiano) (CJC 10130). Accepted

4. Y. Lin, M.E. Crestoni, S. Fornarini and P. M. Mayer*,"Can neutral hydroxymethylene play a significant role in interstellar space? A neutralization-reionization and reactivity mass spectrometry study"In preparation.

5. Y. Lin and P. M. Mayer*, "Comparison of keV $O_2^{+\cdot}$/He and $O_2^{+\cdot}$/Ar Collisions by Emission Spectroscopy and Theory" In preparation.